INFORMATION TO USERS

This manuscript has been reproduced from the microfilm master. UMI films the text directly from the original or copy submitted. Thus, some thesis and dissertation copies are in typewriter face, while others may be from any type of computer printer.

The quality of this reproduction is dependent upon the quality of the copy submitted. Broken or indistinct print, colored or poor quality illustrations and photographs, print bleedthrough, substandard margins, and improper alignment can adversely affect reproduction.

In the unlikely event that the author did not send UMI a complete manuscript and there are missing pages, these will be noted. Also, if unauthorized copyright material had to be removed, a note will indicate the deletion.

Oversize materials (e.g., maps, drawings, charts) are reproduced by sectioning the original, beginning at the upper left-hand corner and continuing from left to right in equal sections with small overlaps.

Photographs included in the original manuscript have been reproduced xerographically in this copy. Higher quality 6" x 9" black and white photographic prints are available for any photographs or illustrations appearing in this copy for an additional charge. Contact UMI directly to order.

ProQuest Information and Learning
300 North Zeeb Road, Ann Arbor, MI 48106-1346 USA
800-521-0600

UMI®

DEVELOPMENT OF A PROTOTYPE COMPTON SCATTERING CAMERA USING 3-D POSITION SENSITIVE CZT DETECTORS

by

Yanfeng Du

A dissertation submitted in partial fulfillment
of the requirements for the degree of
Doctor of Philosophy
(Nuclear Engineering and Radiological Science)
in The University of Michigan
2001

Doctoral Committee:

Assistant Professor Zhong He, Chairperson
Professor G. F. Knoll
Professor W. Leslie Rogers
Associate Professor D. K. Wehe

Bell & Howell Information and Learning Company
300 North Zeeb Road
P.O. Box 1346
Ann Arbor, MI 48106-1346

To my parents,
Linzhang Du and Jumei Shang

ACKNOWLEDGEMENTS

I would like to thank my family for their support, love, and encouragement in every stage of my education.

I would like to express my gratitude to those who have contribute to the work. First of all, I thank my advisor, Dr. Zhong He, for his help, guidance and invaluable contributions to this work. His clear explanations and helpful discussions were a constant source of enlightenment for me. Without his help, this work would not have been possible. I would also thank my other advisor, Dr. David Wehe, for his guidance and support whenever it was needed. I shall always be grateful to him. I would also like to thank Dr. Glenn Knoll and Dr. Leslie Rogers for being on my doctoral committee and reviewing my thesis.

In addition, I thank James Berry for his technical support during this project. I am grateful to Wen Li for his help and friendship. I am also very grateful to Clair Branch and James Baciak for their helpful suggestions in editing this thesis. I thank Jose Perez for his GENT3 simulations.

I am also grateful for the Department of Nuclear Engineering and Radiological Science for the financial support through my graduate education.

I also thank John Lehtonen from Applied Physics Lab of Johns Hopkins University for their work on the wire bonds and Dr. Florian Schopper from Max Plank Institute for providing the repeater cards needed for our experiments.

TABLE OF CONTENTS

CHAPTER

LIST OF FIGURES

Figure

LIST OF TABLES

Table

CHAPTER I

INTRODUCTION

Since it is not easy to focus gamma ray as it is for visible light, historically, gamma-ray imaging is performed by combining a mechanical collimator with a position sensitive detector such as an Anger camera [Ang58]. One fundamental problem with these mechanical collimator systems is the inverse coupling between the detection sensitivity and the spatial resolution. Improved efficiency may be obtained by using coded apertures [Mer61, Bar72]. In low energy gamma-ray imaging, it is usually sufficient to construct the aperture from highly absorbing material such as Pb or W. However, for high energy gamma-ray imaging, due to its high penetrating power, the required thickness and size for the collimator is impractically high. A Compton scattering (or electronically collimated) camera has the potential to provide high detection efficiency without sacrificing the spatial resolution, and can work well in high energy applications.

1.1 Compton Camera Developments in Astrophysics, Nuclear Medicine, and Nuclear Industry

Compton scatter cameras have been extensively used in astronomy and astrophysics as telescopes to localize the gamma-ray sources or map the gamma-ray sky. Compton telescopes for astrophysical research originated in independent programs at the University of California [Her75] and at the Max Plank Institute [Sch73] in the early 1970's. Since then, many Compton telescopes have been built for balloon borne missions [Loc79, Ait90, Sch82]. The success of these missions and the improvement in the technology over the following twenty years lead to the launch of COMPTEL on board NASA's Compton Gamma Ray Observatory (CGRO) in 1991. COMPTEL consists of an upper array of 7 liquid scintillation detectors and a lower array of 14 NaI scintillation detectors [Sch93]. It covers the energy range from 0.75-30 MeV with a field-of-view (FOV) of 60° FWHM. COMPTEL has yielded significant breakthroughs in the field of high energy gamma ray astrophysics [Kur98]. The Tracking and Imaging Gamma Ray Experiment (TIGRE) on the INTErnational Gamma Ray Astrophysics Laboratory (INTERGRAL) is planned to launch in 2002 [Tum95]. TIGRE uses multi-layer silicon strip detectors as the first detector and arrays of small CsI(Tl) photodiode detectors as the second detector. With the improved detector energy resolution and the ability to track Compton recoil electrons, TIGRE is expected to be sensitive to gamma rays from 0.3 to 100 MeV with an energy resolution of 3% FWHM and a $1-\sigma$ angular resolution of 120 arc minute at 2 MeV. The absolute detection efficiency is about 8% over the full energy range.

Medical imaging faces markedly different challenges than those in astronomy. The low energy of the commonly used radioactive isotope ^{99m}Tc is well-suited for mechanically collimated systems. Although the Compton scattering method was proposed for medical imaging by Todd et al. in 1974 [Tod74], the first working prototype electronically collimated camera (ECC) was built by Singh and Doria in 1983 [Sin83a, Sin83b]. The ECC replaced the conventional collimator with a High Purity Germanium (HPGe) detector in front of an Anger camera. The comparison between an ECC and a mechanical cone beam collimated system was made by Brechner and

Singh [Bre88]. Their experimental results showed that their ECC achieved the same counting sensitivity at 140 keV for a 25 cm diameter spherical object in less than 10% of the data collection time required by a cone beam mechanical collimated system. The theoretical sensitivity was improved by a factor of 62 for a 32×32 array of HPGe. Other Compton cameras have been suggested for nuclear medicine that use either a silicon [Sol88] or a gas scintillation proportional counter [Fuj87] to replace the HPGe array in the ECC. C-SPRINT, a prototype Compton scattering camera, was intended to extend the work of Singh by using silicon pad detectors in place of HPGe, exploiting a ring of NaI scintillation detectors to improve the resolution and reduce the low angle count rates in the second detector [LeB98]. Despite these efforts, a significant improvement in individual detector performance is required in order for Compton cameras to match or exceed the sensitivity and resolution of the currently commercially available mechanically collimated systems.

To image spatially extended sources and multi-energy gamma-ray field in the 0.5-3 MeV range in the nuclear industry, a Ring Compton Camera (RCC) was designed by Martin et al. [Mar93, Mar94]. In the RCC, the first detector is a 4×4 planar array of HPGe and the second detector is a ring which holds a set of NaI(Tl) scintillation detectors. The ring geometry for the second detector was used to avoid the high count rate from low angle scattering events. The angular resolution is improved at the expense of efficiency in their design. The practical use of the RCC is limited by its low detection efficiency and bulky size.

1.2 Objectives of This Work

Besides the applications in astrophysics, nuclear medicine and the nuclear industry, Compton cameras have potential as radiation imagers in environmental remediation and nuclear treaty verification. These applications are often best served by portable devices. However, previous Compton cameras have used HPGe, or silicon detectors combined with scintillation detectors. Their portability is limited by either the requirement for cryogenic cooling of the semiconductor detectors, the relatively large volume of the photo-multiplier tubes or the larger distance between the two detectors in order to achieve a good angular resolution. In contrast, CdZnTe detectors can be operated at room temperature, can achieve high energy and position resolution compared to scintillation detectors, and can be made compact. 3-D position sensitive CZT detectors have recently demonstrated a 1.5% FWHM energy resolution at 662 keV and a 1 mm position resolution [He99]. These are attractive for portable Compton scattering cameras in the energy region of several hundred keV to a few MeV.

The main objective of this dissertation was to design and build a prototype Compton scattering camera using two 1 cm^3 cubic 3-D position sensitive CZT detectors. We investigated the feasibility of using room temperature CZT detectors in a Compton scattering camera. The performance of the prototype camera was studied analytically and experimentally. Based on these studies, the operating system parameters, such as the separation distance and the central scatter angle between the two detectors, were chosen. Several image reconstruction algorithms were compared and a List-Mode Maximum Likelihood iterative reconstruction algorithm was chosen for the camera. The data acquisition problems associated with two 3-D detectors were addressed and a specialized data acquisition system was designed to maintain the intrinsic detector performance while avoiding the long dead time for individual detectors. The primary experimental results from the camera are presented.

CHAPTER II

THEORETICAL DESIGN CONSIDERATIONS AND PERFORMANCE ESTIMATION

2.1 Compton Scattering

Compton scattering is the dominant interaction for middle energy gamma rays (0.3 - 10 MeV). It is an elastic scattering between the incident photons and electrons in the scatter medium. From the conservation of momentum and energy, the scattered photon energy (assuming the electron is at rest and unbound) is given by

$$E' = \frac{E_0}{1 + \frac{E_0}{m_e c^2}(1 - cos\theta)}, \tag{2.1}$$

where E_0 is the incident photon energy, m_e is the electron mass and θ is the scatter angle. If the electron momentum can not be neglected, the scattered photon energy also depends on the electron momentum. This effect is often referred as the Doppler broadening and will be discussed later in Section 2.3.2.

Compton scattering is an interaction between an incident photon and an electron in the detector material. The Compton scatter cross section increases linearly with material atomic number Z. The scattered photon angular distribution is given by the Klein-Nishina formula [Kno00]:

$$\frac{d\sigma}{d\Omega} = Zr_0^2\left(\frac{1}{1 + \alpha(1 - cos\theta)}\right)^2\left(\frac{1 + cos^2\theta}{2}\right)\left(1 + \frac{\alpha^2(1 - cos\theta)^2}{(1 + cos^2\theta)[1 + \alpha(1 - cos\theta)]}\right), \tag{2.2}$$

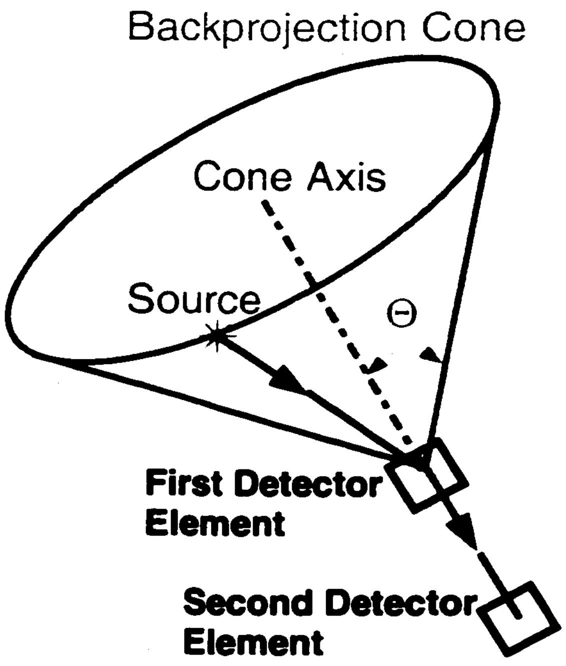

Figure 2.1: Illustration of Compton scatter imaging.

where $\alpha = E_0/m_ec^2$ and r_0 is the classical electron radius. This angular distribution exhibits a strong forward tendency for gamma energies larger than 500 keV.

2.2 Compton Scatter Imaging

In Compton scatter imaging, when the incident photon Compton scatters in the first detector and the scattered photon is detected by the second detector, as illustrated in Figure 2.1, the source location can be backprojected to lie on the surface of a cone. The cone's axis is defined by the interaction positions in the two detectors, and the cone angle, θ, is determined from the Compton equation as:

$$cos(\theta) = 1 - \frac{m_ec^2E_e}{E_0^2 - E_0E_e}, \tag{2.3}$$

where E_e is the energy transfered to the electron during the Compton scattering.

By collecting many such coincident events, these backprojected cones will intersect at the true source position. After proper image reconstruction, the source distribution can be reconstructed. In this way, electronic collimation is achieved.

2.3 Angular Resolution of Compton Scattering Camera

As illustrated in Figure 2.1 and from Equation 2.3, the backprojection angle θ is determined by the initial energy and the energy transfered to the electron. Any energy uncertainty, either due to the detectors' energy resolution or the Doppler broadening effect, will contribute to the uncertainty of θ. As the backprojection axis is determined by the interaction positions in the two detectors, the detector position resolution will contribute to the angular uncertainty of the source location as well. If we assume each component is a Gaussian distribution and independent of each other, the overall angular resolution is the quadratic summation of these three components

$$(\triangle\theta_{overall})^2 = (\triangle\theta_{energy-resolution})^2 + (\triangle\theta_{Doppler})^2 + (\triangle\theta_{geomerty})^2, \qquad (2.4)$$

where $\triangle\theta_{energy-resolution}$ is the detector energy resolution contribution, $\triangle\theta_{Doppler}$ is the Doppler broadening contribution and $\triangle\theta_{geometry}$ is the detector position resolution contribution.

2.3.1 Detector Energy Resolution Contribution

In two detector Compton scatter imaging, the photon must only undergo one scatter in the first detector and the scattered photon must escape the first detector. Under this condition, the measured energy in the first detector E_1 is equal to the energy transfered to the electron E_e. For general imaging applications, the incident gamma-ray energy is unknown. We have to assume the measured energy in the second detector E_2 is equal to the scattered photon energy E'. By replacing E' with

E_2 and E_0 with $E_1 + E_2$, Equation 2.3 becomes

$$cos(\theta) = 1 - \frac{m_e c^2 E_1}{E_2^2 + E_1 E_2}. \tag{2.5}$$

Applying error propagation to Equation 2.5, the energy uncertainty contribution to the angular uncertainty is given by

$$(\Delta\theta_{energy})^2 = (\frac{d\theta}{dE_1})^2(\Delta E_1)^2 + (\frac{d\theta}{dE_2})^2(\Delta E_2)^2. \tag{2.6}$$

From Equation 2.5, we have

$$\frac{d\theta}{dE_1} = \frac{m_e c^2}{sin\theta}\frac{1}{(E_1 + E_2)^2}, \tag{2.7}$$

$$\frac{d\theta}{dE_2} = \frac{m_e c^2}{sin\theta}[\frac{1}{(E_1 + E_2)^2} - \frac{1}{E_2^2}]. \tag{2.8}$$

In above derivation, we assume the scattered photon deposits its full energy in the second detector by a photoelectric interaction. This assumption is not always true, especially for high and middle energy gamma rays where the scattered photons have high probability to undergo another Compton scatter and only deposit a part of their energy in the second detector. In such a case, the energy deposited in the second detector, E_2, is not equal to the scattered photon energy, E'. Therefore, the scatter angle obtained from Equation 2.5 is not related to the true scatter angle. These events will only add background noise to the reconstructed image. In order to eliminate this noise, a window is usually used in the summed spectrum to select full energy deposition events. In this case, instead of using the summed energy for each event to calculate the scatter angle, the centroid or the peak energy of the summed window can be used, i.e. $E_0 = E_s$. Then Equation 2.3 becomes:

$$cos(\theta) = 1 - \frac{m_e c^2 E_1}{E_s^2 - E_s E_1}, \tag{2.9}$$

$$(\Delta\theta_{energy})^2 = (\frac{d\theta}{dE_1})^2(\Delta E_1)^2 + (\frac{d\theta}{dE_s})^2(\Delta E_s)^2, \tag{2.10}$$

$$\frac{d\theta}{dE_1} = \frac{m_ec^2}{sin\theta}\frac{1}{(E_s - E_1)^2}, \tag{2.11}$$

$$\frac{d\theta}{dE_s} = \frac{m_ec^2}{sin\theta}\frac{E_1^2 - 2E_1E_s}{(E_s^2 - E_1E_s)^2}. \tag{2.12}$$

Since the error for E_s only comes from the systematic calibration bias, it is usually much smaller than the individual detector energy resolution. The angular uncertainty in Equation 2.10 is thus dominated by the first term.

For some special applications, such as Single Photon Emission Computed Tomography (SPECT), where the incident gamma-ray energy is known, the angular resolution is solely determined by the first detector energy resolution as given by

$$\triangle\theta_{energy} = \frac{(1+\alpha(1-cos\theta))^2}{E_0\alpha sin\theta}\triangle E_1, \tag{2.13}$$

where $\alpha = E_0/m_ec^2$. In this dissertation, unless otherwise pointed out, the incident gamma energy is assumed to be known.

For our 3-D position sensitive CZT detector, the energy resolution at 59.5 keV, 122 keV and 662 keV is shown in Figure 2.2. The electronic noise is around 3-4 keV. By fitting the measured data points in Figure 2.2, the general relationship between the energy resolution and the deposited energy is given by $\triangle E = 4.0 + 0.29\sqrt{E}$ (keV). Using Equation 2.13, the predicted angular resolution due to the first detector energy resolution for 140 keV gamma rays is shown in Figure 2.3. Since $\triangle\theta_{energy-resolution}$ is larger than 15° for all scatter angles, our CZT detectors with current energy resolution are not suitable as the first detector for low energy Compton scatter imaging for many imaging applications. However, as shown in Figure 2.4 (a), for 511 keV gamma rays, the $\triangle\theta_{energy-resolution}$ is only 2° - 3° for scatter angles between 20° - 80°. The energy resolution contribution decreases as the incident energy increases. As shown in Figure 2.4 (b), $\triangle\theta_{energy-resolution}$ is only about 1° for 1 MeV gamma rays within the 20° - 80° scatter angles. Therefore, the

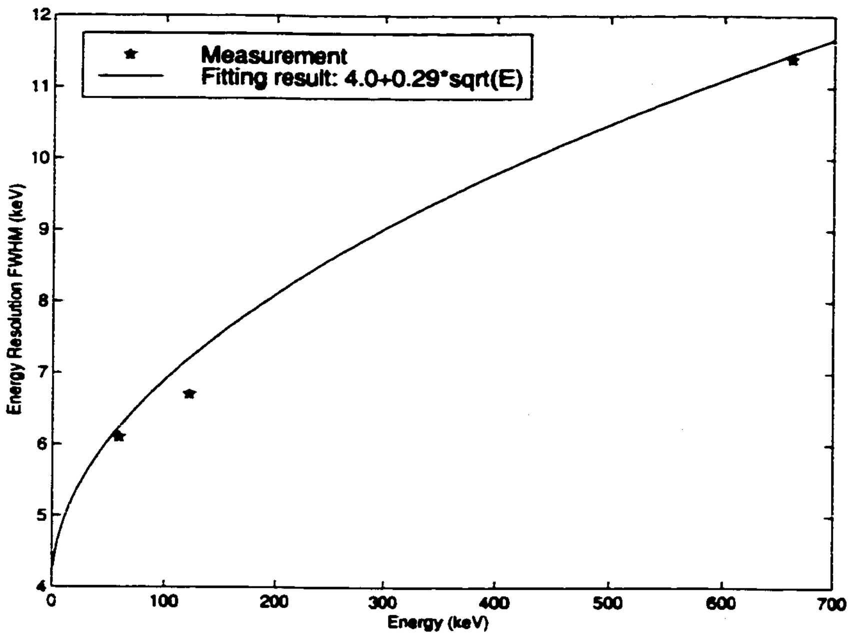

Figure 2.2: Energy resolution of the first detector. The measured energy resolution is for 59.5 keV, 122 keV, and 662 keV gamma rays irradiated from the cathode side of the detector.

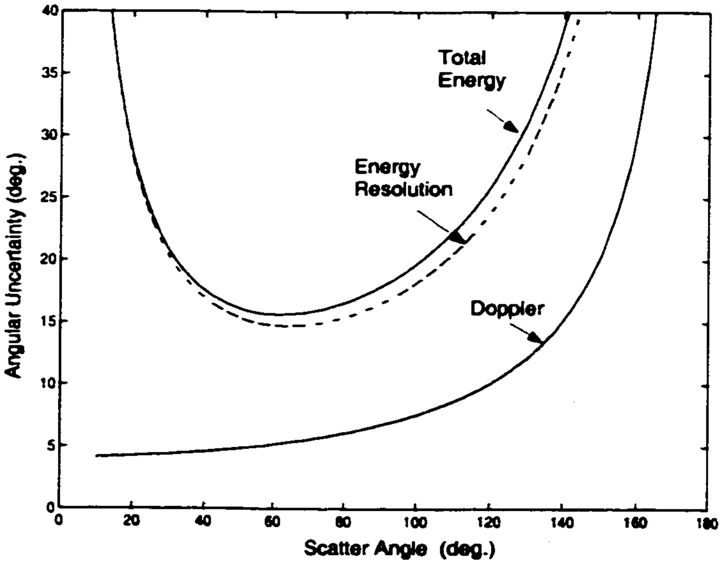

Figure 2.3: Angular uncertainty due to detector energy resolution and Doppler broadening (ref. Section 2.3.2) at 140 keV.

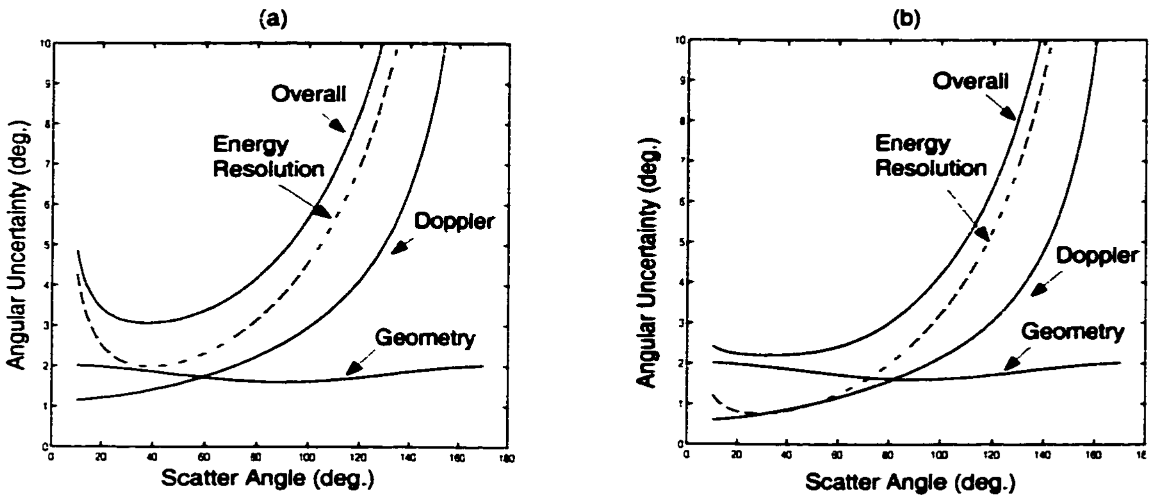

Figure 2.4: Angular uncertainty estimation: (a) for 511 keV, and (b) for 1 MeV

detector energy resolution for our 3-D CZT detectors is good enough for Compton scatter imaging for gamma-ray energies above 500 keV.

2.3.2 Doppler Broadening Contribution

The derivation of Equation 2.1 is based on the assumption that the electron is free and at rest before the scattering interaction. But in reality, bound electrons have finite momenta. As shown in Figure 2.5, if the electron momentum $\vec{P}$ and energy E are included, from the conservation of the energy and momentum, we have

$$\begin{cases} E_0 + E = E_e + E' \\ \vec{P}_0 + \vec{P} = \vec{P}_e + \vec{P'} \end{cases} . \tag{2.14}$$

The energy transfered to the electron by the incident photon is then given by [Cop77]

$$\begin{aligned} E_e &= \frac{|\triangle\vec{P}|^2}{2m_e} + \frac{\triangle\vec{P}\bullet\vec{P}}{m_e} \\ &= \frac{|\triangle\vec{P}|^2}{2m_e} + \frac{|\triangle\vec{P}|p_z}{m_e} \\ &= \frac{E_0^2+E'^2-2E_0E'cos\theta}{2m_ec^2} + \frac{p_z\sqrt{E_0^2+E'^2-2E_0E'cos\theta}}{m_ec}, \end{aligned} \tag{2.15}$$

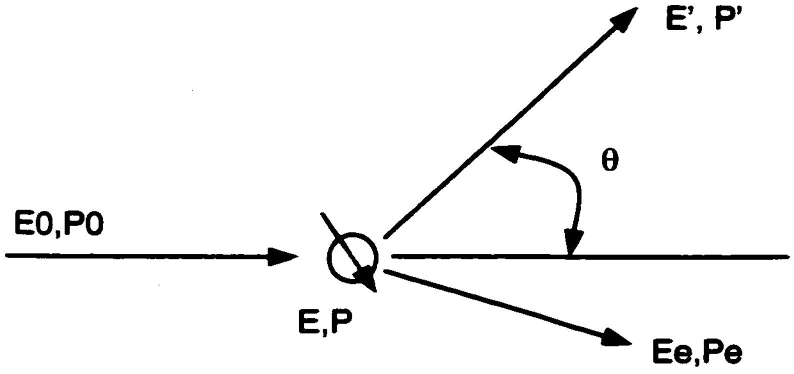

Figure 2.5: Compton scatter from a real electron.

where the scatter vector $\triangle\vec{P}$ is defined as $\vec{P'} - \vec{P_0}$, the momentum difference between the scattered and incident photons, and p_z is the initial electron momentum along the scatter vector direction. In Equation 2.15, the first term on the right side is the usual term given by the Compton equation, and the second term is the Doppler shift, which is linear with respect to p_z and increases with incident energy E_0. Therefore, the scattered photon energy is not only determined by scatter angle, θ, but also depends on the coupling between the scatter vector $\triangle\vec{P}$ and the initial electron momentum, $\vec{P}$. The energy distribution of the scattered photons is given by the double differential cross section [Ces92]

$$\frac{d^2\sigma}{d\Omega dE'} = \frac{1}{2} m_e r_0^2 (E_c^2 + E'^2 - 2E_c E' cos\theta)^{1/2} (\frac{E'}{E_0})(\frac{E'}{E_0} + \frac{E_0}{E'} - sin^2\theta) J(p_z, Z), \quad (2.16)$$

where E_c is the scattered photon energy calculated by the normal Compton equation at scatter angle θ, r_0 is the classical electron radius, and the Compton profile $J(p_z, Z)$ is the initial electron momentum distribution in the scatter medium:

$$J(p_z, Z) = \int\int \rho(p_x, p_y, p_z) dp_x dp_y. \quad (2.17)$$

At a fixed scatter angle θ, the scattered photon energy distribution is mainly determined by the Compton profile $J(p_z)$, because the other terms in Equation 2.16 are

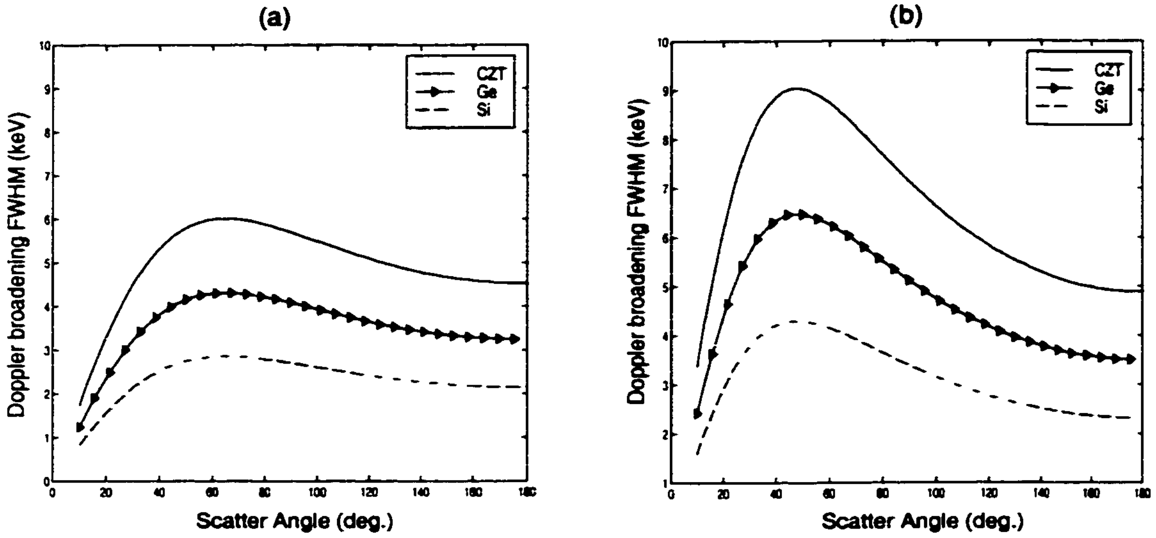

Figure 2.6: Energy uncertainty due to the Doppler broadening effect for: (a) 511keV, and (b) 1 MeV.

relatively slowly varying with E'.

Neglecting the small chemical and lattice effects on the electron momentum distribution in crystals, the calculated FWHM energy spread due to Doppler broadening from Equation 2.16 for silicon, germanium and CZT at 511 keV and 1 MeV are shown in Figure 2.6. These results are based on the calculated Compton profiles in reference [Big75]. For $Cd_{0.8}Zn_{0.2}Te$, the average atomic Compton profile is derived from that for Cd, Zn and Te. From Figure 2.6, it is obvious that the energy FWHM due to Doppler broadening, $\triangle E_{Doppler}$, increases with the incident photon energy and the scatter medium atomic number. For Si and Ge, the $\triangle E_{Doppler}$ is much larger than their intrinsic energy resolution, so the angular resolution due to the energy uncertainty is dominated by the Doppler broadening effect for incident energies above 500 keV. Thus the excellent energy resolution of Si or HPGe detectors is not helpful for Compton imaging at middle and high γ-ray energies.

In Equation 2.13, $\triangle\theta_{energy}$ is approximately proportional to $\triangle E_1/E_0^2$. The energy uncertainty contribution to the angular resolution decreases with increasing incident energy E_0. Even with the poorer available energy resolution and larger Doppler broadening for CZT as comparing to Si and Ge, as shown in Figure 2.4 (a), the overall angular uncertainty due to energy uncertainty at 511 keV is still around 3° for scatter angles between 20° - 80°.

2.3.3 Geometry Contribution

Since the axis of the backprojection cone is determined by the interaction positions in the two detectors, any position uncertainty will contribute to the angular uncertainty [Ord99]. These effects are illustrated in Figure 2.7. The two detector elements are shown as the gray rectangular area. The central distance between them is d. A point source is located at position S in front of the first element.

The contribution from the first detector lateral position resolution is illustrated in Figure 2.7 (a). A gamma ray from the source first Compton scatters at point A (the middle of the upper edge of the first element) by an angle of θ, then the scattered photon is absorbed by the second element at point O_2. In the backprojection, the center position, O_1, of the first element must be used. The backprojected source direction is O_1S'. The angular error, $\triangle\theta_1$, between the true source direction and the backprojected direction is $\angle SO_1S'$. From the geometry relation in Figure 2.7 (a), we have

$$d \cdot sin(\theta + \triangle\theta_1) = W_1 + d \cdot cos(\theta + \triangle\theta_1) tan(\theta + \Phi). \tag{2.18}$$

Since the source to the first element distance SO_1 is much larger than the lateral position resolution W_1, Φ is small compared to θ for useful scatter angles, i.e. $\theta+\Phi \approx$

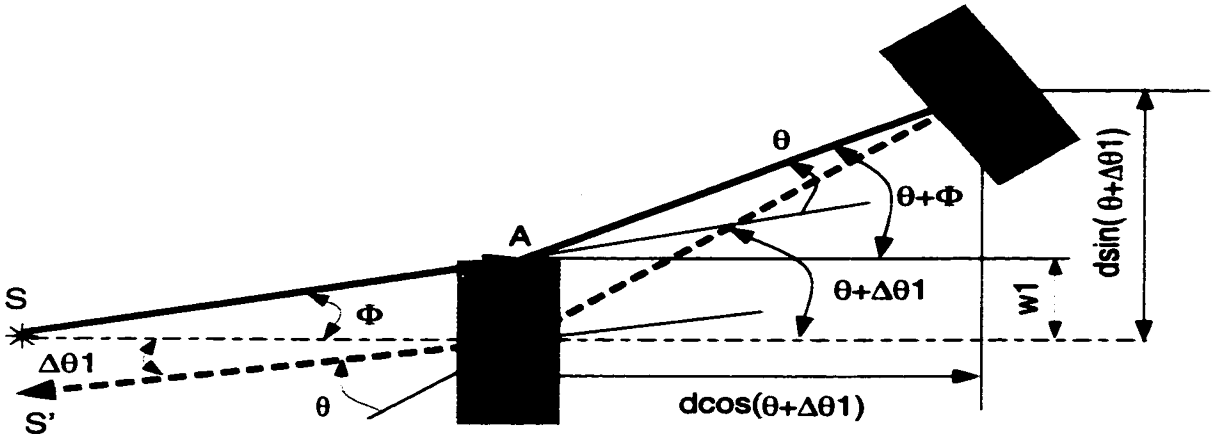

(a) Angular uncertainty due to the first detector lateral position resolution

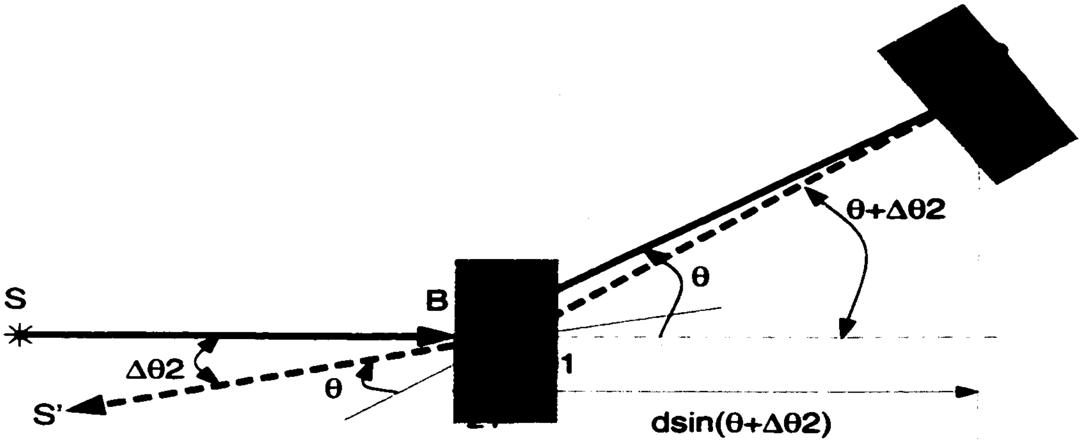

(b) Angular uncertainty due to the first detector depth position resolution

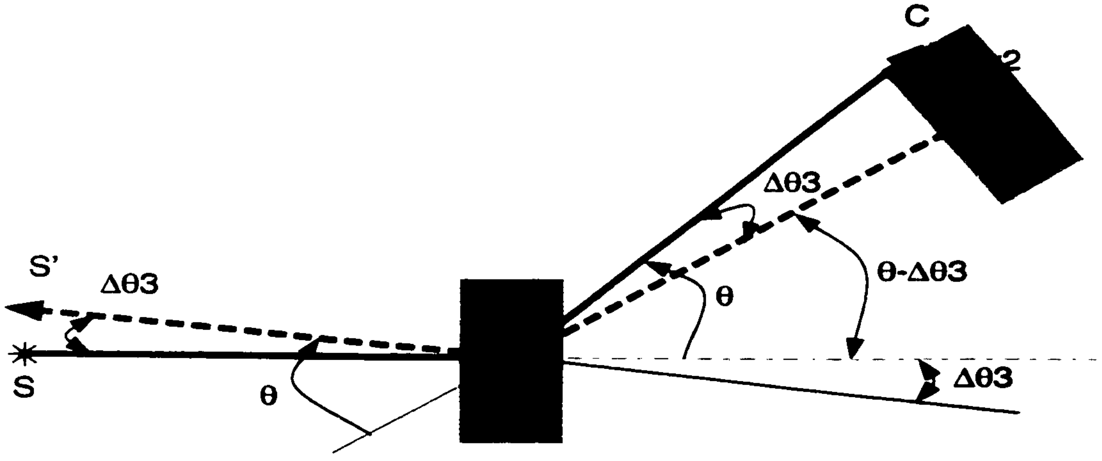

(c) Angular uncertainty due to the second detector lateral position resolution

Figure 2.7: Detector position resolution contribution to the angular uncertainty. The solid arrows in the plots illustrate the true scatter direction. The dashed arrows illustrate the false backprojection direction.

θ. Then $sin(\theta + \Delta\theta_1)$ and $cos(\theta + \Delta\theta_1)$ can be approximated as

$$sin(\theta + \Delta\theta_1) = sin(\theta) + cos(\theta)\Delta\theta_1, \tag{2.19}$$

$$cos(\theta + \Delta\theta_1) = cos(\theta) - sin(\theta)\Delta\theta_1. \tag{2.20}$$

Equation 2.18 becomes

$$d \cdot sin(\theta) + d \cdot cos(\theta)\Delta\theta_1 = W_1 + d[cos(\theta) - sin(\theta)\Delta\theta_1]tan(\theta). \tag{2.21}$$

Finally, the first detector lateral position resolution contribution is given by

$$\Delta\theta_1 = \frac{W_1}{d}\frac{1}{cos(\theta) + sin(\theta)tan\theta} = \frac{W_1}{d}cos(\theta). \tag{2.22}$$

Similarly, the first detector depth position resolution contribution is illustrated in Figure 2.7 (b). From the geometry relation in the plot, we have

$$d \cdot sin(\theta + \Delta\theta_2) = (d \cdot cos(\theta + \Delta\theta_2 + Z_1)tan(\theta). \tag{2.23}$$

Applying Equations 2.19 and 2.20 into this equation, it becomes

$$d \cdot sin(\theta) + d \cdot cos(\theta)\Delta\theta_2 = (d \cdot cos(\theta) - d \cdot sin(\theta)\Delta\theta_2 + Z_1)tan(\theta), \tag{2.24}$$

$$d(cos\theta + sin^2(\theta)/cos(\theta)\Delta\theta_2 = Z_1 tan(\theta). \tag{2.25}$$

The first detector depth position resolution contribution is finally given by

$$\Delta\theta_2 = \frac{Z_1}{d}cos(\theta)tan(\theta) = \frac{Z_1}{d}sin(\theta). \tag{2.26}$$

The second detector lateral position resolution contribution is illustrated in Figure 2.7 (c). It is straightforward from the plot that

$$tan(\Delta\theta_3) = \frac{W_2}{d}. \tag{2.27}$$

Since $\Delta\theta_3$ is small,

$$tan(\Delta\theta_3) \approx \Delta\theta_3 = \frac{W_2}{d}. \tag{2.28}$$

The overall geometry contribution to the angular resolution is the quadratic summation of all these components:

$$\begin{aligned}(\Delta\theta_{geometry})^2 &= 2\Delta\theta_1^2 + \Delta\theta_2^2 + 2\Delta\theta_3^2 \\ &= \tfrac{1}{d^2}(2W_1^2 cos^2\theta + Z_1^2 sin^2\theta + 2W_2^2).\end{aligned} \tag{2.29}$$

The factor of 2 before the $\Delta\theta_1$ and $\Delta\theta_3$ accounts for the two lateral position contributions for each element.

2.3.4 Overall Camera Angular Resolution

As indicated in Equation 2.29, the geometry contribution to the angular uncertainty is approximately inversely proportional to the distance between the two detectors. Since the Compton camera efficiency is inversely proportional to the square of the distance, there is a trade-off between the efficiency and the angular resolution. A reasonable choice will be choosing the distance d such that

$$\Delta\theta^2_{geometry} \approx \Delta\theta^2_{energy-resolution} + \Delta\theta^2_{Doppler}. \tag{2.30}$$

Thus, a good efficiency can be achieved while $\Delta\theta_{overall}$ is only $\sqrt{2}$ worse than that determined by the energy uncertainty components. For our CZT detectors, the lateral position resolution is around 1 mm and the depth position resolution is around 0.5 mm. When the separation distance between two voxels is 4 cm, the $\Delta\theta_{geometry}$ is comparable to $\Delta\theta_{energy-resolution}$ and $\Delta\theta_{Doppler}$ for 511 keV gamma rays as shown in Figure 2.4 (a). We choose the center-to-center distance between the two CZT detectors to be 5 cm so that the distance between the nearest voxels in the two detectors is 4 cm.

As shown in Figure 2.4, the overall angular uncertainty $\triangle\theta_{overall}$ is $3° - 4°$ at 511 keV and reduces to $2° - 3°$ at 1 MeV for scatter angles $20° - 80°$. So we choose the offset angle θ_c between the two detectors to be 50°. The field-of-view (FOV) will be ±30° around the axis of the first detector corresponding to $20° - 80°$ scatter angles.

The actual angular uncertainty for the reconstructed image will be the weighted average of that shown in Figure 2.4 over all acceptable scattering angles. Referring to Figure 2.4, note that the $\triangle\theta_{overall}$ is a slowly varying function of the scatter angle θ over the acceptable angle range $20° - 80°$. As a result, the expected angular uncertainty for the reconstructed image will be similar to that shown in Figure 2.4.

2.4 Efficiency of Compton Scattering Camera

2.4.1 Compton Aperture Efficiency (CAE)

Unless the position resolution for a large volume detector is good enough to get a reasonably good angular resolution, Compton scatter imaging is achieved by a two detector system. In this common mode, a photon must undergo only one Compton scattering in the first detector and the scattered photon must escape the first detector. The Compton Aperture Efficiency (CAE), P_c, is defined as the probability that the incident photon only undergoes one scatter in the first detector and the scattered photon escapes the first detector within a pre-set solid angle:

$$P_c = \int_0^{Z_{max}} dz \int_{\theta_{min}}^{\theta_{max}} d\theta \mu_c(E_0) e^{(-\mu_t(E_0)z)} P(\theta) e^{(-\mu_t(E')L')}, \qquad (2.31)$$

where μ_c, μ_t are Compton scatter and total attenuation coefficient, z is the depth in the first detector, $\theta_{min}, \theta_{max}$ are the minimum and maximum useful scatter angles, $P(\theta)$ is the scatter distribution function, and L' is the escape length the scattered photon travels. In the following calculations, the scatter angle is from 20° to 80°.

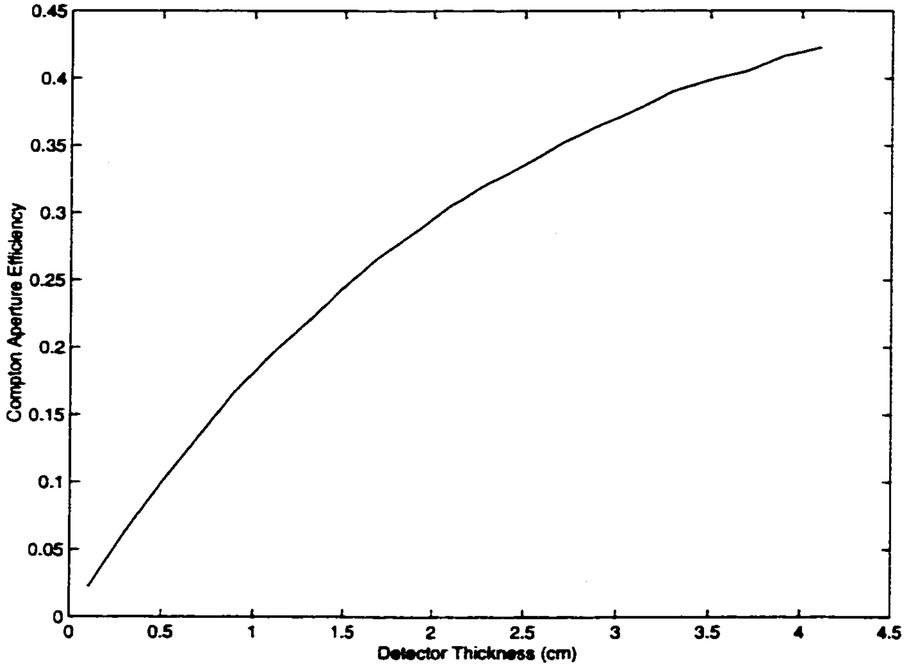

Figure 2.8: Compton aperture efficiency at 662 keV for a 1 mm × 1 mm CZT detector.

For a very small detector, the probability that the scattered photons will be attenuated in the detector itself is small. As shown in Figure 2.8 for a 1 mm × 1 mm CZT detector, P_c increases with the detector thickness. However, in order to get a reasonable overall camera efficiency, many small detectors must be packed together or a single large pixellated detector must be used. In such a case, the attenuation from neighboring detectors or elements will affect P_c. As is shown in Figure 2.9 for a 1 cm thick CZT detector at 662 keV, P_c decreases from 18% to 10.5% as the detector width increases from 1 mm to 6 cm. Since we are only interested in the escaped photons from 20 to 80 degrees, when the detector width increases above 5 cm, the attenuation from neighboring elements become less important, and the Compton aperture efficiency becomes independent of the detector width. For a 20 cm × 20 cm area detector, the variation of P_c with the detector thickness for Si, Ge and CZT

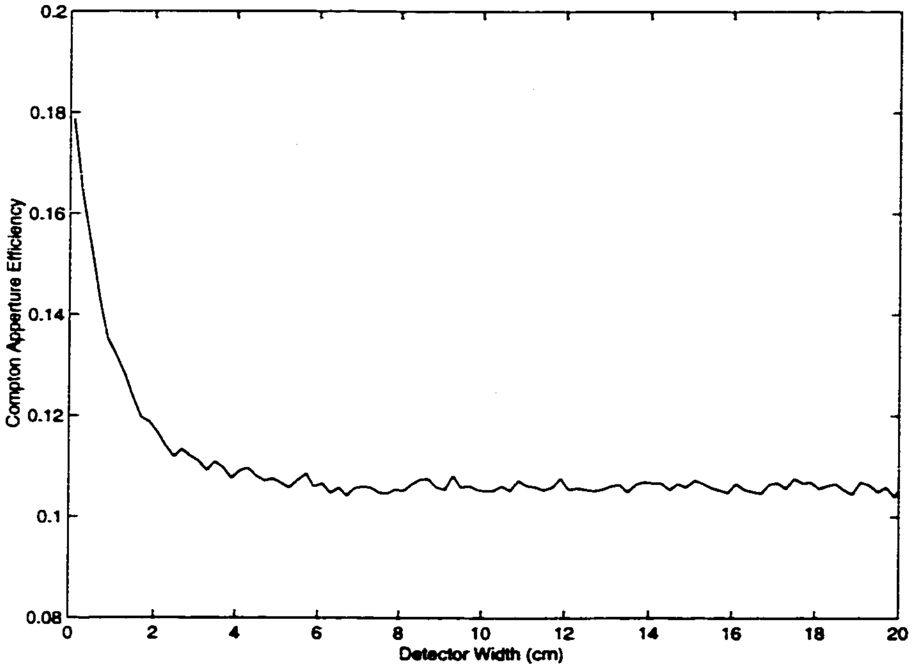

Figure 2.9: Compton aperture efficiency at 662 keV for a 1 cm thick CZT detector.

at several energies from 114 keV to 3 MeV is shown in Figure 2.10. At 114 keV, the maximum CAE for CZT and Ge are only 1% and 4% respectively. The maximum P_c for silicon is 12%. Even at the same thickness, silicon is more efficient than CZT or Ge. When the gamma-ray energy increases to 300 keV, silicon still has the higher maximum CAE than that for CZT and Ge. However Ge reaches its maximum, 11%, at 1 cm thickness, while silicon needs to have a 3 cm thickness to reach its maximum, 14%. From 1 MeV to 3 MeV, Ge and CZT have nearly identical behavior. They will get their maximum CAE around 2 cm. On the other hand, silicon has to have around 6 cm thickness to get the similar efficiency. For a thin detector before the CAE reach their maximum, at the same thickness, Ge and CZT are more efficient than Si when the energy is higher than 300 keV.

Therefore, due to its higher Compton/total cross section ratio, the Si always has

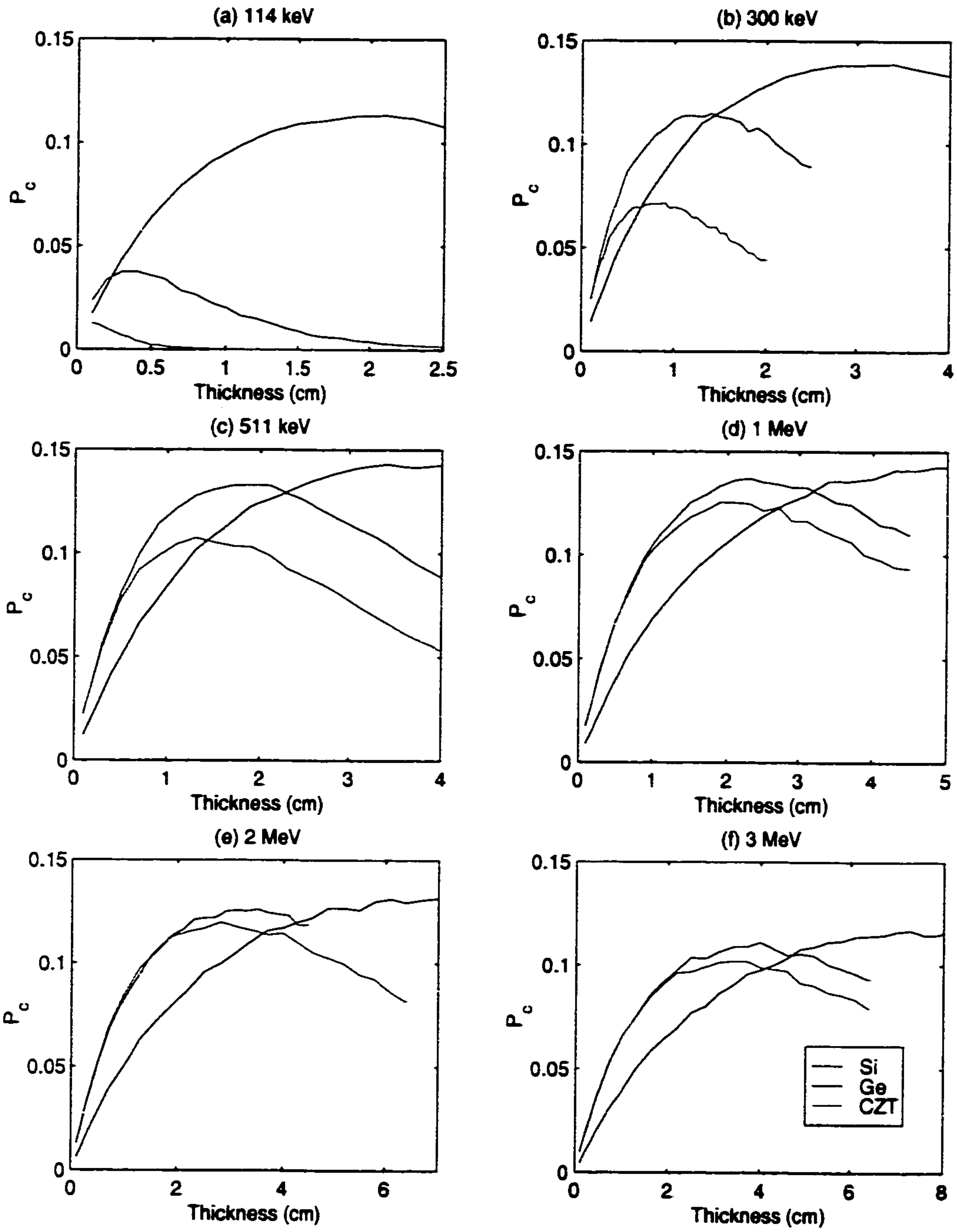

Figure 2.10: Compton aperture efficiency for Si, Ge and CZT detectors with a 20 cm × 20 cm area. This is the calculated results from EGS4 for a collimated source radiated perpendicularly at the the center of the detector surface.

the higher maximum CAE than that for Ge or CZT. PIN Si detectors also have better energy resolution and smaller Doppler broadening than CZT detectors. The currently available PIN silicon detector thickness is usually smaller than 1 mm. In order to have the same efficiency as 1 cm CZT detectors, multiple layers of Si detectors must be stacked together for the first detector. Thus, the readout electronic channels will proportionally increase. Although HPGe can be made thick, the simple depth sensing technique used for CZT detectors can not be used since charge carrier electrons and holes are both collected. For a thick detector without depth sensing capability, the separation distance between the first and the second detectors must increase in order to reduce the geometry contributions to the imaging angular uncertainty. This will adversely affect the overall camera efficiency. Furthermore, the room temperature operation of CZT detectors makes them convenient to use, especially for portable devices. Therefore, a CZT detector with 3-D position sensitive capability is the better choice for the first scatter detector for Compton scatter imaging in the middle and high energy range.

2.4.2 Intrinsic Efficiency of the CZT Compton Camera (CCC)

The intrinsic Compton scattering camera efficiency, ε_{ice}, is defined as the fraction of photons entering the first detector that undergo only one Compton scattering in the first detector and then the scattered photons are photoelectrically absorbed by the second detector. ε_{ice} for a point source can be expressed as

$$\varepsilon_{ice} = \frac{1}{\Omega_1} \int_{det1} dV_1 \int_{det2} dV_2 \Delta\Omega_1 \mu_c(E_0) e^{(-\mu_t(E_0)L_1)} \frac{d\sigma}{d\Omega}(\theta_{12}) \Delta\Omega_2 e^{(-\mu_t(E_1)L_{12})} \mu_p(E_1), \tag{2.32}$$

where Ω_1 is the solid angle subtended by the first detector, $\Delta\Omega_1$ is the solid angle for a differential volume element dV_1 in the first detector, L_1 is the attenuation

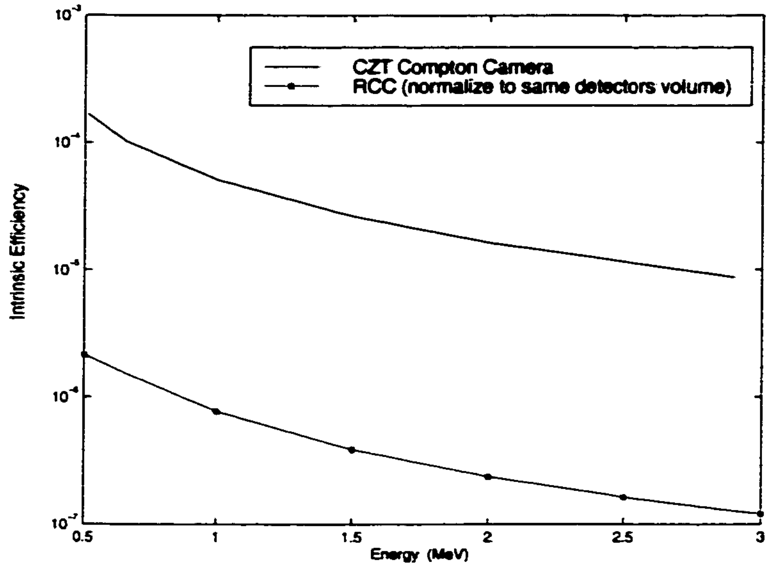

Figure 2.11: Predicted intrinsic efficiency of the CZT Compton camera. The intrinsic efficiency for the RCC is normalized to the same total detector volume as that for the CCC.

length in the first detector between the source and dV_1, μ_t, μ_c, and μ_p are the total, Compton scatter, and photoelectric coefficients respectively, L_{12} is the attenuation length between the two elements dV_1 and dV_2.

Analytical calculation of ε_{ice} requires numerical integration over two detector volumes and the knowledge of interaction probabilities for the initial and scattered γ-rays. Instead of using an analytical approach, the Monte Carlo program EGS4 [Egs4] was used to calculate ε_{ice} for a point source at 10 cm from the first detector surface. The calculated intrinsic efficiency for our Compton camera from 500 keV to 3 MeV is shown in Figure 2.11. The predicted intrinsic efficiency is between 1.5×10^{-4} to 8.8×10^{-6} from 500 keV to 3 MeV. For comparison, the intrinsic efficiency for the Ring Compton Camera (RCC) [Mar94] normalized to the same total detector volume as that for CCC is also shown in Figure 2.11. The first detector for the RCC is a $2 \times 2 \times 0.6$ cm HPGe detector, and the second detector consists of sixteen 1.91 cm diameter by 5.08 cm long NaI(Tl) detectors. The angular resolution of the RCC is from 5.4° at 511 keV to 4.0° at 2.75 keV. Since the CCC has a larger atomic number and reduced distance between the two detectors, its intrinsic efficiency is more than one order of magnitude higher than the normalized ε_{ice} for the RCC. The advantage of using 3-D CZT detectors in Compton scatter imaging is obvious.

In summary, the predicted angular resolution based on our measured detector energy resolution is $3° - 4°$ at 511 keV and reduces to $2° - 3°$ at 1 MeV for scatter angles $20° - 80°$. The optimal offset angle θ_c between the two detectors should be 50° and the center to center distance between the two detectors should be 5 cm. The field-of-view (FOV) will be ±30° around the axis of the first detector corresponding to $20° - 80°$ scatter angles. The predicted intrinsic camera efficiency for this prototype camera is 1.5×10^{-4} to 8.8×10^{-6} from 500 keV to 3 MeV. Although the CZT detectors have larger Doppler broadening and worse energy resolution than Si or Ge detectors, for gamma-ray energy above 500 keV, CZT has useful angular resolution. Furthermore, the room temperature operation of CZT detectors makes them convenient to use, especially for portable devices.

CHAPTER III

IMAGE RECONSTRUCTION

As illustrated in Figure 2.1, when a gamma ray first scatters in the first detector and the scattered photon is detected by the second detector, the source location can be only determined within a backprojection cone if there is no information on the recoiled electron direction. For a pair of detector elements in two detectors located at $(x1, y1, z1)$ and $(x2, y2, z2)$, the cone's axis is determined by the positions of these two elements. If the incident gamma-ray energy is known (or can be determined to be the sum of the energies deposited in the two detectors), the cone angle θ can be determined by the energy deposited in the first detector E_1 from the Compton equation. Therefore, all the source activities located on this cone will contribute to the coincident counts defined by $Y(x1, y1, z1, x2, y2, z2, E1)$. $Y(x1, y1, z1, x2, y2, z2, E1)$ is effectively a weighted integration of the source activity along the backprojection cone. The weighting factor is dependent on the distance between the source and the first detector element. For the same pair of detector elements, different deposited energy, E_1, represents the different backprojection angle, θ. In order to get the true source distribution, multiple projections from different azimuthal angles must be collected. As shown in Figure 3.1, for a point source located on the center of the source plane, the backprojection lines from different azimuthal angles will inter-

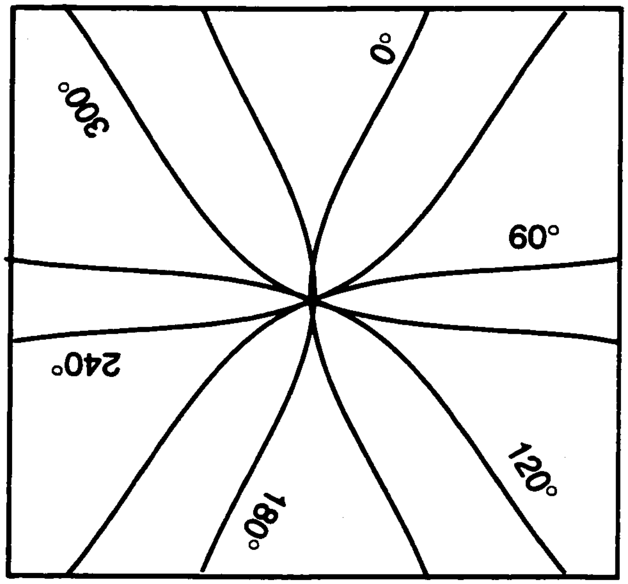

Figure 3.1: Illustration of the backprojection for a point source in Compton scatter imaging. For many backprojections, the distribution falls off approximately as 1/r.

sect with each other at the source location. A proper reconstruction algorithm must be used to reconstruct the original image. This is similar to the situation in parallel projection imaging, such as x-ray Computed Tomography(CT), where parallel projections from different angles are collected. A backprojected image for a point source from parallel projections is shown in Figure 3.2. It is very similar to the the backprojection in Figure 3.1, except for two major differences between them. First, the backprojection line in the source plane for Compton scatter imaging is a conic section, while the backprojection line in parallel projection imaging is a straight line. Second, in parallel projection imaging, the response is spatially invariant. In Compton scatter imaging, even for the same detector element pair, the response is spatially variant since different source points will have different scatter angles related to them. Despite these two differences, the similarity between Compton scatter imaging and parallel projection imaging makes it possible to try to use the image reconstruction

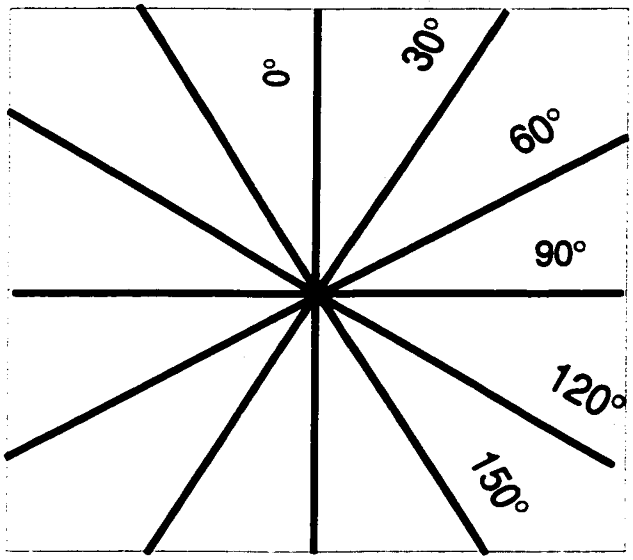

Figure 3.2: Illustration of the backprojection for a point object in parallel projection imaging. The distribution falls off as 1/r.

algorithms in parallel projection imaging as an approximate method for Compton scatter imaging. A brief review of the image reconstruction for parallel projection imaging therefore is given below. Then a review of the iterative image reconstruction algorithms is presented and the implementation of the List-Mode Maximum Likelihood algorithm is presented with the Monte Carlo simulation results.

3.1 Direct Image Reconstruction in Parallel Projection Imaging

3.1.1 Fourier Slice Theorem (or Central Slice Theorem)

All the direct image reconstruction algorithms are based on the Fourier Slice Theorem. As shown in Figure 3.3, the relation between the object and its parallel projection is given by the line integral along the line at angle θ counter-clockwise from y axis and at a distance R from the origin:

$$g_\theta(R) = \int_{L(R,\theta)} f(x,y)dl = \int_{-\infty}^{\infty} f(x,y)\delta(x cos\theta + y sin\theta - R)dxdy. \qquad (3.1)$$

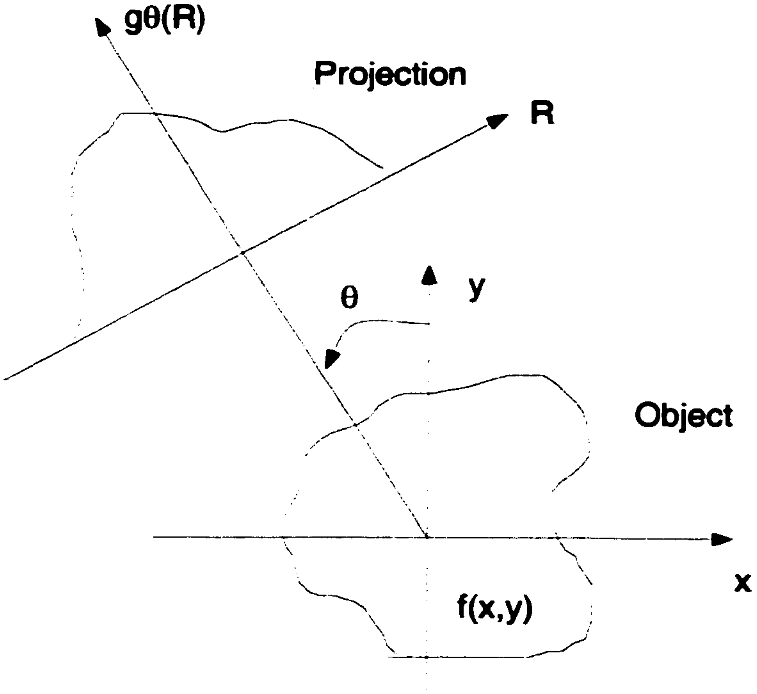

Figure 3.3: Geometry and coordinate system for parallel projection imaging.

The two-dimensional Fourier Transform (2-D FT) of the object is given by:

$$F(u,v) = \int\int f(x,y)e^{-i2\pi ux+vy}dxdy. \tag{3.2}$$

Expressing this in polar coordinates $F(u,v) = F(\rho,\beta)$, where $u = \rho cos\beta$ and $v = \rho sin\beta$, gives

$$F(\rho,\beta) = \int\int f(x,y)e^{-i2\pi\rho(xcos\beta+ysin\beta)}dxdy. \tag{3.3}$$

The one-dimensional Fourier Transform (1-D FT) of a projection $g_\theta(R)$

$$G_\theta(\rho) = \int g_\theta(R)e^{-i2\pi\rho R}dR. \tag{3.4}$$

Substituting Equation 3.1 into the above equation, we have

$$\begin{aligned} G_\theta(\rho) &= \int\int_{-\infty}^{\infty} f(x,y)\delta(xcos\theta + ysin\theta - R)dxdye^{-i2\pi\rho R}dR \\ &= \int\int f(x,y)e^{-i2\pi\rho(xcos\beta+ysin\beta)}dxdy \\ &= F(\rho,\beta). \end{aligned} \tag{3.5}$$

The 1-D Fourier transform of a projection of the object at angle θ equals to the slice at angle θ through the two-dimension Fourier transfer of that object. This theorem is the mathematical basis for tomography.

3.1.2 Fourier-Slice (Gridding) Reconstruction

Since the relation between an object and its projection is given by the Fourier Slice Theorem, intuitively, the object f(x,y) can be reconstructed from its projection $g_\theta(R)$ by the following steps:

- Step 1: Take the 1-D FT of each $g_\theta(R)$ to get $G_\theta(\rho)$ for each θ.
- Step 2: Fill up the 2-D FT of the object $F(\rho, \theta) = G_\theta(\rho)$.
- Step 3: Take the inverse 2-D FT of F(u,v) to get the object f(x,y).

In practice, the step 2 can be complicated. The inverse 2-D FT routine used for the step 3 requires the Fourier transform of the object in Cartesian coordinates $F(u, v)$, whereas the relation $F(\rho, \theta) = G_\theta(\rho)$ is in polar coordinates. One must interpolate between the two coordinates systems. This interpolation is sometimes called gridding. Since the interpolation from polar coordinates to the Cartesian coordinates is time consuming and can cause interpolation artifacts, and the two-dimension inverse Fourier transform in step 3 is also time consuming, this intuitive reconstruction method is rarely used in practice.

3.1.3 Backprojection Filtering (BPF) Reconstruction

The projections can be backprojected into the object space as

$$f_b(x, y) = \int_0^\pi g_\theta(x cos\theta + y sin\theta) d\theta, \tag{3.6}$$

where $f_b(x,y)$ is called a laminogram. The Fourier transform of f_b is given by

$$\begin{aligned} F_b(\rho,\phi) &= \int\int f_b(x,y)e^{i2\pi\rho(xcos\phi+ysin\phi)}dxdy \\ &= \int\int(\int_0^\pi g_\theta(xcos\theta+ysin\theta)d\theta)e^{i2\pi\rho(xcos\phi+ysin\phi)}dxdy \\ &= \int_0^\pi(\int(\int g_\theta(xcos\theta+ysin\theta)e^{i2\pi\rho(xcos\phi+ysin\phi)}dxdy)d\theta. \end{aligned} \tag{3.7}$$

Rotating the coordinates as $x' = xcos\theta + ysin\theta, y' = -xsin\theta + ycos\theta$, we have

$$\begin{aligned} F_b(\rho,\phi) &= \int_0^\pi(\int(\int g_\theta(x')e^{i2\pi\rho(x'cos(\theta-\phi)+y'sin(\theta-\phi))}dx'dy')d\theta \\ &= \int_0^\pi(\int G_\theta(\rho cos(\theta-\phi))e^{i2\pi\rho(y'sin(\theta-\phi))}dy')d\theta. \end{aligned} \tag{3.8}$$

Since the delta function can be expressed as

$$\delta(x) = \int_{-\infty}^{\infty} e^{i2\pi xu}du \tag{3.9}$$

and

$$\delta(sin(\phi-x)) = \sum_n \delta(x-\phi-n\pi), \tag{3.10}$$

Equation 3.7 becomes

$$\begin{aligned} F_b(\rho,\phi) &= \int_0^\pi(\int G_\theta(\rho cos(\theta-\phi))\delta(\rho sin(\phi-\theta))d\theta. \\ &= \tfrac{1}{\rho}\int_0^\pi(\int G_\theta(\rho cos(\theta-\phi))\delta(sin(\phi-\theta))d\theta \\ &= \tfrac{1}{\rho}\int_0^\pi(\int G_\theta(\rho cos(\theta-\phi))\sum^n\delta(sin(\theta-\phi-n\pi))d\theta \\ &= \tfrac{1}{\rho}G_\phi(\rho). \end{aligned} \tag{3.11}$$

Thus

$$F_b(\rho,\theta) = \frac{1}{\rho}G_\theta(\rho) = \frac{1}{\rho}F(\rho,\theta). \tag{3.12}$$

Since 1/r and $1/\rho$ are a 2-D FT pair, the relationship of the laminogram and the object is given by

$$f_b(x,y) = f(x,y) ** \frac{1}{r}, \tag{3.13}$$

where ** represents the convolution operation. The laminogram is just the 1/r blurred version of the original object f(x,y). From the above FT relationship in

Equation 3.12, The FT of the object $f(x, y)$ can be recovered by $F(\rho, \theta) = \rho F_b(\rho, \theta)$. The following backprojection filtering method can be used:

- Step 1: Backproject $g_\theta(R)'s$ to get the laminogram $f_b(x, y)$.
- Step 2: Take the 2-D FT of $f_b(x, y)$ to get $F_b(u, v)$.
- Step 3: Filter the $F_b(u, v)$ by a cone filter $\sqrt{u^2 + v^2}$ to get F(u,v): $F(u, v) = \sqrt{u^2 + v^2} F_b(u, v)$.
- Step 4: Fix the DC value F(0,0) and scaling it if necessary.
- Step 5: Take the inverse 2-D FT of $F(u, v)$ to get the object f(x,y).

Since the 2-D FT and the inverse FT are required for BPF image reconstruction, for a large object, it takes a long time for the BPF algorithm to reconstruct the image.

3.1.4 Filtered Backprojection (FBP) Reconstruction

The object f(x,y) can be represented in the Fourier domain as:

$$\begin{aligned} \text{f(x,y)} &= \int\int F(u, v) e^{i2\pi(ux+vy)} dudv \\ &= \int_o^{2\pi} \int_0^\infty F(\rho, \theta) e^{i2\pi\rho(xcos\theta + ysin\theta)} \rho d\rho d\theta \end{aligned} \tag{3.14}$$

The integrals are then rearranged as:

$$\begin{aligned} \text{f(x,y)} &= \int_o^\pi \int_0^\infty F(\rho, \theta) e^{i2\pi\rho(xcos\theta + ysin\theta)} \rho d\rho d\theta \\ &\quad + \int_o^\pi \int_0^\infty F(\rho, \theta + \pi) e^{i2\pi\rho(xcos(\theta+\pi) + ysin(\theta+\pi))} \rho d\rho d\theta \\ &= \int_o^\pi \int_0^\infty F(\rho, \theta) e^{i2\pi\rho(xcos\theta + ysin\theta)} \rho d\rho d\theta \\ &\quad + \int_o^\pi \int_{-\infty}^0 F(-\rho', \theta + \pi) e^{i2\pi\rho'(xcos(\theta) + ysin(\theta))} (-\rho') d\rho' d\theta \\ &= \int_o^\pi \int_0^\infty F(\rho, \theta) e^{i2\pi\rho(xcos\theta + ysin\theta)} \rho d\rho d\theta \\ &\quad + \int_o^\pi \int_{-\infty}^0 F(\rho, \theta) e^{i2\pi\rho(xcos(\theta) + ysin(\theta))} |\rho| d\rho d\theta \\ &= \int_o^\pi \int_{-\infty}^\infty F(\rho, \theta) e^{i2\pi\rho(xcos\theta + ysin\theta)} |\rho| d\rho d\theta. \end{aligned} \tag{3.15}$$

Thus

$$f(x,y) = \int_0^{\pi} q_\theta(xcos\theta + ysin\theta)d\theta, \tag{3.16}$$

which is just a backprojection operation, where

$$\begin{aligned} q_\theta(R) &= \textstyle\int_{-\infty}^{\infty} F(\rho,\theta)e^{i2\pi R\rho}|\rho|d\rho \\ &= \textstyle\int_{-\infty}^{\infty} G_\theta(\rho)e^{i2\pi R\rho}|\rho|d\rho \\ &= \textstyle\int_{-\infty}^{\infty} G_\theta(u)e^{i2\pi Ru}|u|du. \end{aligned} \tag{3.17}$$

q_θ is the 1-D inverse Fourier transfer of $G_\theta(u)|u|$, so it is a filtered version of projection g_θ, where the filter is given by the ramp filter function $|u|$.

Thus, the object f(x,y) can be reconstructed by Filtered Backprojection by the following steps:

- Step 1: Take the 1-D FT of each $g_\theta(R)$ to get $G_\theta(u)$.
- Step 2: Filter the $G_\theta(u)$ by a ramp filter function $|u|$.
- Step 3: Take the inverse 1-D FT to get the filtered projection $q_\theta(R)$.
- Step 4: Backproject $q_\theta(R)'s$ to get f(x,y).
- Step 5: Fix DC components and scale factor if necessary.

Since only the 1-D FT and the inverse FT are needed, FBP is much faster than BPF to reconstruct the image for a large object. FBP is the most commonly used image reconstruction algorithm in CT.

3.2 Iterative Image Reconstruction

The direct image reconstruction algorithms described in the last section are based on the mathematical idealization of the spatially invariant projection operation with complete sampling that satisfies band-limited digital sampling theory. The measurement noise is not taken into account. By using a simple ramp filter, the high frequency components get amplified, so there will be noise amplification. A window function is usually applied in the filtering step to roll off high frequency noise. This operation is equivalent to applying a spatially-invariant smoothing function to the reconstructed image. This not only limits the spatial resolution but also induces some artifacts to the image. For Compton scatter imaging, since the backprojection line on the source plane is not a straight line as in CT, there is no exact simple mathematical relationship between the original image and its cone projections. Many iterative image reconstruction algorithms, such as Algebra Reconstruction Technique (ART), Maximum Likelihood Estimation and Penalized Weighted Least Square Estimation (PWLS) have been applied to Compton scatter imaging.

In all these statistical iterative imaging reconstruction, the source plane is represented by discrete image vector $\vec{F}$. The coincident measurements $\vec{Y}$ is related to the image by the following equation:

$$\vec{Y} = W\vec{F}, \tag{3.18}$$

where W is the system response matrix. In this equation, no assumption is made about the relationship between the cone projection $\vec{Y}$ and the original image $\vec{F}$. Each element of w_{ij} is the probability that a gamma ray from source pixel f_j will contribute to a coincident count y_i, which is determined by the geometric relations and the cross section for related interactions. The system matrix can be calculated from an analytical model or from Monte Carlo simulations.

3.2.1 Algebra Reconstruction Technique (ART)

The Algebra Reconstruction Technique (ART) was first introduced by Gordon, Bender and Herman in 1970 for solving the problem of three dimensional reconstruction from projections in electron microscopy and radiology [Gor70]. The ART algorithms have a very simple intuitive basis. An initial guess distribution is used at the beginning of the reconstruction. Then forward projection operations are carried out according to Equation 3.18 to generate projections y_i's. The original image $\vec{F}$ is updated according to the difference between these forward projections and their corresponding measured projections. This iterative updating continues until the difference between two successively reconstructed images is smaller than a preset condition. There are many implementations for ART.

Additive ART: If $\vec{F^q}$ is the estimated source distribution at the q^{th} iteration, then from Equation 3.18, the forward projection from the q^{th} estimation is given by

$$y_i^q = \sum w_{ij} f_j^q. \tag{3.19}$$

The difference between the measured projection y_i and the estimated projection y_i^q is given by

$$\delta_i^q = y_i - y_i^q. \tag{3.20}$$

This difference then is applied to each source pixel f_j according to the corresponding weighting factor w_{ij} to update the source distribution estimation:

$$f_j^{q+1} = f_j^q + w_{ij}\delta_i^q / \sum w_{ij}. \tag{3.21}$$

Considering the fact that the source distribution f_j's are always equal or larger then zero, a non-negative constraint can be applied to the update algorithm:

$$f_j^{q+1} = max(0, f_j^q + w_{ij}\delta_i^q / \sum w_{ij}). \tag{3.22}$$

Multiplicative ART: In multiplicative ART, the source intensity is updated according the ratio between the measured projection and the calculated projection:

$$f_j^{q+1} = f_j^q \frac{y_i}{y_i^q} = f_j^q \frac{y_i}{\sum w_{ij} f_j^q}. \tag{3.23}$$

In order for multiplicative ART to work, the initial guess distribution $\vec{F}^0$ must be positive. It has an advantage over the additive ART that once the intensity of a pixel $f_j^q = 0$, then it remains zero in subsequent iterations. As long as the initial guess distribution $\vec{F}^0 > 0$, the non-negative constraint is automatically satisfied in the iterations.

3.2.2 Maximum Likelihood Estimation

Although the relationship between the source distribution and its projections can be described by Equation 3.18, the measured count in each projection y_i is a Poisson distribution due to the random nature of the radioactive nuclear decay and the physical process involved in the measurement. The mean value of this distribution is given by Equation 3.18. Therefore, the image reconstruction problem can be naturally treated as a statistical estimation problem: to estimate $\vec{F}$ from a given measured projection set $\vec{Y}$. The traditional statistical estimation techniques can be used for image reconstruction, such as Maximum Likelihood Estimation.

Since each projection y_i is a Poisson distribution with mean value $\sum w_{ij} f_j$ and given the source distribution $\vec{F}$, the probability density function for projection y_i is:

$$P(y_i|\vec{F}) = \frac{\sum w_{ij} f_j}{(y_i)!} exp(-\sum w_{ij} f_j). \tag{3.24}$$

Since each projection is independent and has the same distribution function, the joint likelihood function for the whole measurement set $\vec{Y}$ is:

$$P(\vec{Y}|\vec{F}) = \prod_i P(y_i|\vec{F}) = \prod_i \frac{\sum w_{ij} f_j}{(y_i)!} exp(-\sum w_{ij} f_j). \tag{3.25}$$

The object of Maximum Likelihood Estimation is to determine the source distribution vector $\vec{F} \geq 0$ that maximizes the likelihood function $P(\vec{Y}|\vec{F})$, or equivalently maximizes any monotonic function of $P(\vec{Y}|\vec{F})$ such as the logarithm likelihood function $lnP(\vec{Y}|\vec{F})$.

One iterative update algorithm to maximize the logarithm likelihood function $lnP(\vec{Y}|\vec{F})$ is derived by Shepp and Vardi [She82] based on the Expectation Maximum (EM) algorithm of Dempster et al [Dem77]. Starting from a uniform initial estimate, the next estimation $(q+1)^{th}$ is computed from the current q^{th} estimation as following:

$$f_j^{q+1} = \frac{f_j^q}{\sum_{i'=1}^{M} w_{i'j}} \sum_{i=1}^{M} [\frac{w_{ij} y_i}{\sum_l w_{il} f_l^q}]. \tag{3.26}$$

3.2.3 Penalized Weighted Least Square Estimation

As pointed out in the last section, the ML-EM algorithm is based on the idealized Poisson model for each measurement. But in PET or Compton scatter imaging, each coincident count, y_i, is the sum of the true coincident events, y_{it}, and chance coincident events, y_{ia}, i.e. $y_i = y_{it} - y_{ia}$. It is the true coincident event that carries the imaging information. The measured coincident count, y_i, needs to be precorrected for the accident coincident count to get the true coincident count ($y_{it} = y_i - y_{ia}$) before any image reconstruction operations. Although the measured coincident count, y_i, and the accident coincident count, y_{ia}, themselves are Poisson distribution, as pointed out in [Fes94], the precorrected data y_{it} is not a Poisson distribution. Thus the pure Poisson-based likelihood methods necessarily involve some approximations. As an improvement over the traditional Least Square Estimation, the Penalized Weighted Least Squares Estimation was proposed by J.A. Fessler [Fes94] for PET image reconstruction.

The traditional least square algorithm minimizes the error between the measured data $\vec{Y}$ and the expected data $\hat{\vec{Y}} = W\vec{F}$ in a least square sense in order to get an estimation for $\vec{F}$. Considering the relative information in each measurement y_i, in PWLS, a weighted least square similarity function is used:

$$\frac{1}{2}(\vec{Y} - W\vec{F})'\Sigma^{-1}(\vec{Y} - W\vec{F}), \tag{3.27}$$

the weighting matrix, Σ, is diagonal with the i^{th} entry equal to σ_i^2, the variance of the i^{th} precorrected measurement y_i. Any unregularized reconstruction method solely based on this objective function produces increasingly noisy images with iterations. To remedy this problem, a smoothness penalty term is added to Equation 3.27 as:

$$\phi(\vec{F}) = \frac{1}{2}(\vec{Y} - W\vec{F})'\Sigma^{-1}(\vec{Y} - W\vec{F}) + \beta R(\vec{F}). \tag{3.28}$$

In this penalized weighted least squares objective function, the effect of the penalty term $R(\vec{F})$ is to discourage disparities between neighboring pixels. The first term encourages agreement with the measured data. The smoothing parameter β controls the trade-off between the spatial resolution and the estimation variance. One commonly used penalty function $R(\vec{F})$ for image reconstruction is given by

$$R(\vec{F}) = \frac{1}{2}\vec{F}'R\vec{F} = \frac{1}{2}\sum_{j}\sum_{k\in N_j} r_{jk}\frac{1}{2}(f_j - f_k)^2, \tag{3.29}$$

where N_j is the set of eight neighbors of the j^{th} pixel. The weights r_{jk} are equal to 1 for horizontal and vertical pixels, and $1/\sqrt{2}$ for diagonal pixels.

The image reconstruction goal is to estimate $\vec{F}$ from measurement $\vec{Y}$ to minimize Equation 3.28. A Successive Over-Relaxation (SOR) algorithm [Sau93, Mur88] is used to iteratively minimize the objective function $\phi(\vec{F})$. The PWLS+SOR procedure is as follows:

Initialization:

$$\begin{aligned}
\vec{F}^0 &= \text{Filtered backprojection of } \vec{Y} \\
\vec{\Delta}^0 &= \vec{Y} - W\vec{F}^0 \\
s_j &= \vec{W}_j'\Sigma^{-1}\vec{W}_j, \forall j \\
d_j &= s_j + \beta \textstyle\sum_{k \in N_j} r_{jk}.
\end{aligned} \tag{3.30}$$

then in the $(q+1)^{th}$ iteration

$$\begin{aligned}
f_j^{new} &= \frac{\vec{W}_j'\Sigma^{-1}\vec{\Delta}^q + s_j f_j^q + \beta \sum_{k \in N_j} r_{jk} f_k^q}{d_j}, \\
f_j^{q+1} &= max[0, (1-\omega) f_j^q + \omega f_j^{new}], \\
\vec{\Delta}^{q+1} &= \vec{\Delta}^q + W(\vec{F}^q - \vec{F}^{q+1}).
\end{aligned} \tag{3.31}$$

The variable ω is used to control the convergence rate.

3.3 List-Mode Maximum Likelihood Image Reconstruction

Maximum Likelihood (ML) or Penalized Weighted Least Square (PWLS) iterative image reconstruction algorithms have been successfully used for Compton scatter imaging. In order to use the ML or PWLS algorithms, the coincident energy spectrum between two detectors must be accumulated during the data acquisition, and the system response matrix is needed for image reconstruction. For the CCC camera presented here, there are 11 × 11 × 20 voxels for each detector. Assigning just 256 channels for each detector voxel pair and only one byte for each channel, the required memory for the coincident spectra will be around 1400 MB, too large for any currently available PC. The impractical memory requirement for the system response matrix prohibits the use of any iterative reconstruction algorithm that requires a system response matrix. Therefore, list mode data acquisition and image reconstruction is the only practical choice. The list-mode maximum likelihood image reconstruction algorithm [Par98, Wil01] is implemented for our Compton camera for image reconstruction.

3.3.1 Algorithm

In the list-mode maximum likelihood reconstruction, the image reconstruction problem is treated as an estimation of a discrete source distribution $\vec{F}$ from finite measurement data sets $\{\vec{A}_j\}$. Denote the M unknown components of the discrete source distribution $\vec{F}$ as $f_1, \cdots, f_i, \cdots, f_M$, where f_i is the expected source activity in pixel i. Let the sensitivity s_i be the corresponding probability that an emitted photon from pixel i is detected as an event. The probability, $P(i|\vec{F})$, for a detected event to originate from pixel i will be

$$P(i|\vec{F}) = \frac{f_i s_i}{\sum_{n=1}^{M} f_n s_n}. \tag{3.32}$$

If we represent each measurement event with an attribution vector $\vec{A}$, which has seven components (interaction positions in two detectors $x_1, y_1, z_1, x_2, y_2, z_2$ and energy deposited in the first detector E_1), then the probability density of measuring an event with attribution vector $\vec{A}$ under the given source distribution $\vec{F}$ is given by

$$p(\vec{A}|\vec{F}) = \sum_{i=1}^{M} p(\vec{A}|i) P(i|\vec{F}), \tag{3.33}$$

where $p(\vec{A}|i)$ is the probability density that a detected event generated in pixel i leads to a measurement $\vec{A}$.

Given a set of measurement $\vec{A}_1, \vec{A}_2, \cdots, \vec{A}_N$ during time T, each measurement is independent and has the identical distribution given by Equation 3.33. The logarithmic likelihood of the set of measurements is:

$$\begin{aligned} L(\vec{A}_1, \cdots, \vec{A}_N|\vec{F}) &= \ln p(\vec{A}_1, \cdots, \vec{A}_N|\vec{F}) \\ &= \sum_{j=1}^{N} \ln p(\vec{A}_j|\vec{F}) \\ &= \sum_{j=1}^{N} \ln(\sum_{i=1}^{M} p(\vec{A}_j|i) f_i s_i) - N \ln(\sum_{i=1}^{M} f_i s_i). \end{aligned} \tag{3.34}$$

The maximum likelihood estimate of the source distribution $\vec{F}$ involves finding the maximum of Equation (3.34) with respect to $\vec{F}$ under the positive constraint:

$$\hat{\vec{F}} = argmax_{\vec{F} \geq 0} L(\vec{A}_1, \cdots, \vec{A}_N | \vec{F}). \tag{3.35}$$

To find the ML solution, an Expectation Maximization (EM) iterative updating algorithm was derived in Ref. [Par98]:

$$f_l^{q+1} = \sum_{j=1}^{N} \frac{p(\vec{A}_j|l) f_l^q}{T \sum_{i=1}^{M} p(\vec{A}_j|i) s_i f_i^q}. \tag{3.36}$$

Beginning with any initial guess $\vec{F}^{(0)} \geq 0$, this algorithm converges to a global maximum of the likelihood function in Equation (3.34), i.e. $\vec{F}^{(\infty)} = \hat{\vec{F}}$ [Par98]. In practical implementation, $\vec{F}^{(0)}$ can be simply set to a uniform distribution or the BPF reconstructed image. The iteration time can be controlled by a preset criteria, such as the mean squared difference between two successive iterations.

By Bayes' rule, the probability density $p(\vec{A}|i)$ needed in Equation 3.36 can be written as $p(\vec{A}|i) = p(\vec{A})P(i|\vec{A})/P(i)$, where $P(i) = s_i$. The conditional probability $P(i|\vec{A})$ of an event having originated from pixel i given a measured attribution vector $\vec{A}$ will be the true $P(i|\vec{A}')$ convolved with the measurement noise distribution function $p(\vec{A}'|\vec{A})$. Therefore

$$p(\vec{A}|i) s_i = p(\vec{A}) \int P(i|\vec{A}') p(\vec{A}'|\vec{A}) d\vec{A}', \tag{3.37}$$

where $\vec{A}'$ is the unknown true attribution vector for a detected event. Assuming the measurement noise distribution for each position component is an independent zero-mean Gaussian function with FWHM given by the detectors' position resolution, and the noise distribution for E_1 is the convolution of a Gaussian function with the known detector energy resolution with a Doppler broadened distribution, the multivariate distribution $p(\vec{A}'|\vec{A})$ is simply the product of the distributions for each component.

Given the true attribution vector $\vec{A}'$, the probability $P(i|\vec{A}')$ that the event is originated from pixel i is given by:

$$P(i|\vec{A}') = \begin{cases} \frac{1/r_i^2 exp(-\mu_t L_i)}{\sum_l P(l|\vec{A}')} & \text{when i is on the cone defined by } \vec{A}' \\ 0 & \text{otherwise} \end{cases}, \tag{3.38}$$

where r_i is the distance between source pixel i and the interaction location in the first detector, L_i is the attenuation length in the first detector between them, and the μ_t is the total attenuation coefficient for incident photons.

For simplicity, the measurement noise will be neglected, i.e., $p(\vec{A}'|\vec{A}) = \delta(\vec{A}' - \vec{A})$, so Equation 3.37 reduces to

$$p(\vec{A}|i)s_i = p(\vec{A})P(i|\vec{A}'). \tag{3.39}$$

The update algorithm becomes:

$$f_l^{q+1} = \sum_{j=1}^{N} \frac{1/r_{lj}^2 exp(-\mu_t L_{lj})\delta_{lj} f_l^q / s_l}{T \sum_{i=1}^{M} 1/r_{ij}^2 exp(-\mu_t L_{ij})\delta_{ij} f_i^q}, \tag{3.40}$$

where $\delta_{ij} = 1$ when pixel i is on the cone defined by $\vec{A}_j$, and $\delta_{ij} = 0$ otherwise.

The sensitivity, s_i, needed in Equation 3.40 can be calculated by numerical integration or by a Monte Carlo approach before the reconstruction. In our implementation, it is approximated as

$$s_i \propto \frac{1}{R_{ic}^2} \frac{d\sigma}{d\Omega}(\theta_{i12})\mu_p, \tag{3.41}$$

where R_{ic} is the distance from the pixel i to the center of the first detector, θ_{i12} is the central scatter angle for pixel i, $d\sigma/d\Omega(\theta_{i12})$ is the corresponding Klein-Nishina Compton scattering angular cross section, and μ_p is the photoelectric coefficient for the scattered photon coming from scatter angle θ_{i12}.

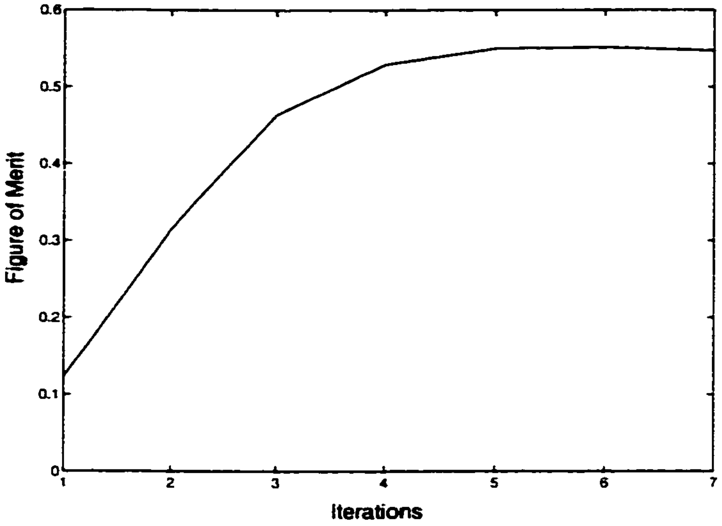

Figure 3.4: Figure of merit during reconstruction iterations for the point source at the origin in Figure 3.5.

3.3.2 Monte Carlo Simulation Results

In order to verify the analytical angular resolution predictions given in Section 2.3 and test the implementation of the List-Mode Maximum Likelihood image reconstruction described above, the EGS4 program was used to generate simulated data for 662 keV point and spatially extended sources at a source plane 10 cm from the first detector. Gaussian noise with a corresponding FWHM for each parameter was added to the Monte Carlo generated interaction data to simulate measurement noise.

The generated data consisted of 6133 total events using 12 angular samplings covering 2π, for five point sources located at (0,0),(0,±4),(±4,0). Beginning with a uniform distribution, the point spread function (PSF) figure-of-merit, G[1], improves during iterations as shown in Figure 3.4 for the source at the origin. The figure-of-

---

[1] PSF figure-of-merit G is defined as $G = \frac{max[f(n_1,n_2)]}{[\sum_{n1}\sum_{n2}|f(n_1,n_2)|^2]^{(1/2)}}$, where n_1, n_2 are 2-D pixel indexes within the PSF. G incorporates the entire PSF in the resolution measure, unlike the FWHM which only gives the resolution along a line. For an ideal delta function PSF, G=1.

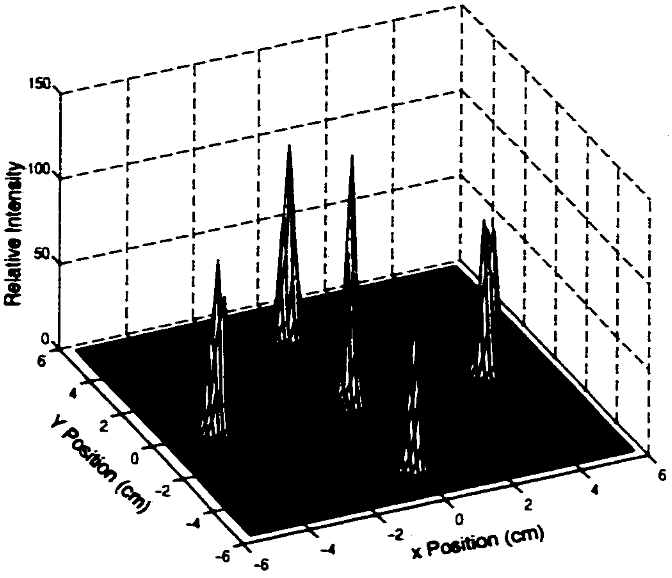

Figure 3.5: Reconstructed image for 5 point sources located 10 cm from the first detector surface from Monte Carlo simulated data.

merit improves quickly during the first 3 iterations, then becomes constant after the 5^{th} iteration. This shows that the list-mode likelihood algorithm is very efficient, requiring only 6-7 iterations for reconstruction. The reconstructed image after six iterations is shown in Figure 3.5. The correct source locations, source activity ratios and small background in the reconstructed image all indicate that the reconstruction procedure is very effective. The FWHM for the on-axis source is 3.2 mm, equivalent to a 1.9° angular resolution. The average FWHM for the four off-axis sources is 4.7 mm, equivalent to 2.7°. Compared with the corresponding predicted angular resolution of 2.8° (at 50° scattering angle) and 3.2° (at 70° scattering angle) for 662 keV, the simulation results are slightly better than the predictions. Considering that the simulation does not including the Doppler broadening effects, the simulation and analytical predictions agree well.

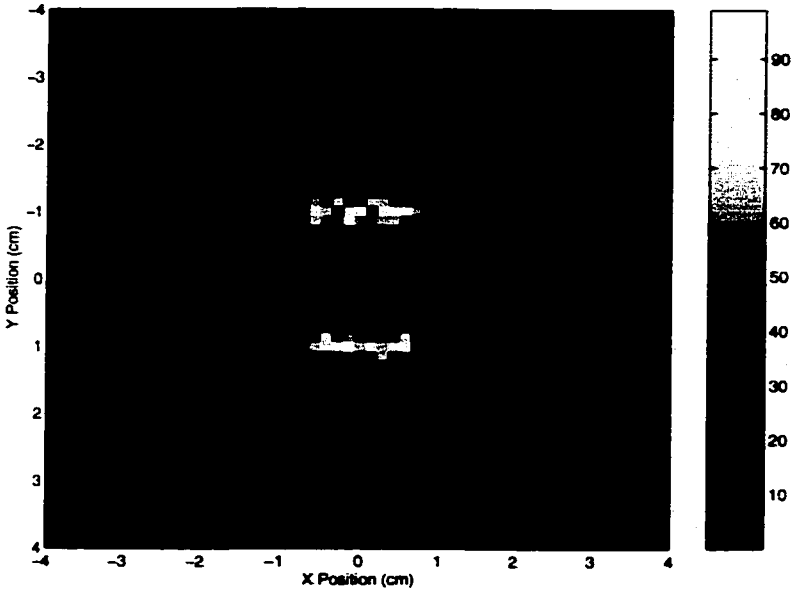

Figure 3.6: Reconstructed image for two 1 cm long line sources from Monte Carlo simulated data. Each line is 2 cm in length. The distance between them is 2 cm.

Figure 3.6 is the reconstructed image for two 1 cm line sources using 7121 simulated events. The average FWHM for the two lines along the y direction is 4.4 mm ($\approx 2.5°$), which is similar to FWHM for the point sources in Figure 3.5. The signal-to-noise ratio in the reconstructed image (SNR_{ccc}) on the two lines is 3.37. Since the interaction data were simulated by a Monte Carlo program, the source location for each simulated event is known and the true signal-to-noise ratio (SNR_{true}) is 15.28 for the corresponding data set. The encoding penalty is equal to the ratio $SNR_{true}/SNR_{ccc} = 4.5$. Thus, in order to have the same signal-to-noise ratio as a perfect mechanically collimated camera, the efficiency of the CCC must be 20 times higher.

CHAPTER IV

ROOM TEMPERATURE SEMICONDUCTOR DETECTORS AND 3-D POSITION SENSING

4.1 Introduction

As pointed out in Chapter 2, the angular resolution of Compton scatter imaging is mainly determined by the detector energy resolution and position resolution. In order to obtain a good angular resolution, detectors with high energy and position resolution are needed for Compton scatter imaging. High energy resolution radiation detectors are also needed in many other applications. Currently, the HPGe and Si semiconductor detectors can achieve the best energy resolution. But HPGe detectors need to be operated at liquid nitrogen temperature. For low noise applications, Si PIN detectors are limited in detector thickness and Si(Li) detectors need to be cooled. This is a major limitation for HPGe and Si detectors. This low temperature operation makes them not only expensive and inconvenient to operate, but also unsuitable for many applications, such as portable devices. Another undesired property of Ge and Si is their relatively low atomic numbers, 32 and 14 respectively. Due to these limitations, people have tried to find alternate semiconductor materials that can operate at room temperature and can provide high efficiency.

For semiconductor detectors, the energy resolution is determined by three components: statistical noise, electronic noise, and the variations in charge collection efficiency. The statistical noise is due to the charge carrier number fluctuation. The larger the number of charge carriers that are generated, the smaller the statistical noise is. So narrow band gap energy material is preferred to increase the the number of charge carriers excited per ionizing radiation event. The electronic noise is mainly determined by the detector leakage current and the detector capacitance. A wide gap material is preferred to reduce the thermally generated charge carrier concentration to reduce the leakage current. The third contribution to the detector energy resolution is the incomplete charge collection due to the charge carrier trapping or recombination. In order to ensure efficient charge carrier extraction, long charge carrier free drift time and large mobility are desired. For x-ray or gamma-ray detectors, the preferred interaction is photoelectric effects. Since the photoelectric cross section is proportional to Z^{3-4}, where Z is the material atomic number, in order to have high detection efficiency and more photoelectric interactions, high Z material is wanted.

Many compound semiconductors such as CdTe, CdZnTe, HgI, and PbI have most of the above desired properties. Their band gap is wide enough to ensure the room temperature operation, while their band gap is narrow enough to ensure a good intrinsic energy resolution. Furthermore, these compound semiconductor materials have larger atomic number than that for Ge and Si. As pointed out earlier, a higher atomic number implies a higher photoelectric cross section and higher detector efficiency. However due to the high defect densities and impurity concentrations, the charge carrier mobility (μ) is low and the charge carrier lifetime (τ) is very short, especially for holes. The low mobility and short lifetime severely affect the charge carrier collection. In order to produce high resolution detectors from these materials, one would prefer to improve the material growth and purification process to produce good quality crystals that have large $\mu\tau$ products. Despite decades of effort, the progress in material processing is very slow. Given this reality, instead of waiting for good material to appear sometime in the future, many techniques have been applied to get good energy resolution from currently available material, such as electronic pulse discrimination or compensation and single polarity charge sensing techniques.

4.2 Energy Resolution Enhancement Techniques

In semiconductor detectors, following the initial electron-hole pair generation from the incident radiation, the electrons and holes drift in the electric field present in the device. These charge carriers also undergo diffusion, recombination, trapping and detrapping. Among these processes, under normal detector operating conditions, the electric field within the device is high enough to sweep the charge carriers away from each other so that recombination has little effect on the detector response.

While the charge carriers are drifting in the detector, charges will be induced on the external electrodes. According to Remo-Schockley theorem [Ram39, Sho38], The induced charge, Q, on electrode i is given by:

$$Q_i = qV_{wi}, \tag{4.1}$$

where q is the charge of the charge carriers, and V_{wi} is the weighting potential for electrode i (calculated by setting electrode i to unity potential, other electrodes to zero potential, and ignoring any space charge in the detector volume). According to Equation 4.1, when charge carrier q moves from point A to point B, the net induced charge produced on electrode i is

$$\triangle Q_i = q\triangle V_{wi}, \tag{4.2}$$

where $\triangle V_{wi}$ is the weighting potential difference between point A and point B. By

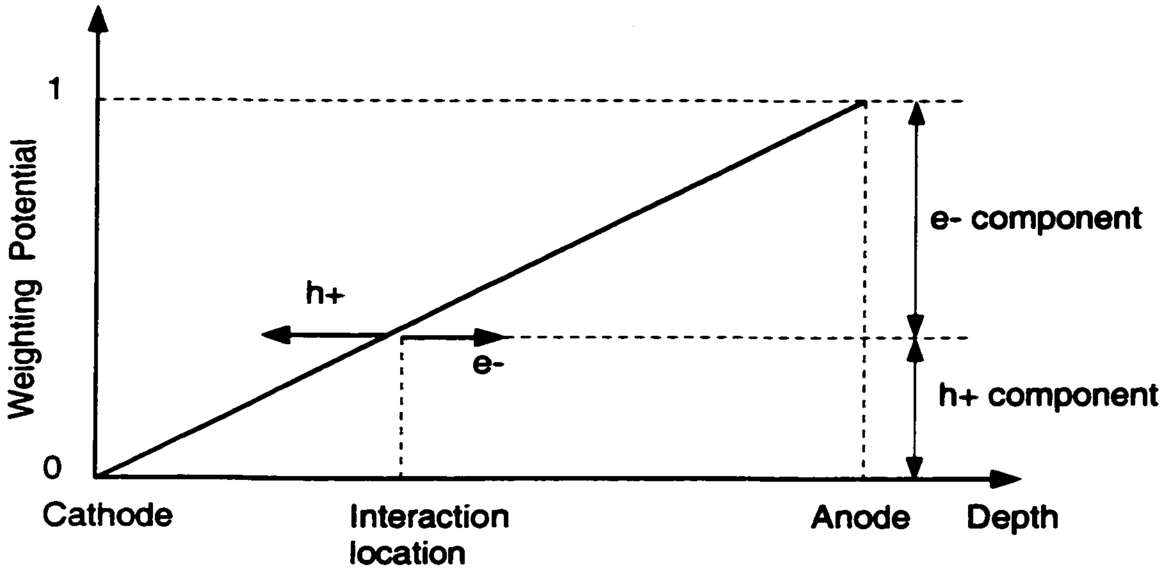

Figure 4.1: Weighting potential for a planar detector

taking the time derivation for Equation 4.2, the instantaneous current produced by charge carrier q's motion is

$$\begin{aligned} i_i &= \frac{\Delta Q_i}{dt} \\ &= q\frac{\Delta V_{wi}}{dt} \\ &= q\frac{\Delta V_{wi}}{dx} \times \frac{dx}{dt} \\ &= qE_{wi}\nu, \end{aligned} \tag{4.3}$$

where E_{wi} is the weighting field for electrode i, and ν is the charge carrier velocity (the product of the carrier mobility and the actual operating electric field).

As shown in Figure 4.1, the weighting potential for a planar detector is a linear distribution from 0 to 1. The electron and hole contributions to the anode and the cathode depend on the charge carrier generation depth in the detector. But as long as all the electrons and holes can be collected within the integration time of the shaping amplifiers, the signal amplitude is independent of the interaction depth and only determined by the number of the charge carriers, which is proportional to the incident radiation energy. This is the case for Ge and Si detectors.

However, for many compound semiconductor materials, a significant fraction of the charge carriers can not be collected due to the low mobility and charge carrier trapping. The induced charge becomes a function of the interaction position. Neglecting the diffusion and detrapping effects, the interaction depth dependent induced charge from the charge carrier transportation in a uniform electric field is given by Hecht's relation [Hec32, Aku69, Kno93]

$$Q = eN_0 \frac{\nu_h \tau_h}{W}(1 - exp([\frac{-z}{\nu_h \tau_h}])) + \frac{\nu_e \tau_e}{W}(1 - exp([\frac{z - W}{\nu_e \tau_e}])), \tag{4.4}$$

where τ is the charge carrier lifetime, z is the radiation interaction location measured from the cathode side, W is the detector thickness, and the e and h subscript represent electrons and holes respectively. The induced charge is a function of carrier extraction factor $\nu\tau/W$ for both electrons and holes and a function of the interaction position. The charge collection efficiency can approach 1 if the carrier extraction factor is greater than about 50 [Kno00]. For CdZnTe, the $\mu\tau$ is around $1.0 \times 10^{-3} cm^2/V$ and $2.4 \times 10^{-5} cm^2/V$ for electrons and holes respectively [McG97]. For a normal operating electric field of 1000 V/cm, the maximum mean free drift length is 0.1 cm and 2.4×10^{-3} cm for electrons and holes respectively. In order to get a carrier extraction factor of about 50, the maximum detector thickness is only about 4.8×10^{-5} cm. For other compound semiconductor materials, due to their even smaller $\mu\tau$ products, the maximum detector thickness to get a good energy resolution is even smaller. For many gamma-ray applications, the detection efficiency for such a thin detector is too small. In order to build a thick detector, some resolution enhancement techniques must be applied to mitigate the severe charge trapping problems, especially for holes.

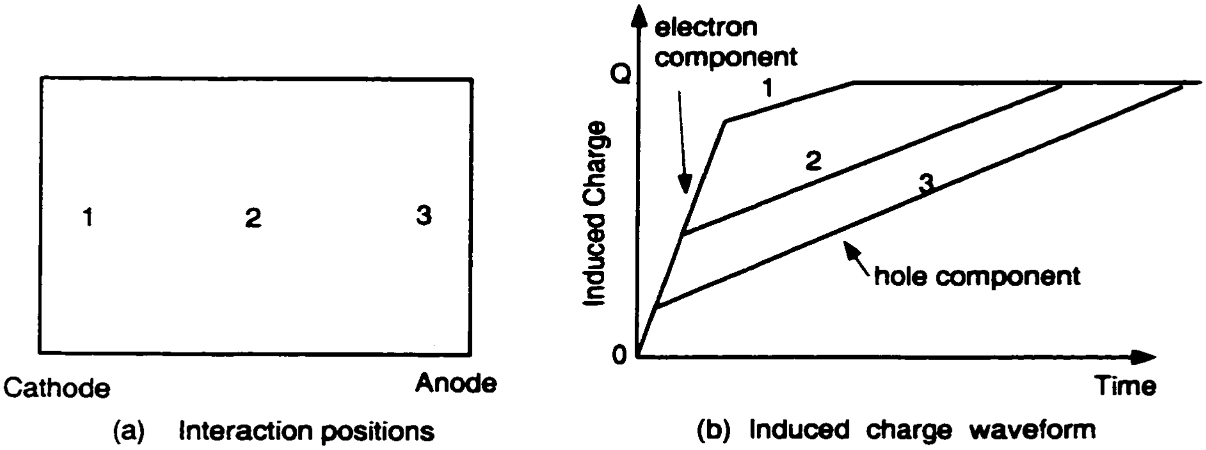

(a) Interaction positions (b) Induced charge waveform

Figure 4.2: Induced charge waveforms for interactions at different depths.

4.2.1 Electronic Signal Processing Techniques

For most compound semiconductor materials, the electrons have a much higher mobility than that for holes, and the lifetime of electrons is also much longer than that for holes. As shown in Figure 4.2, the induced signal on the anode has two components: a fast electron contribution and a slow hole contribution. If the holes can only drift a very short distance before they get trapped, the hole contribution is very small. The signal amplitude is thus mainly determined by the electron contribution. As shown in Figure 4.2, the signals from different depths not only have different amplitudes, but also have different rise times and signal waveforms. The detector energy resolution can be enhanced by electronic signal processing techniques by exploiting the correlation between the signal amplitude loss with its rise time or waveform shape.

Since the signal rise time is mainly determined by the electron drift time in the detector, which in turn depends on the interaction depth, signals with the same rise time will have the same charge carrier collection efficiency. By selecting signals with the same rise time, the Pulse Rise Time Discrimination (PRTD) approach can effectively increase the energy resolution [Squ89, Jon75]. But by collecting signals within a rise time discrimination window, only those interactions at the narrow depth corresponding to the selected rise time are collected. Thus the detector energy resolution is enhanced at the price of losing efficiency. This is not a practical approach for most applications.

If the hole contribution to the signal amplitude can be neglected and the electron trapping is small, the signal amplitude loss due to hole trapping is a linear function of the rise time. Using this correlation, the analog rise time compensation method adds an analog signal to the anode signal proportional to its rise time. A 7.5 keV energy resolution for 662 keV gamma ray was obtained with a 5 mm × 5 mm × 2 mm CdTe detector [Ric92]. One problem with this analog rise time compensation is that, due to finite hole contribution and electron trapping, the linear relationship between the signal rise time and the amplitude loss is not accurate, especially for interactions near the anode or the cathode side. A rise time window is still needed to discriminate those events outside the linear range. This will cause some efficiency loss.

By measuring the signal amplitude and rise time at the same time, the digital rise time compensation can apply accurate compensation for the signal amplitude loss according to its rise time. An energy resolution of 5 keV FWHM at 662 keV was obtained for a 4 mm × 4 mm × 2 mm CdTe detector without rejecting any events [Red96].

Another technique is the signal waveform analysis [Tak96]. This method first digitizes the signal waveform for each event, then compares it with the precalculated waveforms from different depths to determine the signal interaction depth. Once the interaction depth is determined, the signal amplitude loss is corrected according to the charge collection efficiency from that depth.

All these energy enhancement techniques rely on the correlation between the signal amplitude loss with its rise time or waveform. For multiple interaction events, the output signal is the superposition of signals from different depths. The correlation between the signal amplitude loss with its rise time or waveform for single interaction events is different from that for multiple interaction events. These amplitude compensation techniques will cause spectrum distortions in this case. As the gamma-ray energy increases and the detector volume increases, the multiple interaction probability will increase, and this problem will become more severe.

4.2.2 Coplanar Grid Detectors

A similar problem with low ion mobility also exists for ionization gas detectors. In ionization chamber detectors, this problem was successfully overcome by using a Frisch grid very close to the anode. Due to the shielding effect of the Frisch grid, when the electrons and ions drift in the detector volume between the cathode and the Frisch grid, there is no induced signal on the anode. Only after the electrons pass through the Frisch grid, an induced charge is generated on the anode. The anode signal is mainly determined by the electrons collected by the anode.

For semiconductor detectors, it is not practical to fabricate a physical Frisch grid inside the crystal close to the anode surface. A novel detector design, the coplanar grid detector, was introduced in 1994 by P. N. Luke [Luk94]. As shown in Figure 4.3, there are two sets of interconnected anode electrodes. A small bias voltage is applied between them. When the charge carriers drift through most of the detector volume,

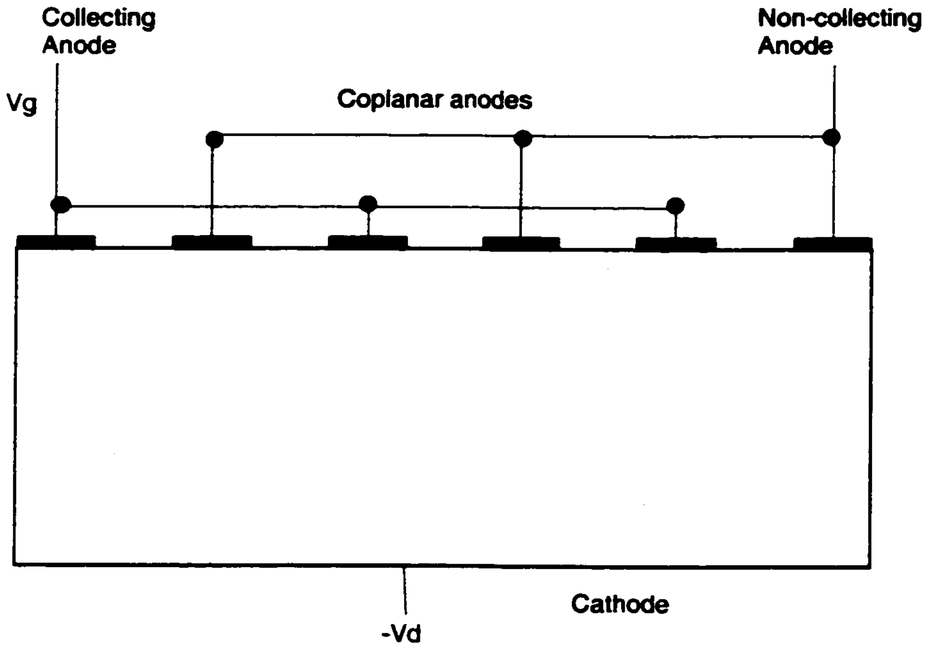

Figure 4.3: Geometry of a coplanar grid detector. V_d is the cathode bias and V_g is the bias between the two anodes.

they will induce the same signal on both anodes. But when the electrons move very close to the anode surface, due to the small bias between the two anodes, the electrons will move towards the anode with the higher potential. This anode is often referred to as the collecting anode, and the other anode as the non-collecting anode. The weighting potential for the collecting and the non-collecting anode is shown in Figure 4.4. The effective weighting potential for the difference signal is also shown in Figure 4.4, which is identical to the weighting potential for a Frisch grid detector. Due to the symmetry between the collecting and non-collecting anodes, the weighing potential for the difference signal is zero until very close to the anode surface, then quickly increases to 1. Thus, the difference signal is mainly determined by the number of electrons collected by the collecting anode for interactions taking place in most of the detector volume. This design thus effectively achieves single

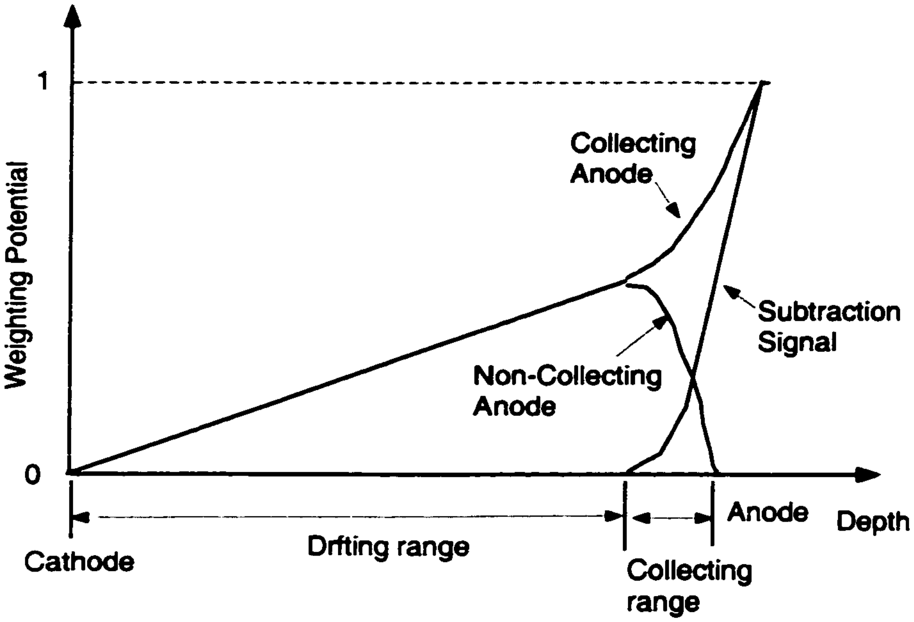

Figure 4.4: The schematic illustration of the weighting potential for a coplanar grid detector.

polarity charge sensing. A 1.8% energy resolution at 662 keV has been achieved for a $1cm^3$ coplanar grid cubic CdZnTe detector [He97].

The single polarity charge sensing of the coplanar grid detector relies on the symmetry between the collecting and non-collecting anodes. This symmetry condition is satisfied in the central region of the detector. But for interactions near the detector edges, the asymmetry between the two anodes will degrade the detector energy resolution. In order to reduce the influence of this asymmetry to the energy resolution, the anode grid pattern needs to be carefully designed to minimize the unbalance between the anodes [He98].

The coplanar grid anode design effectively overcomes the hole trapping problem. However for thick detectors, the electron trapping can not be neglected. For a 1 cm thick CdZnTe detector under a normal cathode to anode bias of 1500 V the electron trapping can be 5-10%. Two techniques have been used to overcome electron

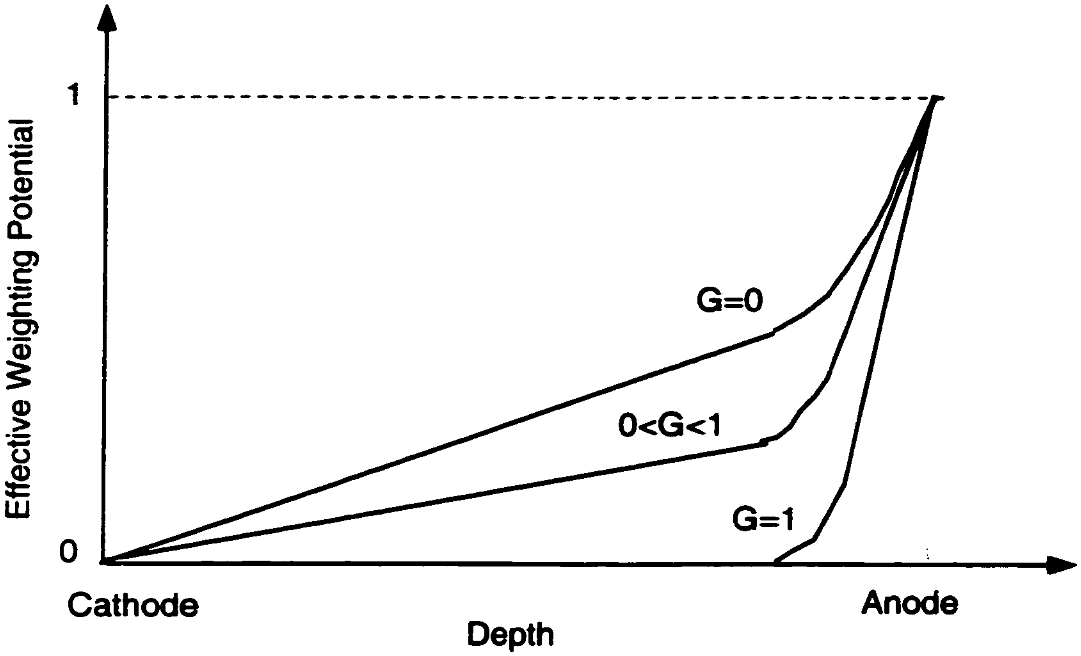

Figure 4.5: The schematic illustration of the effective weighting potential for a coplanar grid detector with different gain, G, for the non-collecting anode.

trapping. The first method was introduced by P. Luke [Luk96]. Instead of using a unity gain for subtraction between the collecting and non-collecting anodes, a gain G ($0 < G < 1$) is applied to the non-collecting anode. As shown in Figure 4.5, the effective weighting potential in the drift region has a small slope. Therefore, the induced signal for interactions near the cathode side will have a larger amplitude. On the other hand, due to electron trapping, there are fewer electrons that can drift to the anode. Under proper conditions, if these two effects compensate for each other, then the difference signal will have a depth independent amplitude. As the weighting potential is determined by the anode grid pattern, once a detector is fabricated, the effective weighting potential distribution for the difference signal can only be changed by adjusting the gain, G, for the non-collecting anode. The electron trapping behavior is mainly determined by the crystal properties and the operating electric field inside the detector. For a specific detector, it is only possible to change this behavior by changing the detector bias voltage, thus subjecting it to other operational constraints such as the leakage current consideration. Therefore, compensation of these two effects can not be achieved for all detectors. A more flexible and accurate method is to use the depth sensing technique introduced by Z. He [He96]. Knowing the interaction depth for each interaction, any arbitrary correction for the electron trapping can be applied to the measured difference signal amplitude.

The coplanar grid design has been very successful. Commercial CZT detectors with up to $1cm^3$ volume are available with energy resolution around 2-3%, much better than the commonly used NaI scintillation detectors. However for larger area detectors, the leakage current and capacitance between the collecting and non-collecting anodes will increase as the detector area increases. Thus the electronic noise will increase. The material non-uniformity is also an energy resolution degradation factor. Therefore, the coplanar grid can not be used for large volume detectors.

4.2.3 Pixellated Detectors

Single polarity charge sensing can also be achieved by the small pixel effect [Bar95]. As shown in Figure 4.6, when the anode pixel dimension is small compared with the detector thickness, the weighting potential for the anode pixel has a small slope in the most of the detector thickness, then has a steeper slope near the anode. When the charge carriers drift in the most of the detector volume, the induced signal on the anode pixel is small. When the charge carriers drift near the anode surface, where the weighting potential has a steep gradient, the majority of the induced charge will be generated on the anode pixel. For interactions not very

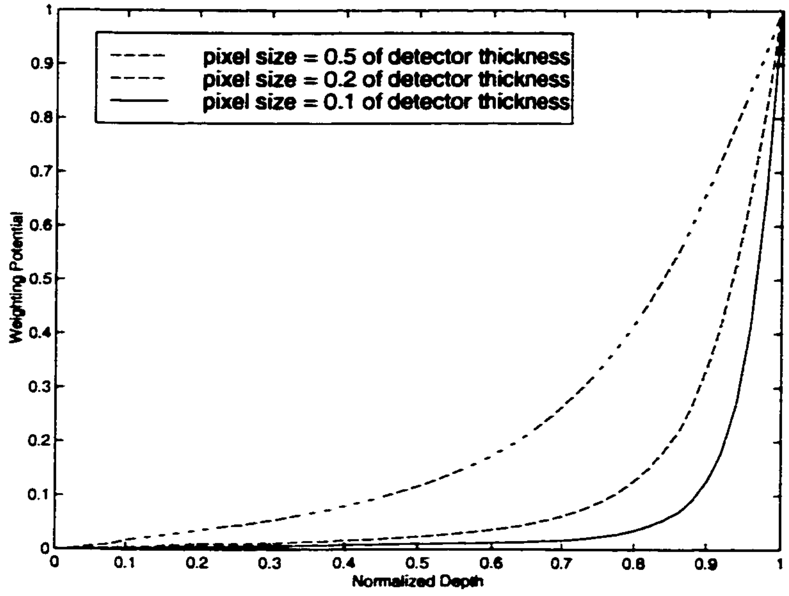

Figure 4.6: Weighting potential distribution for pixellated detectors with different pixel size. This is the calculated results from COULOMB [Cou] with boundary conditions that set the potential of the pixel of interest to unity, and the potential of all other pixels and the cathode to zero.

close to the anode surface, the signal amplitude is mainly determined by the number of electrons collected by the anode pixel. Thus, due to this small pixel effect, the pixellated detector can effectively overcome hole trapping. As shown in Figure 4.6, in order to have a strong small pixel effect, the ratio between the pixel size and the detector thickness has to be small. The anode needs to be divided into many small pixels. Each of these anode pixels has to have its own independent signal readout electronics. Implementation of such a readout system using discrete electronics was too expensive and impractical several years ago. However as the technology progressed in the semiconductor industry, the integrated ASIC chips with multiple signal processing channels have become readily available, such as the VA1 series from Integrated Detector & Electronics AS (IDE AS). The availability of these readout electronics makes the pixellated detector an effective, practical way to mitigate the severe hole trapping problem. A 1.5% energy resolution at 662 keV has been obtained with a $1cm^3$ CdZnTe detector using this technique [He99].

Since the anode is divided into many pixels, the leakage current between the cathode and the anode is shared by these small pixels. The leakage current for each pixel is much smaller than that for a planar detector with the same area. The capacitance for each pixel is also much smaller. Therefore, theoretically the electronic noise should be smaller for pixellated detectors than that for conventional planar or coplanar grid detectors. However the electronic noise of the current available integrated readout ASIC is higher than that for discrete readout systems. The potential advantages for pixellated detectors have not been realized. Yet as the technology in the integrated semiconductor industry progresses, the electronic noise for readout ASIC chips should decrease over time.

4.2.4 Other Single Polarity Sensing Detectors

Other detector geometries such as coaxial, hemispherical [Zan77], drift detectors [Pat96], and geometrically weighted trapezoidal detectors [McG99] can also partially achieve single polarity charge sensing. For all these geometries, the weighting potential peaks towards to the anode. Thus the electron contribution to the anode is larger than that for the holes for most events. Due to the geometrical effect for coaxial, hemispherical, trapezoidal geometries, more detector volume is located in the region near the cathode, so more interactions take place in the region where holes have small contributions. These two effects make these detector geometries have better energy resolution than conventional planar devices. However, due to the fabrication difficulties and poorer resolution than that for coplanar grid or pixellated detectors, these geometries are not widely used.

4.3 3-D Position Sensing using Pixellated Detectors

Severe hole trapping is a major problem for CZT, CdTe and other compound semiconductor materials. However, a novel use of this property by Z. He et al. [He96] can provide very useful information: the interaction depth. As shown in Figure 4.1, when neglecting the edge effect, the weighting potential for a planar electrode is a linear function from the cathode to the anode surface. If the holes can only travel a short distance, their contribution to the cathode can be neglected and the cathode signal amplitude is mainly determined by the number of electrons and the interaction depth, i.e.

$$Q_c = eN_eZ. \tag{4.5}$$

From the analysis in the last section, the difference signal for coplanar grid detectors or the anode pixel signal for the pixellated detectors is mainly determined by the number of electrons being collected, i.e.

$$Q_A = eN_e. \tag{4.6}$$

Therefore, the ratio between the cathode and the anode signals

$$C/A = Q_c/Q_A = Z, \tag{4.7}$$

which is independent of the interaction energy and a direct measurement of the interaction depth.

For a detector with a pixellated anode and a planar cathode, this depth sensing technique can be used together with the small pixel effect for pixellated detectors. The energy information is given by the anode pixel's amplitude. The lateral position information is given by the pixels that have response. The depth information can be obtained from the ratio of the cathode to the anode signal. This three dimensional position sensitive capability is not only very useful for many imaging applications, but also makes it possible to apply 3-D material non-uniformity and electron trapping corrections [He99]. This material nonuniform correction capability can relax the requirement for material uniformity in building large volume detectors.

As shown in Figure 2.10, the CZT needs to be more than 1 cm thick for maximum Compton aperture efficiency (CAE) above 300 keV. For such a thick detector, without the depth sensing capability, the distance between the two detectors has to increase in order to reduce the detector thickness contribution to the angular uncertainty. Thus the overall camera efficiency will be reduced. With the 3-D sensing capability, the maximum CAE can be achieved without sacrificing the overall camera effiency. The 3-D material non-uniformity and electron trapping correction capability is also helpful to improve the overall angular resolution by improving the overall energy resolution.

CHAPTER V

SYSTEM SETUP AND INDIVIDUAL DETECTOR CHARACTERIZATION

5.1 System Setup

As shown in Figure 5.1, the prototype Compton scattering camera is composed of two 1 cm^3 3-D position sensitive CdZnTe detectors [He99]. According to the performance estimation in Chapter 2, when the central distance between the two detectors is 5 cm with a central scatter angle of 50° (corresponding to 20° to 80° scatter angles) the system will have its best angular resolution. Therefore, the center to center distance between the two detectors is fixed at 5 cm. The center of the field of view (FOV) is located on the front surface of the instrument box, 50° relative to the centers of the two detectors. Since there is only one second detector for this prototype camera, the source plane needs to rotate around the center of the FOV to get adequate azimuthal sampling. In order to reduce the pick up noise from the ambient environment, the preamplifiers, detectors, and repeater cards are all housed in an aluminum instrument box. By shielding the repeater cards, the electronic noise on the anode grid signal is much smaller than that in the first generation DAQ system. The improved signal-to-noise ratio enables us to reduce the anode grid trigger threshold from above 100 keV to below 30 keV. This low threshold enables

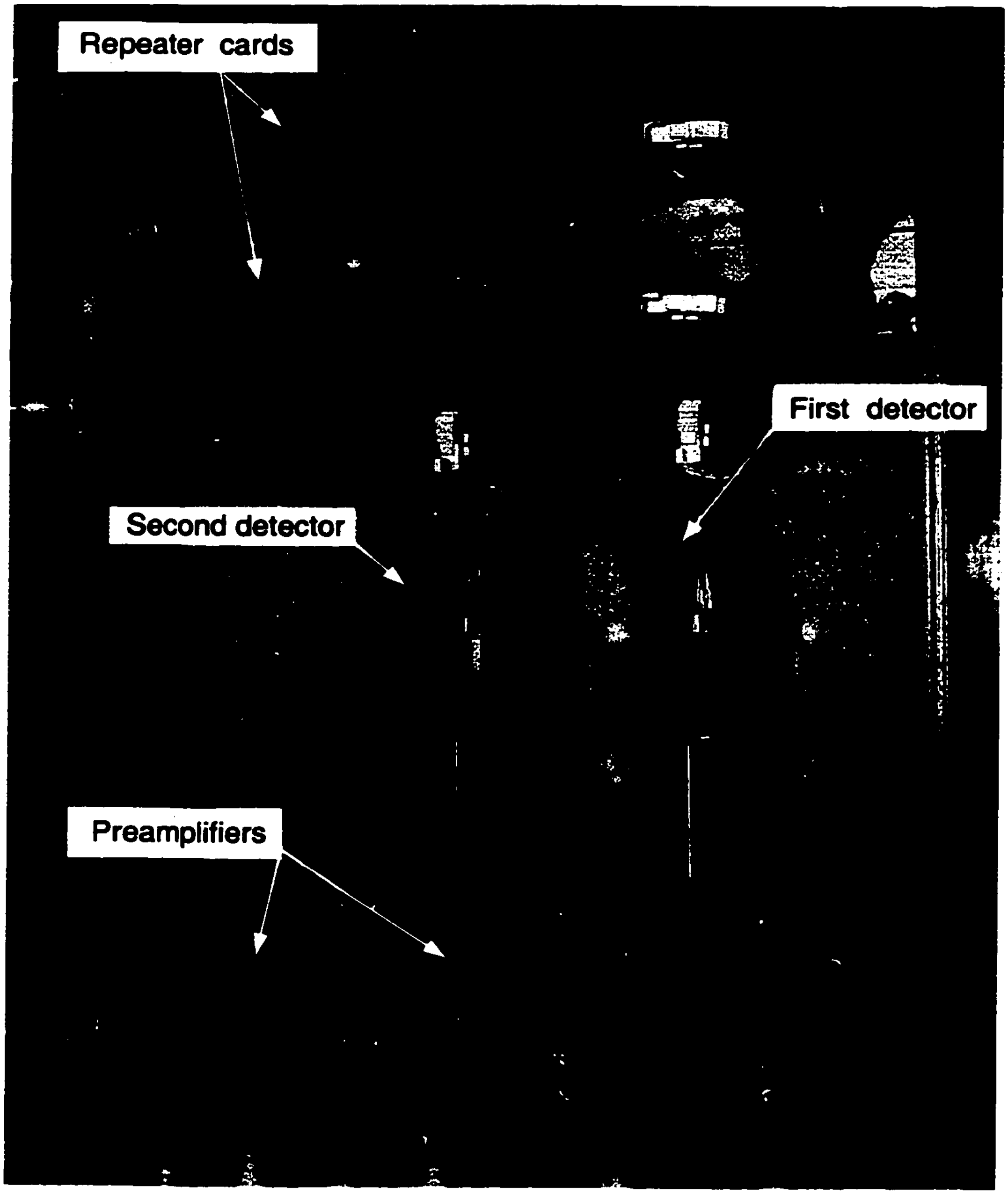

Figure 5.1: Picture of the CZT Compton scattering camera.

us to get the energy spectra from low energy gamma rays, such as the Am-241 59.5 keV gamma ray or the Co-57 122 keV gamma ray, irradiated from either the anode or the cathode side. This low threshold also enables us to collect coincident data from even 20° scatter angles as desired.

There are 11 × 11 pixels on the anode surface. The 11 × 11 array covers an area of 7.8 mm × 7.8 mm on the 10 mm × 10 mm CdZnTe anode surface. Each pixel has a dimension of 0.7 mm × 0.7 mm, with an anode of 0.2 mm × 0.2 mm at the center. A 0.1 mm width anode grid surrounds each of these anode pixels. Since a negative bias is applied to the anode grid, it acts like a non-collecting anode in coplanar grid detectors. The electrons will be collected by anode pixels. The anode pixels are first wire-bonded to a fanout ceramic plate which is then wire-bonded to the VA1 inputs through an RC chip. There are 128 channels of resistors and capacitors in one RC chip. Figure 5.2 shows a complete detector unit with a hybrid board. For each interaction, the energy and lateral (x,y) position is read out by an integrated ASIC VA1 chip. The depth information is given by the ratio between the cathode and anode pixel signals.

5.2 Data Acquisition Hardware

The overview of the data acquisition system for the camera is shown in Figure 5.3. The anode pixels from each detector are AC coupled to a VA1 chip. The hybrid board provides the physical support for the VA1 chip and fanout connections between the VA1 and the repeater card. The repeater card provides various biases and supplies power to the VA1 chip. It also provides the signal level conversion and analog output driver circuit. Working with the externally provided test level, the repeater card can also generate a test pulse to test the VA1 chip. In conjunction with the

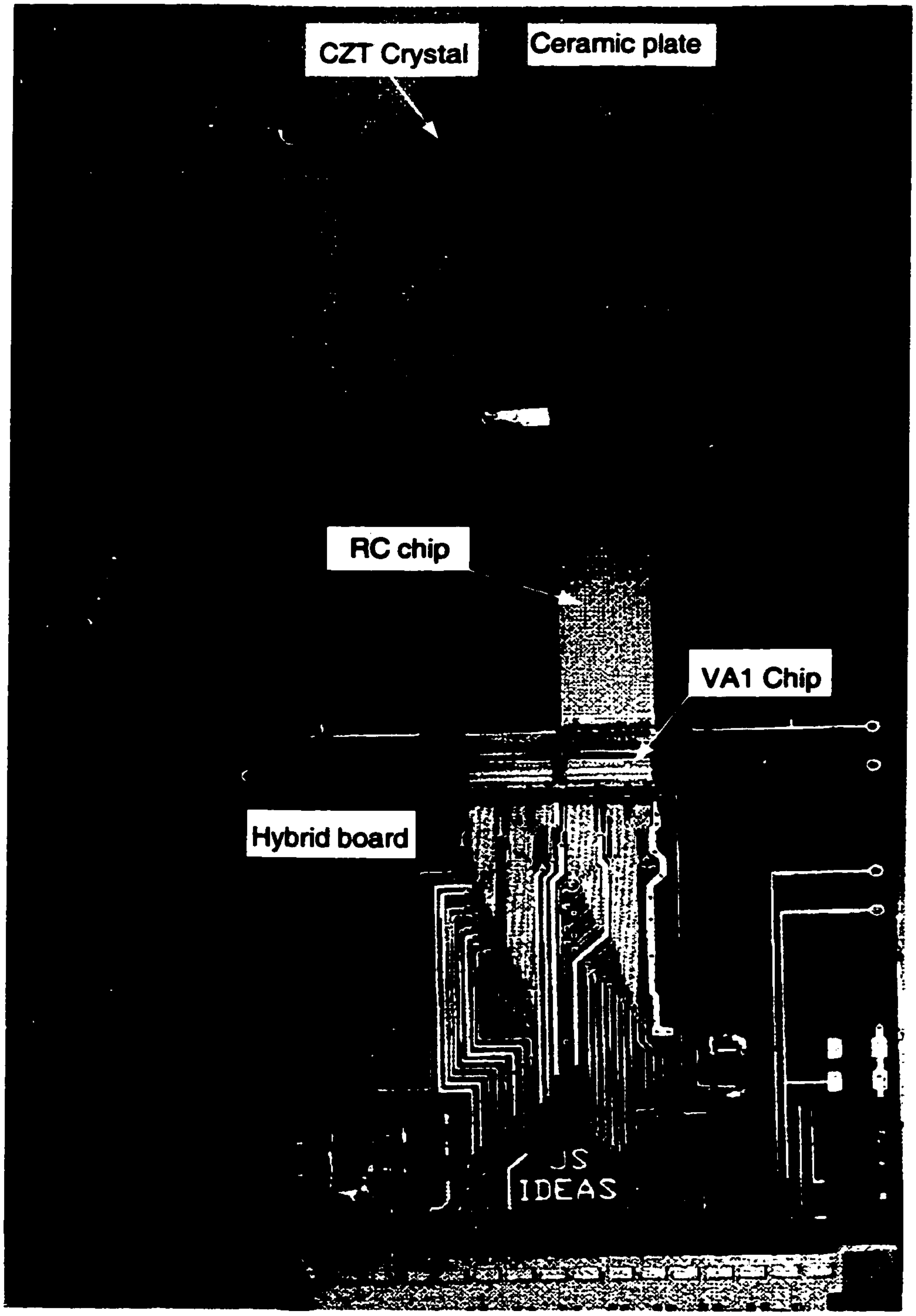

Figure 5.2: Picture of a 3-D CZT detector.

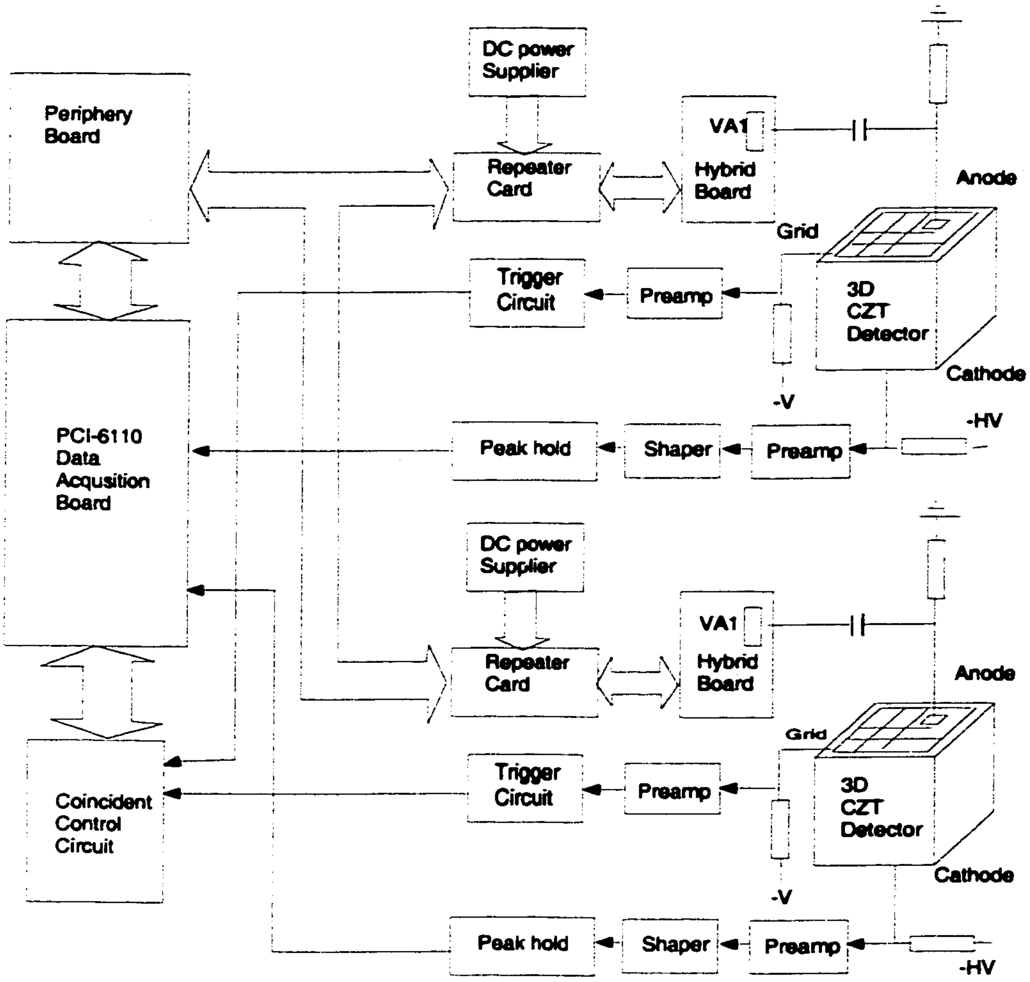

Figure 5.3: Data acquisition system block diagram.

Data Acquisition Board, PCI-6110, the periphery board generates all digital control signals and coordinates the data acquisition of the two 3-D CdZnTe detectors. The periphery circuit also performs the TTL to the differential TTL conversion for all digital control signals sent to the repeater cards. Working in the differential TTL mode helps to suppress common mode pickup interference. The cathode signal from each detector is processed by a discrete preamplifier, a shaping amplifier, and a peak-hold circuit, and is then read out by another analog input channel to get the interaction depth. The anode grid signal is processed by a preamplifier, fast shaping

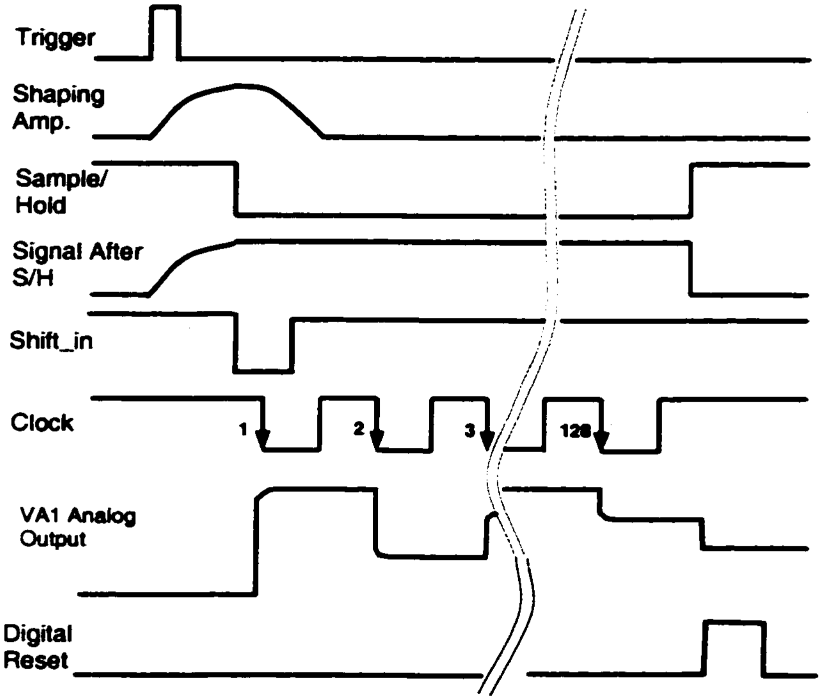

Figure 5.4: The major control signals for the VA1 chip.

amplifier, and trigger circuit to generate the trigger signal. The coincidence control circuit is controlled by the DAQ board, PCI-6110, to enable the system to work in different modes.

There are 128 independent signal processing channels in one VA1 chip. Each channel has its independent preamplifier, shaping amplifier and sample/hold circuit. In order to reduce the number of output connections, the analog outputs from the sample/hold circuits of the 128 channels are read out serially through a multiplexer built on the chip. Although this design simplifies the connection for the data acquisition system, for each interaction all 128 channels need to be serially read out. This greatly increases the system dead time. The major control signals for the VA1 operation are shown in Figure 5.4. For each event, a trigger signal is needed to start its operation. Then a sample/hold signal is needed for the sample/hold circuits to simultaneously capture the peaks of the shaping amplifier outputs. After that, a shift_in signal is needed to enable the clock signal to switch the output multiplexer from one channel to another. After all 128 channels have been serially read out, the sample/hold signal needs to return to the high level to discharge the sample/hold circuits, and a digital reset signal is needed to reset the VA1 for its next operation.

Since the VA1 does not have self-trigger capability, an external trigger signal is needed to start its operation. From Figure 5.4, it is clear the delay time between the trigger and the sample/hold signal is critical for the sample/hold circuit to correctly capture the peak of the shaping amplifier output. A trigger signal that has a constant timing relative to the shaping amplifier output is needed. This trigger ideally should be generated from the anode pixel signals themselves. However the anode pixel signals are not accessible to an outside circuit. It is not possible to generate the trigger or the sample/hold signal from the anode pixel signals. The only choice is to use the cathode signal or the anode grid signal. As analyzed in Section 4.3, the anode pixel signal is mainly induced when the charge carriers move very close to the anode pixel due to the small pixel effects. However the cathode electrode is a conventional planar geometry. The cathode signal starts as soon as the electrons start drifting. For interactions that take place at different depths, the delay time between the cathode signal and the anode pixel signal is different. Therefore, the cathode signal can not be used to generate the trigger signal unless most interactions have similar depths, such as for low energy gamma rays since most interactions would take place near the irradiation surface. Since a small negative bias is applied to the anode grid, it acts like a non-collecting anode in coplanar grid detectors. As shown in Figure 5.5, a transient signal is induced on the anode grid. When the electrons drift towards the anode surface, the induced charge begins to generate a signal on

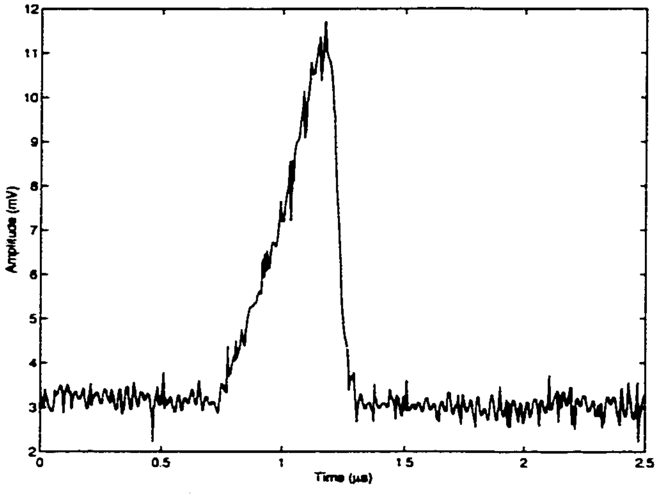

Figure 5.5: The measured waveform of the anode grid signal. The falling edge coincides with the electron collection by the anode pixels.

the anode grid. When the electrons are being collected by anode pixels, the induced charge on the anode grid quickly drops to zero. The falling edge of the anode grid signal coincides with the electrons drifting near the anode and being collected by the anode pixels. Therefore, the anode grid signal is used to generate the trigger signal from its falling edge by a fast shaping and trigger circuit.

For multiple interaction events, if these interactions take place at different depths, the electron drift times to the anode pixels are different. The trigger signal from the anode grid coincides only with the electrons collected by the anode pixel with the shortest drift time. So the sample/hold timing is only correct for this pixel. We can only get the correct signal amplitude for this pixel, and will miss the correct amplitudes for other pixels. Therefore, under the current VA1 working mode we can only measure the correct signal amplitude for single pixel events.

For Compton scatter imaging, the two detectors need to work in coincidence mode. For ordinary detectors, if two detectors work in coincidence mode, a natural

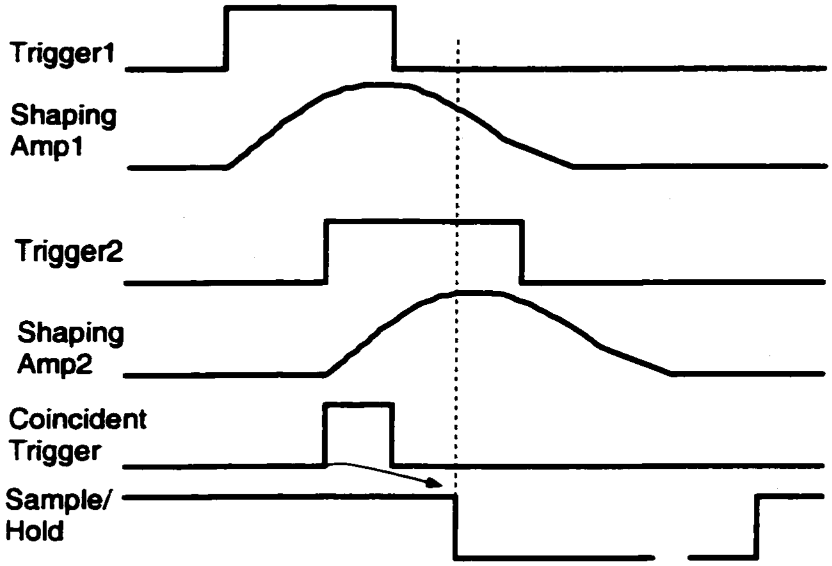

Figure 5.6: Timing problem for coincident events. Even if we set the correct delay between the coincidence trigger and the sample/hold signal, we can only capture the correct signal amplitude from one detector.

choice is to use the coincidence signal between two detectors to control the data acquisition. For the CZT detectors, the electron mobility is around $1000cm^2/Vs$. Under the normal bias between the cathode and the anode of 2000 V, the electron drift time from the cathode to the anode is around 500 ns. The actual measured drift time is even longer than this estimation. Even for true coincident events, if the interactions in two detectors have different depths, the trigger signals from the two detectors will have different timing. As shown in Figure 5.6, suppose the coincidence signal is the overlapping signal between the two triggers from both detectors. Even if we set the correct delay between the coincidence trigger and the peaking time of the shaping amplifiers, at best we can only capture the correct signal amplitude for one detector, and miss the peak for the other. So we can not use the coincidence trigger to generate the sample/hold signal for both detectors. In order to measure the correct signal amplitude for both detectors, each detector has to use its own trigger signal to generate the sample/hold signal. For each event, the DAQ system needs to serially read out all 128 channels from the VA1 chip. In the experiments, we found the maximum readout clock frequency is around 3×10^4 Hz before outputs interfere between neighboring channels occurs. Thus the total time to read out 128 channels is around 4.3 ms. Since the individual detector count rate is much higher than the coincident count rate, if each detector has to hold the VA1 for such a long dead time with or without coincident event, the system dead time will be dominated by the single detector events. We will not be able to collect much coincident data during imaging data acquisition. In order to reduce the dead time due to single detector events, each detector should quickly reset itself for non-coincident event. On the other hand, for coincident events, both detectors should hold the VA1 long enough for all 128 channels from each detector to be serially read out.

Besides these timing and hold problems, the DAQ for the camera should enable the system to work in three different modes: 1. Test mode to measure the electronic noise and test the VA1 response for each channel. 2. Single detector mode to characterize and calibrate each detector. 3. Coincidence mode for Compton scatter imaging data acquisition. For ease of operation, the switch between each mode should be controlled from the DAQ software.

Considering all the above requirements, the design of the periphery control circuit is shown in Figure 5.7. The coincidence trigger signal is the output from a specially designed coincidence control circuit. Controlled by three digital I/O signals from the PCI-6110 DAQ board, the coincidence control circuit can select trigger signals from either individual detector, coincidence of both detectors, or no trigger signal output for the test mode. The trigger signal for each detector generated from its anode grid signal is used to control a general purpose counter on the PCI-6110. A delayed output

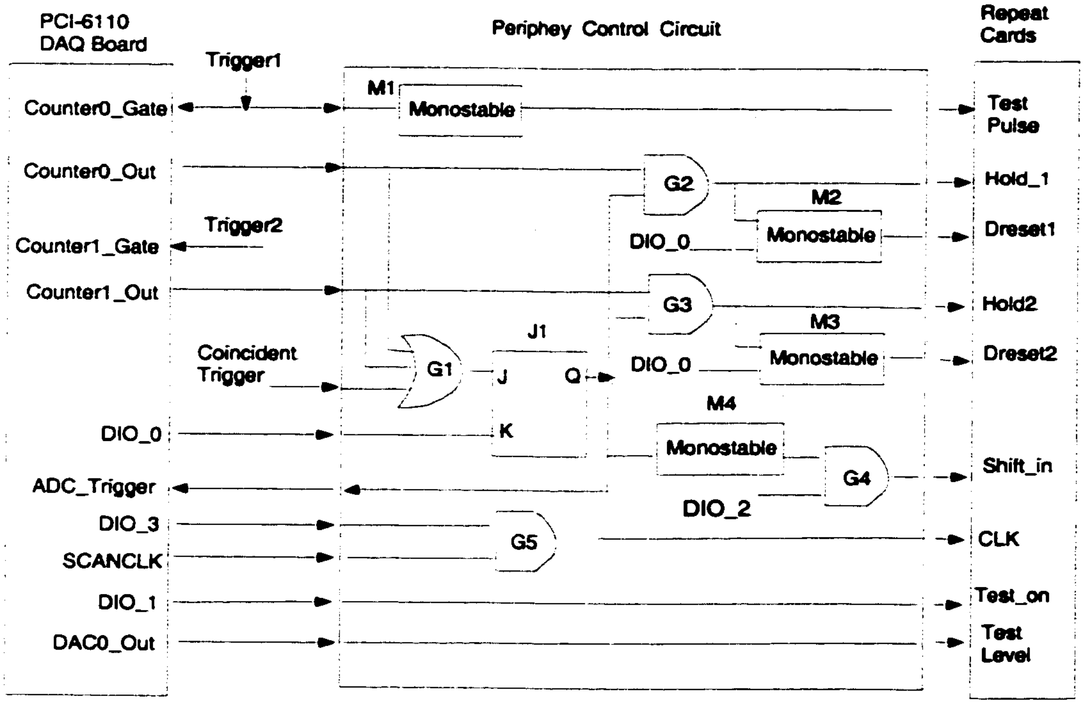

Figure 5.7: The periphery control circuit.

from the counter is used as the sample/hold signal for each detector. The delay time and hold time can be easily adjusted by software. The delay time for each detector needs to set to coincide with the peaking time of its VA1 shaper. Since the delay and hold time from the counters output is based on a 20 MHz clock on the DAQ board, the maximum time uncertainty due to this timing clock itself is 50 ns. In coincidence mode, as shown in Figure 5.8, both detectors use their own sample/hold signals to correctly capture their signal amplitude. Each detector only needs to hold itself for a very short time to wait for the other detector's trigger and the coincidence trigger signal to come. After that, the actual hold time is controlled by the J-K flip-flop, J1, which is set to a low level by the coincidence trigger signal after both detectors have been in the hold states. The falling edge of J1 is used to trigger the A/D conversion of the DAQ board and to generate a shift_in signal by the monostable chip, M4, for

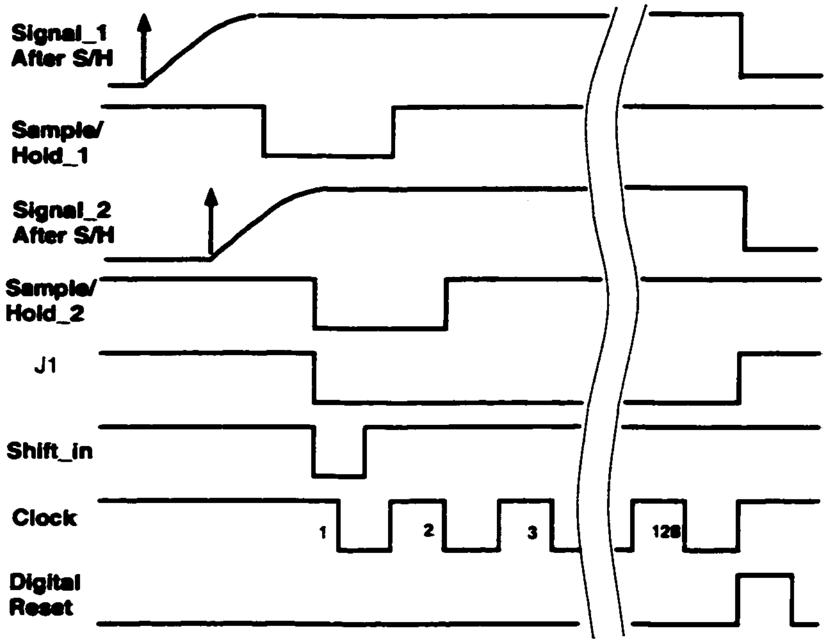

Figure 5.8: Control signals for coincident events

both detectors. The SCANCLK signal from the PCI-6110 is used as the clock signal to switch VA1 channels. Since the SCANCLK signal is generated by the PCI-6110 shortly after the sample is taken by the DAQ board, using it as the switch clock can make sure each VA1 channel is correctly sampled by the DAQ board. The frequency for SCANCLK can be easily controlled from the software by setting the sample rate for the DAQ board. After all 128 channels have been read out, J1 is set to high level by DIO_0 to discharge the VA1s for both detectors. Digital reset signals are generated by the monostable chips, M2 and M3, to reset both VA1s. On the other hand, if only one detector has a trigger signal, as shown in Figure 5.9, since J1 is in high level, gates G2 and G3 are open, the output from the general purpose counter is directly used as the sample/hold signal. After holding for a short time, the sample/hold signal returns to high level to discharge the VA1. The rising edge from the sample/hold signal is also used to generate a digital reset signal to reset the

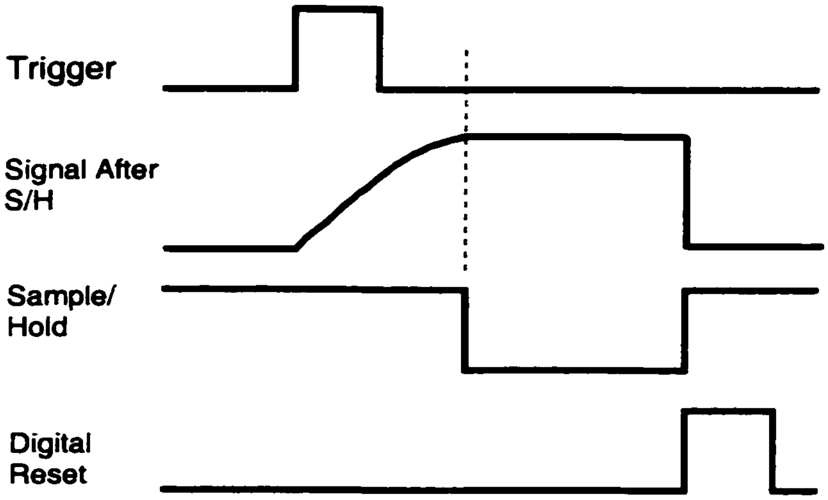

Figure 5.9: Control signals for single detector events.

VA1. Therefore, under this design, both detectors can capture their correct signal amplitudes for coincident events while resetting quickly for single detector events to avoid the single detector events that would dominate the system dead time.

In the individual detector mode, the counter for the other detector is turned off by the software and the trigger signal for the detector itself is selected by the coincidence control circuit to control the J1. Other signals work in the same fashion as in the coincidence mode.

In the test mode, a test pulse from the pulse generator is connected to the trigger 1 input to generate a test pulse from the monostable chip, M1. The actual test pulse injected into the preamplifiers on the VA1 is generated on the repeater card. Its amplitude is controlled by the test level, which is the output from the digital to analog converter output, DAC0_Out, and can be set by the software. In the test mode, the DIO_2 is used to generate a shift_in signal and DIO_3 is used to generate the CLK signal for the VA1s. DIO_2 and DIO_3 work together to select the test channel for the input and output multiplexers. Once a test channel is chosen, its response to the test pulse can be read out by the DAQ board. By turning on or off the sample/hold counter from the software, the VA1 output waveform before or after the sample hold circuit for each chip can be checked. Its peaking time can be measured in order to make sure the correct delay between the trigger and the sample/hold signal is set.

5.3 Data Acquisition Software

As pointed out earlier, under the current working mode, the VA1s can not capture correct signal amplitude for multiple pixel events. So in the data acquisition software, we only record the information for single pixel events for both detectors. The major data acquisition software was written in Borland C++. The flow chart of the program is shown in Figure 5.10. In order to minimize the additional time associated with the data processing, during the data acquisition only one overall spectrum from whole detector is accumulated and displayed for visual inspection. The user can check this spectrum to make sure it looks reasonable. For each event, the pixel channel number, anode pixel signal, and cathode signal amplitude are written to a disk file for off-line data processing.

All the off-line data processing codes were written in Matlab. During off-line data processing, the anode signal amplitude is first corrected for non-uniform gains of the VA1's different channels. Then, three-dimensional spectra for 11 × 11 × 20 voxels for each detector can be accumulated based on the pixel number and the cathode to anode signal ratio. After that, the voxel-based electron trapping and material non-uniformities can be corrected. A spectrum for the whole detector can be obtained.

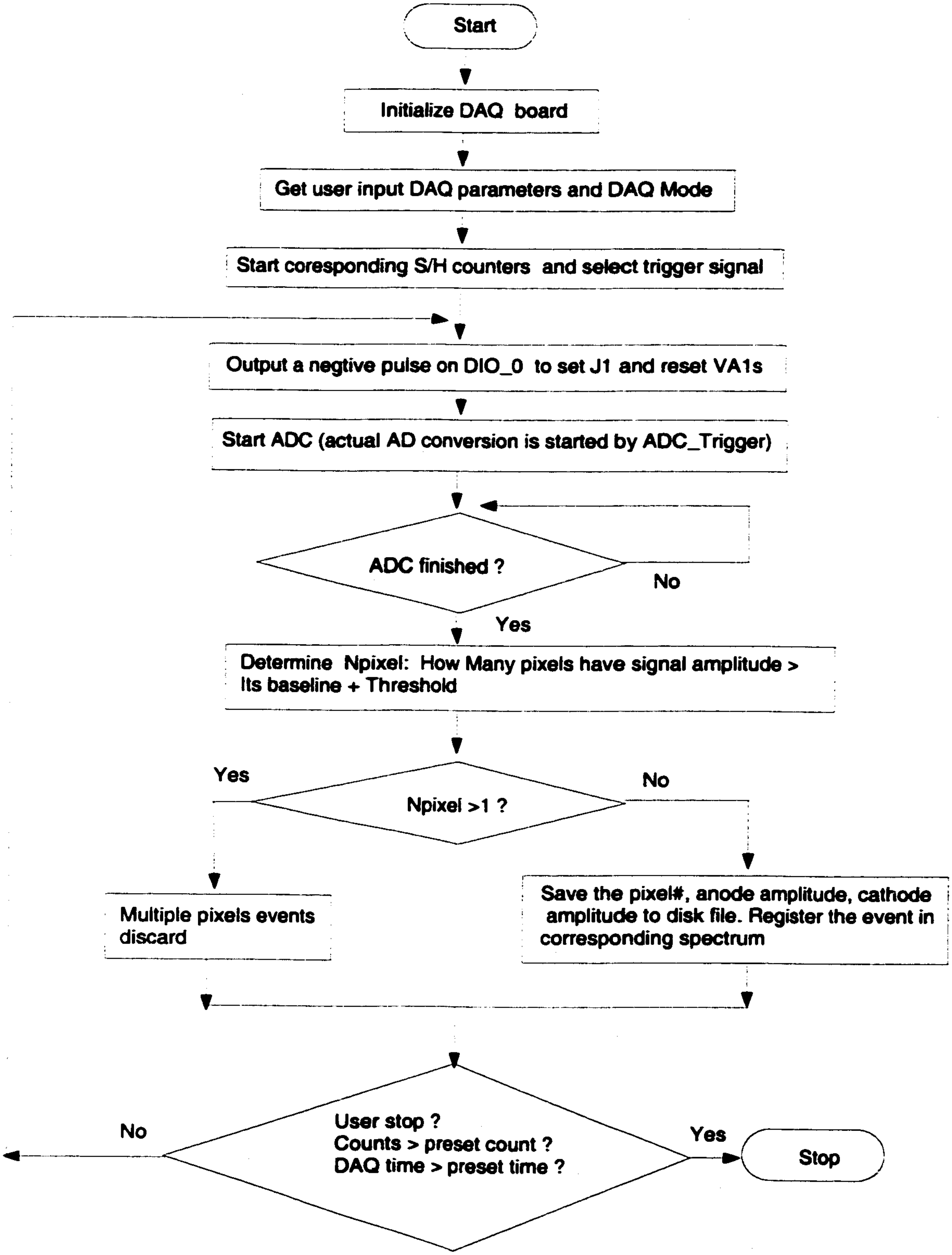

Figure 5.10: Flow chart of the DAQ Software.

5.4 The First Detector Characterization

5.4.1 Electronic Noise and Test Pulse Response

Under the first generation DAQ system, DC coupling between the anode pixels and the VA1 chip was used. The estimated electronic noise from the base line fluctuation was around 3 keV before applying bias voltages to the detectors. The electronic noise increased to around 6-7 keV after applying the bias voltages [Li99]. In order to reduce the leakage current contribution to the electronic noise, AC coupling between the anode pixels and the VA1 chip was implemented for both detectors. Figure 5.11 is the measured equivalent noise FWHM of the baseline fluctuation for the first detector before applying the bias voltages and under two bias conditions. Under the new AC coupling, it is clear in Figure 5.11 the electronic noise has a similar value under different bias conditions. Since our detector only has 121 anode pixels, the VA1 channels 1 - 5, 127 and 128 are left open. The electronic noise for these open channels is only around 1.5 keV. For other channels connected to the detector anode pixels, due to the increased capacitance from wire-bonding and anode pixel capacities, the electronic noise increases to 2.5-3 keV for most channels. This 3 keV electronic noise approaches the manufacturer's performance specification for the VA1. Figure 5.12 is the VA1 output amplitude fluctuations for the test pulse when the test level equals -4.1V, cathode bias V_c =-2000V and anode grid bias V_g =-50V. The test results under other different bias conditions or different test level also have similar fluctuations. Although the test level is controlled by the digital to analog converter output, DAC_0, on the DAQ board, its noise is only 1 mV RMS. The actual test pulse injected to the VA1 preamplifier inputs is generated on the repeater card. The measured test pulse noise is the quadratic summation of the noise of the VA1 chip and the test pulse noise. The measured noise in Figure 5.12 is an upper

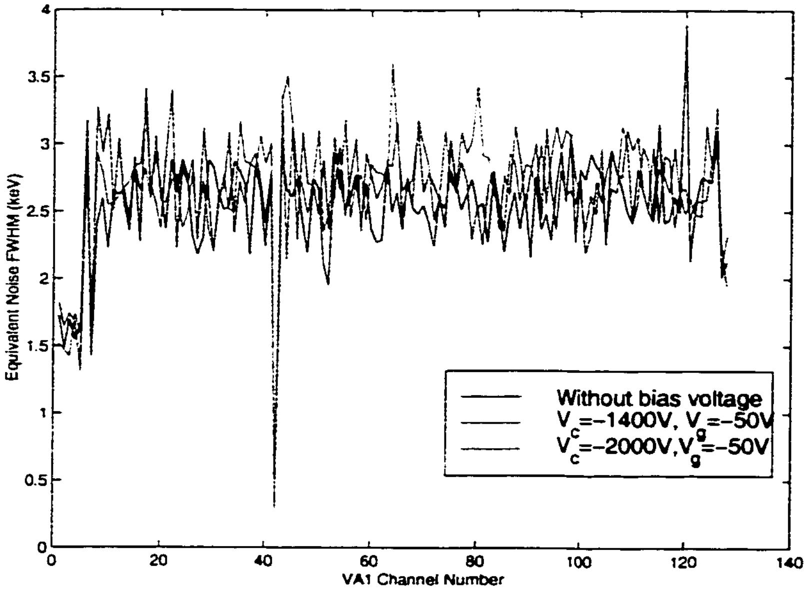

Figure 5.11: The baseline noise for the first detector.

limit for the VA1 noise. We can conclude from these results that the electronic noise for the VA1 is around 3-4 keV for most channels.

The average test signal amplitudes for the VA1 chip at several test levels are shown in Figure 5.13. Four channels (42, 67, 71, 111) have smaller amplitudes than the rest of the channels. By examining the output waveforms for these bad channels, it is found the sample/hold circuits for these channels do not work properly. So these four channels are excluded in the data acquisition. For the rest of the channels, it is clear in Figure 5.13 that the gain for different channels is not uniform. Since the depth information is derived from the signal amplitudes of the cathode and the anode pixel, and all anode pixels share the same cathode signal, if different pixels have different gains from the VA1 channels, then the same C/A ratio for different pixels will represent different physical depths. A pixel by pixel depth normalization

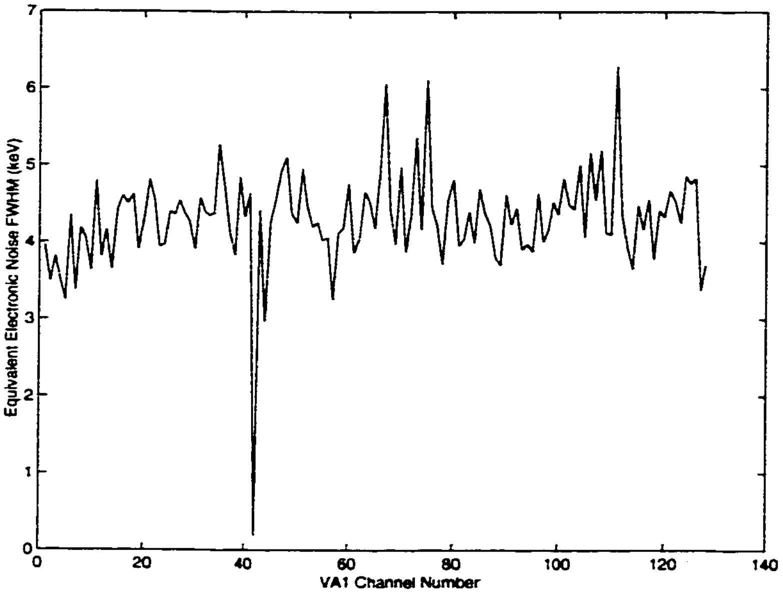

Figure 5.12: The test pulse noise for the first detector when the test level equals -4.1 V($V_c = -2000V, V_g = -50V$).

and calibration is required. This will make the depth calibration very complicated. As shown in Figure 5.14, if we get the normalization factors for all 124 good channels according their responses at the test level of -4.1 V and correct the test pulse amplitudes for other test levels, all channels have a very uniform response. If we apply these normalization factors to the anode pixel signals, the C/A ratio for different pixels will represent the same physical depth. This greatly simplifies the depth normalization and calibration.

5.4.2 Energy Spectra

All the following spectra were taken with cathode bias V_c = -2000V and anode grid bias V_g = -50V. Figure 5.15 is the Cs-137 spectrum with a $10\mu Ci$ point source irradiated from the cathode side. The FWHM is around 6.4%. A major contribution

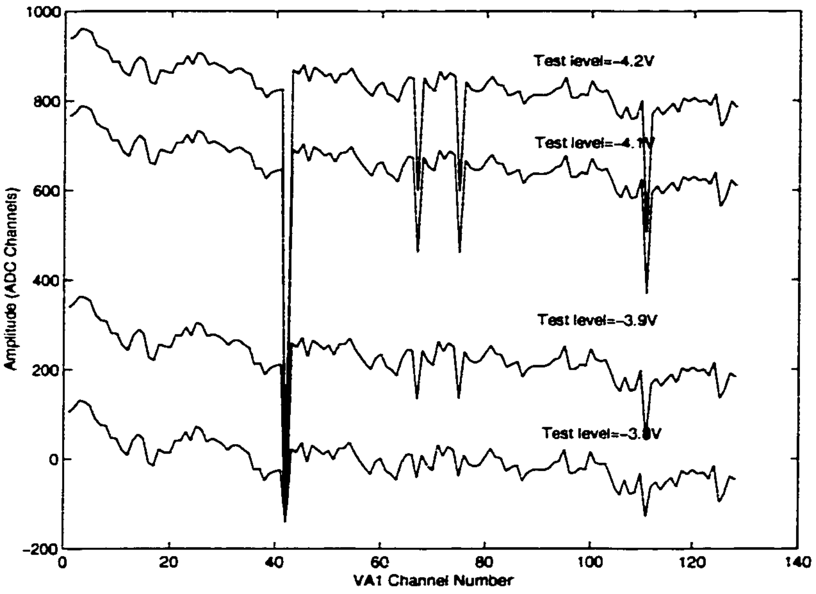

Figure 5.13: The Test pulse amplitudes for the first detector.

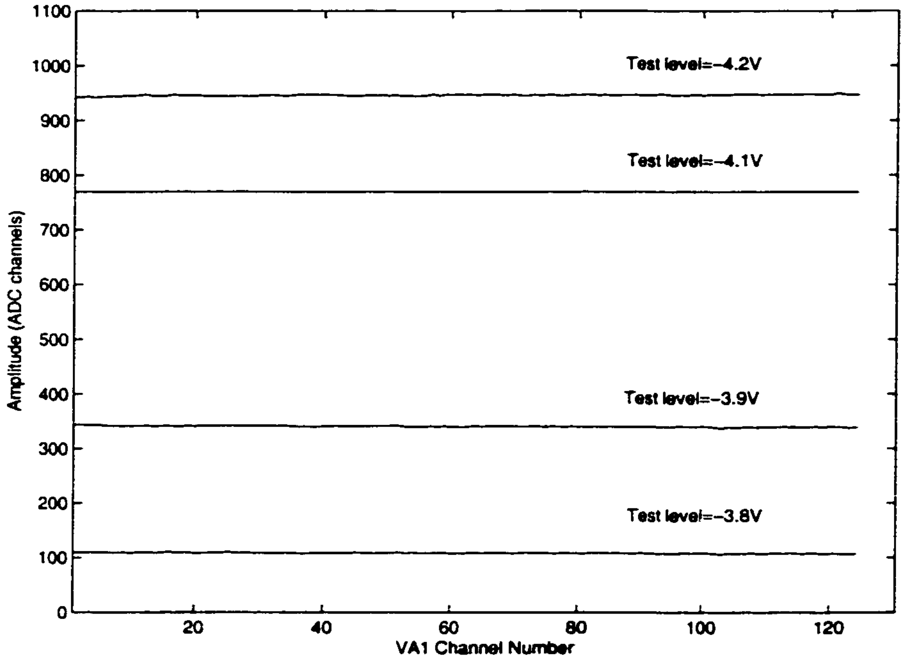

Figure 5.14: The normalized test pulse amplitude for the first detector.

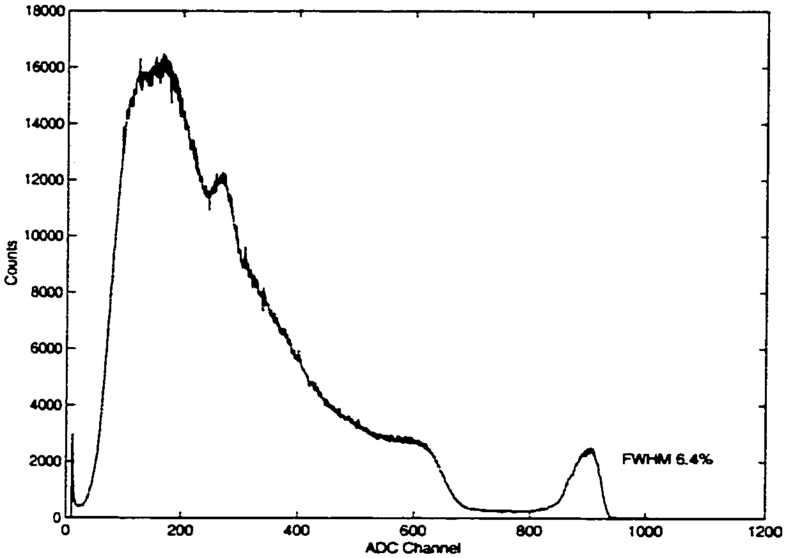

Figure 5.15: Cs-137 spectrum for the first detector before the electrons trapping and material non-uniformity correction.

to the photopeak broadening is due to the electron trapping. Figure 5.16 is the distribution of the 662 keV photopeak centroid for pixel #41 at different depth indices. The depth index 1 is corresponding to the anode side, and the depth index 20 is corresponding to the cathode side. For events very close to the anode surface (depth index 1-3), as shown in Figure 4.6, the weighting potential for the anode pixel has a steep slope. The weighting potential difference between the original position and the anode pixel becomes smaller than one. According to Equation 4.2, the induced charge will be smaller. For those events not very close to the anode surface (depth index 4 to 20), the weighting potential change from the interaction position to the anode pixel is close to one due to the strong small pixel effect. So the photopeak centroid decrease from depth index 4 to depth index 20 is mainly due to electron trapping. As shown in Figure 5.16, the photopeak centroid decreases 6.75% from

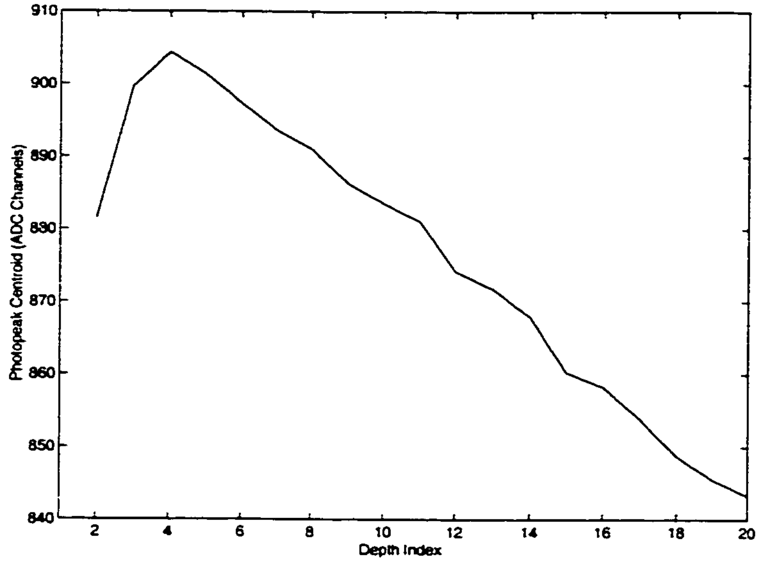

Figure 5.16: Photopeak centroid distribution for pixel #41 of the first detector. The depth index 1 represents interactions near the anode side and depth index 20 represents the cathode side.

depth index 4 to depth index 20. If we assume the operating electric field has an uniform distribution in the detector, then the electric field is 2000 V/cm inside the crystal. We assume the electron trapping follows the simple exponential function

$$N(z) = N_0 exp(-\frac{z}{\mu_e \tau_e E}), \tag{5.1}$$

where N(z) is the number of free electrons after drifting a distance z. Since the 1 cm detector thickness is divided into 20 depth indices, if we assume a simple linear relation between the depth index and its physical depth, each index represents a 0.5 mm thickness. Using Equation 5.1, we can derive the $\mu_e \tau_e$ for the crystal is $0.0061 cm^2/V$. After applying the voxel-based electron trapping and material non-uniformity corrections, the Cs-137 spectrum for the whole detector is shown in Figure 5.17. The energy resolution for the 662 keV photopeak is improved to 1.7%. The unusually high counts below 400 ADC channels is due to two reasons. First, low energy scatter-

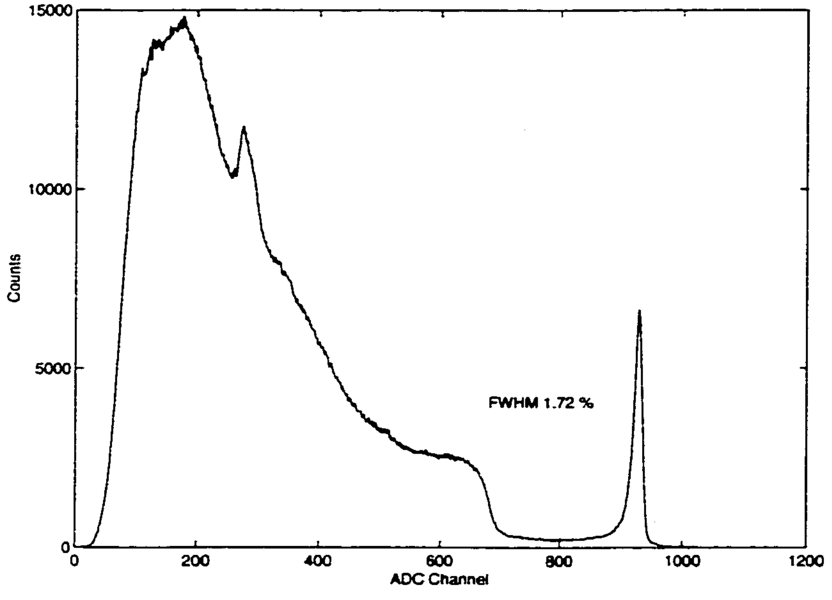

Figure 5.17: Cs-137 spectrum for the whole volume of the first detector.

ing photons from the surrounding material, including the instrument box and PVC support for the detector. Second, due to the high probability of charge sharing, the high energy gamma rays have a much lower single pixel efficiency than normal detectors. This phenomenon will be discussed further later. A Monte Carlo simulation in GEANT3 [Gea3] that modeled the real detector environment and considering the charge sharing effects yielded a similar spectrum for the detector.

Table 5.1 is the photoelectric coefficients for $Cd_{0.9}Zn_{0.1}Te$ calculated from software PHOTOCOEF [Pho]. Based on these photoelectric coefficients, the photopeak area distribution along a 1 cm thick CdZnTe for 59.5 keV, 122 keV and 662 keV gamma rays is shown in Figure 5.18. For the Am-241 59.5 keV gamma rays, the photoelectric effect is the dominant interaction. Due to the high photoelectric coefficient in CdZnTe, most interactions occur within 0.1 cm from the radiation entrance

Energy (keV)	Photoelectric Coef (cm^{-1})
59.5	3.5636E+1
122	4.7499E+0
662	4.8157E-2

Table 5.1: Photoelectric Coefficients for $Cd_{0.9}Zn_{0.1}Te$.

surface. Figure 5.19 and Figure 5.20 are the spectra for Am-241 irradiated from the anode and cathode sides respectively. It is clear from these plots that most interactions occur very close to their incident surface. This confirms our depth sensing by C/A ratio and directly verifies our normalization of the C/A ratio. After applying the same voxel-based correction as that for Cs-137 spectrum, the spectrum for the whole detector irradiated from cathode side is shown in Figure 5.21. The FWHM of the 59.5 keV peak is about 6.1 keV.

The Co-57 spectrum for the whole detector irradiated from the cathode side is shown in Figure 5.22. The FWHM for the 122 keV peak is about 6.7 keV.

5.4.3 Material Non-uniformity

Figure 5.23 is the distribution of the energy resolution FWHM for 662 keV photopeak for the first detector. It is clear from Figure 5.23 that the energy resolution is not uniform across the detector, ranging from 8 keV in some central pixels up to 30 keV for some bad pixels. Most of the peripheral pixels have worse energy resolution than the central pixels. As a result, if we just include the spectrum from the 9 × 9 central pixels, the energy resolutions improve to 5.41 keV, 6.07 keV and 9.3 keV for 59.5 keV, 122 keV and 662 keV gamma rays respectively. As shown in Figure 5.11, the electronic noise for all working VA1 channels have similar values around 3 keV.

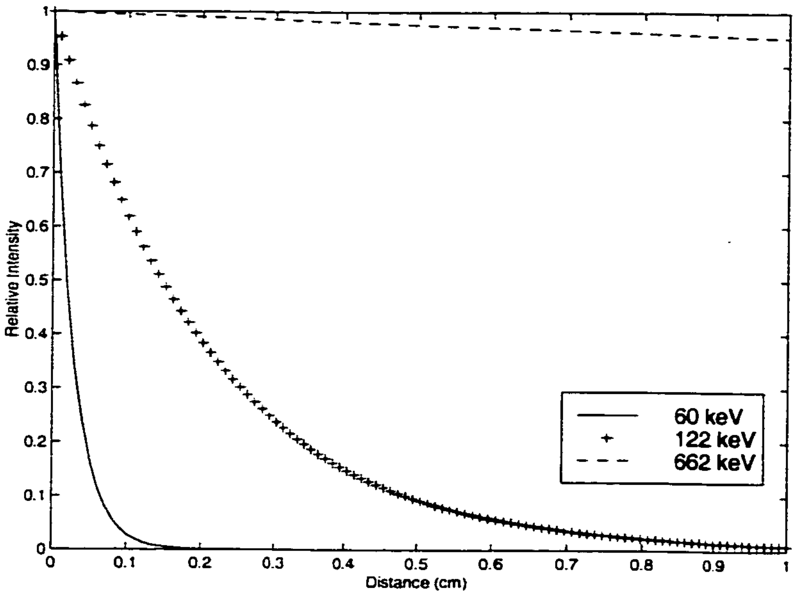

Figure 5.18: Photopeak efficiency distribution for CdZnTe.

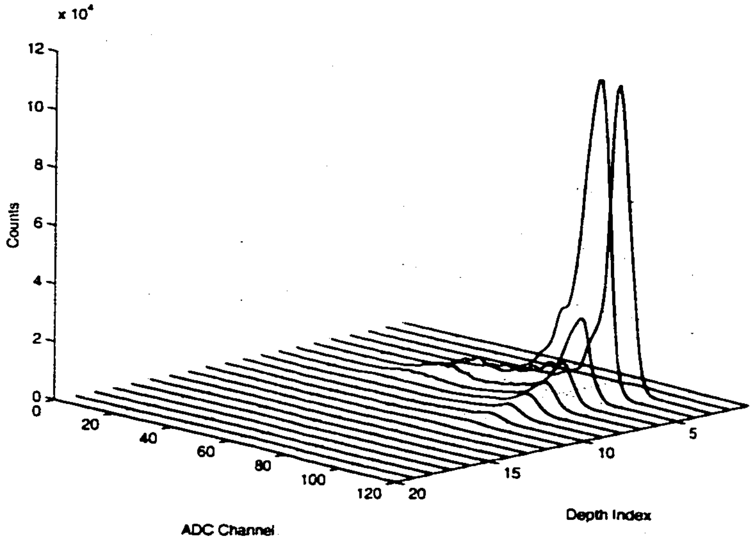

Figure 5.19: Am-241 spectrum along depth index when irradiated from the anode side.

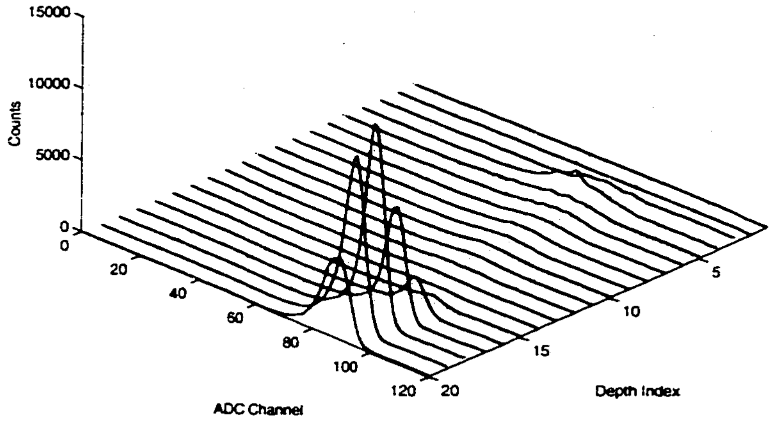

Figure 5.20: Am-241 spectrum along depth index when irradiated from the cathode side.

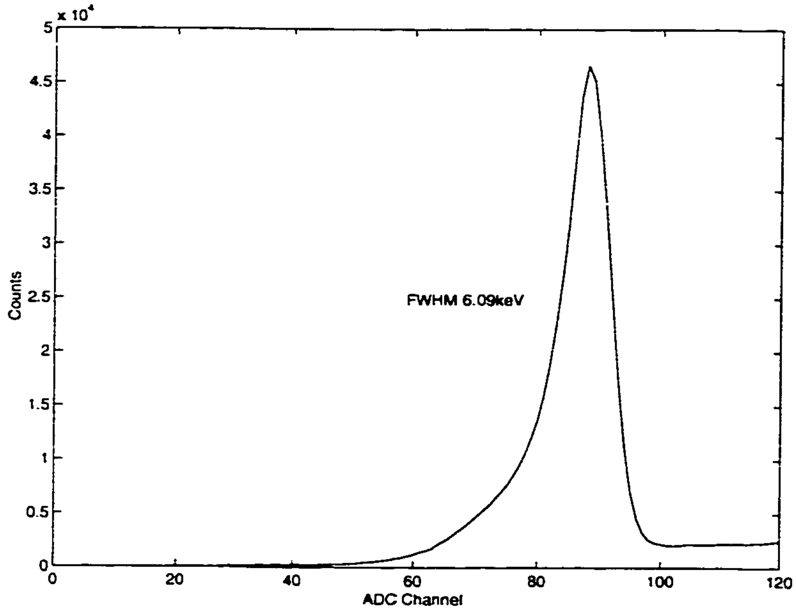

Figure 5.21: Am-241 spectrum for the whole volume of the first detector.

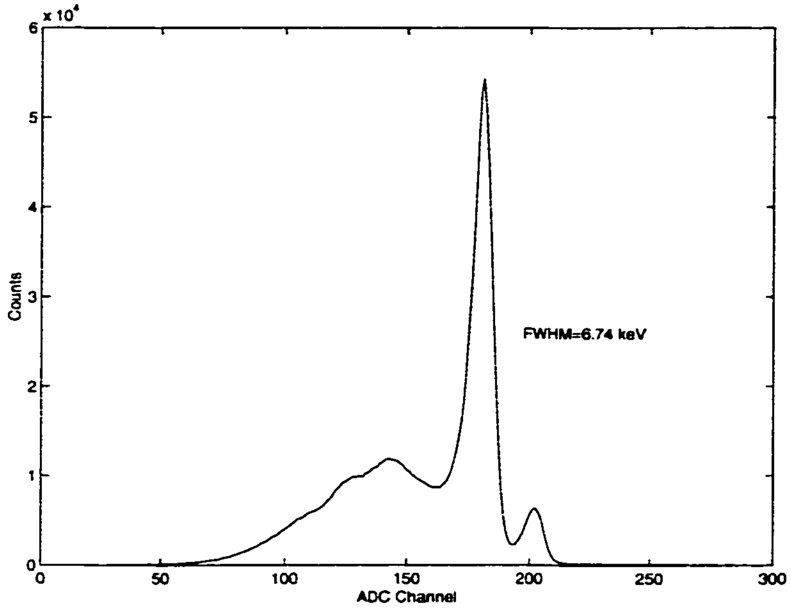

Figure 5.22: Co-57 spectrum for the whole volume of the first detector.

This non-uniform energy resolution is solely due to the material non-uniformity or non-uniform charge collection. Since there is around a 1 mm gap between the anode pixel pattern and the crystal edge, the electrons created under the peripheral pixels need to drift a longer distance to be collected by anode pixels, especially for the four corner pixels. This may explain the wide FWHM for most periphery pixels. But as shown in Figure 5.23, some peripheral pixels do have as good energy resolution as the good central pixels, especially the corner pixel (11,11). Therefore, the non-uniform resolution must be mainly due to the crystal material non-uniformity. As shown in Figure 5.24, the photopeak efficiency for 662 keV gamma rays is also quite different across the detector. According to the anode array geometry, the effective areas are 0.49 mm^2, 1.05 mm^2 and 2.25 mm^2 for central pixels, pixels along the crystal edge, and corner pixels respectively. But the efficiency ratio in Figure 5.24 does not reflect

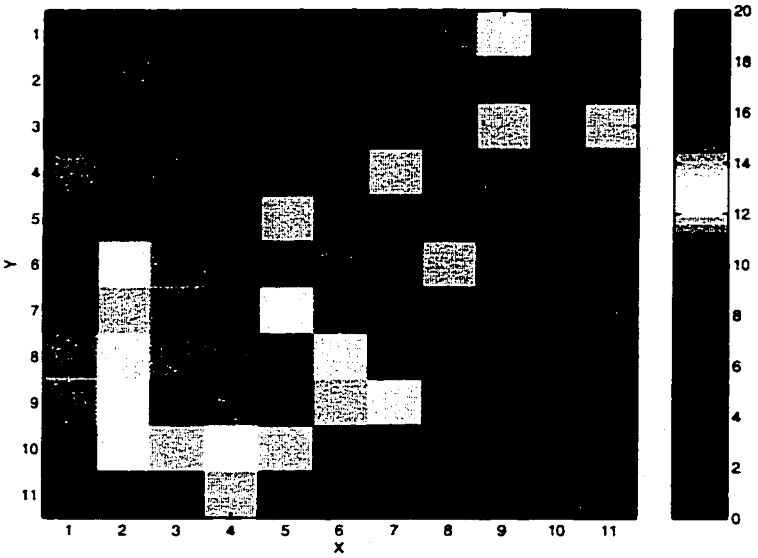

Figure 5.23: 662 keV photopeak energy resolution FWHM(keV) of the first detector.

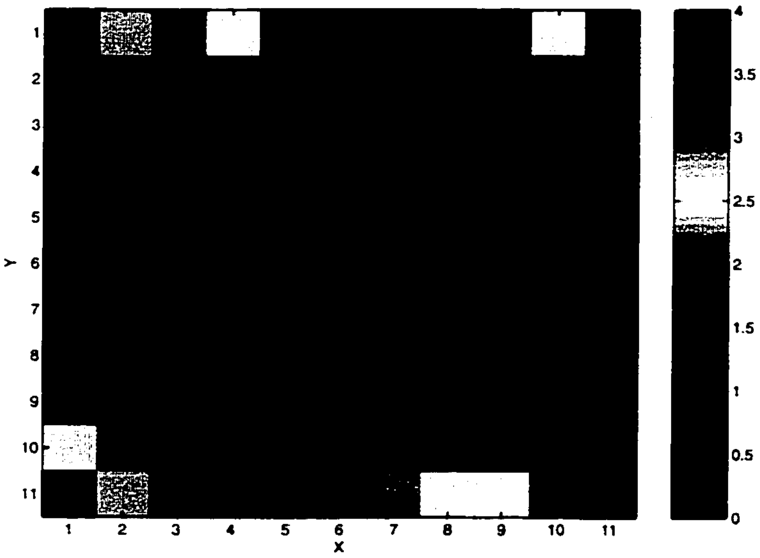

Figure 5.24: 662 keV photopeak area distribution of the first detector (normalized by the photopeak area of the center pixel).

these effective volume ratios. Even the efficiency for the central pixels are quite different. This efficiency non-uniformity can only be due to the material non-uniformity. As shown in Figure 5.18, the photoelectric interaction probability along the 1 cm thick CdZnTe is a slowly varying linear distribution. For those interactions near the cathode side, the electrons have to drift a longer time to the anode pixels. Due to the electron diffusion, the charge sharing probability will be larger for interactions near the cathode side. The multiple pixel rejection probability for interactions near the cathode will be higher. Considering this effect, the efficiency should have a near uniform distribution along the detector thickness. As was previously identified for this crystal, the photopeak efficiency is quite different than the above predictions for most pixels [He00].

As shown in Figure 5.25, there are four types of photopeak area distributions along the depth index. Among the 114 properly working pixels, only 25 pixels belong to group A (near uniform distribution), 54 pixels belong to group B (photopeak efficiency dramatically decrease from the anode to the cathode side), 25 pixels belong to group C (only half of the depth indices close to the anode side have photopeaks), 10 pixels belong to group D (low efficiency in the middle) and one pixel (#16) does not have a photopeak for all depths. It is clear in Figure 5.25 there is a significant photopeak efficiency loss for those pixels belonging to the last three groups. There are three possible reasons why there is a significant efficiency loss for these pixels:

- 1. Due to material defects, the absorption efficiency is different through the detector thickness.

- 2. Due to crystal defects such as grain boundaries, a significant fraction of electrons have been trapped. The anode pixel signal is smaller than the normal

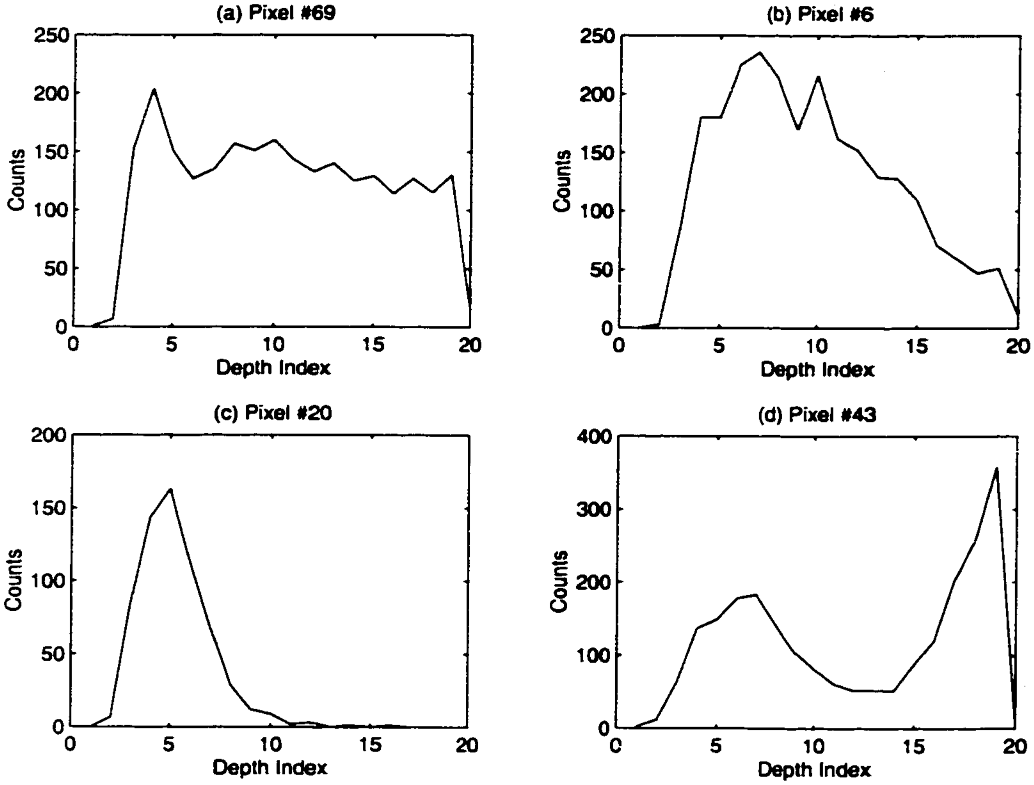

Figure 5.25: Four representative types of photopeak area distribution along the depth index for the first detector.

signal amplitude and can not be recorded in the photopeak window.

- 3. Due to the non-uniform charge sharing, the multi-pixel rejection probability is different along the detector thickness.

Figure 5.26 is the Cs-137 662 keV spectra for pixel 20 at different depth indices. From depth index 10 to 20, there are not only no photopeaks, but also no smaller amplitude events between the Compton edge and the normal photopeak position. This suggests the lost photopeak is not due to the second reason. When irradiated from the cathode side with Co-57 source, the spectra for the same pixel are shown

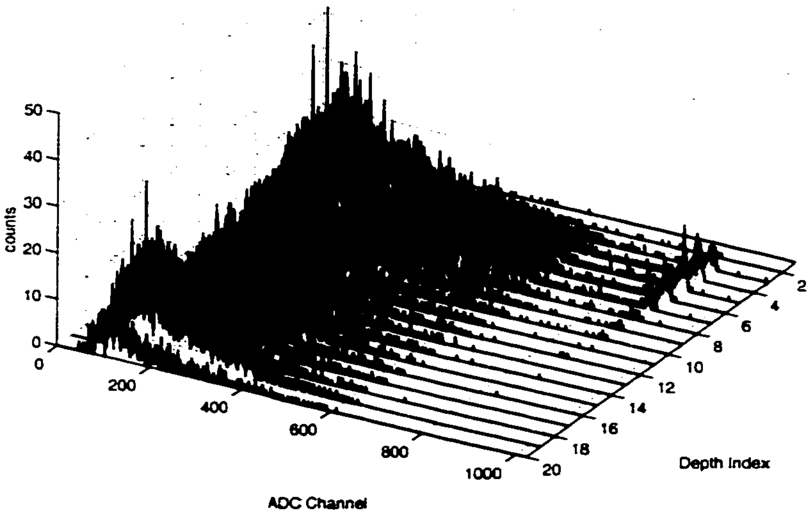

Figure 5.26: Cs-137 spectrum for pixel #20 of the first detector.

in Figure 5.27. The correct count rate along the depth indices and the good energy resolution suggest neither the absorption is low near the cathode nor the electrons experience any severe trapping along their way to the anode pixel. Other pixels in group C also have good spectra near the cathode for Co-57 gamma rays. This energy dependent behavior can only be explained by the third reason. According to the Monte Carlo simulation, the average transportation distance for 662 keV photoelectrons in CdZnTe is around 200 μm, and the diffusion length is 50 μm [Du98]. So for a 700 $\mu m \times$ 700 μm pixel, only those photoelectric events occurring in the central 200 × 200 μm^2 region can be recorded as single pixel events, that is only about 8%. If, due to some crystal defects or channel effects, the photoelectrons have an even longer transport distance, the charge sharing probability will be even larger and strongly depends on photoelectron transport and electron carrier diffusion. Any

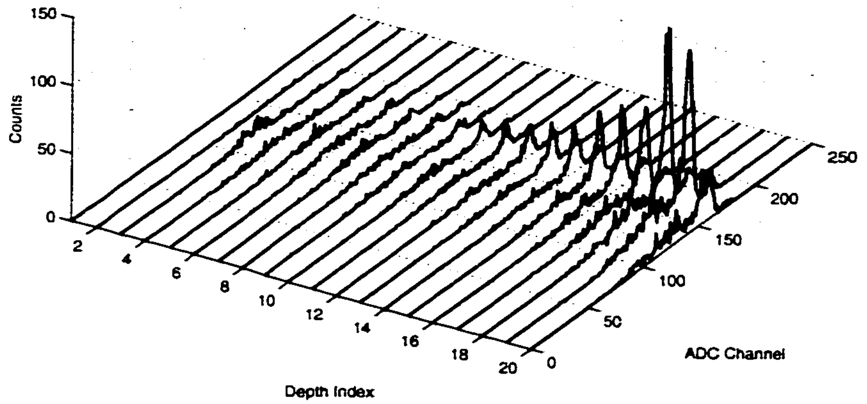

Figure 5.27: Cs-57 spectrum for pixel #20 of the first detector when irradiated from the cathode side.

non-uniformity for these effects will affect the single pixel photopeak efficiency. On the other hand, the average transport distance for 122 keV photoelectrons is only around 20 μm. Using the same diffusion length, 80% events can be recorded as single pixel events. That is why there is a good 122 keV photopeak for pixel 20 while there is no 662 keV photopeak near the cathode side.

In order to verify the above explanations, the Cs-137 spectrum is measured with all conditions remaining the same except for an increase in the single pixel event select threshold from 10 ADC channels (6 keV) to 80 ADC Channels (55 keV). As shown in Figure 5.28, all depth indices for pixel 20 have near uniform photopeak counts. The similar situation occurs with many other pixels in group C. Under the new high threshold, all working pixels have photopeaks for all depth indices. The number of pixels in normal group A increased to 79. As shown in Figure 5.29, not

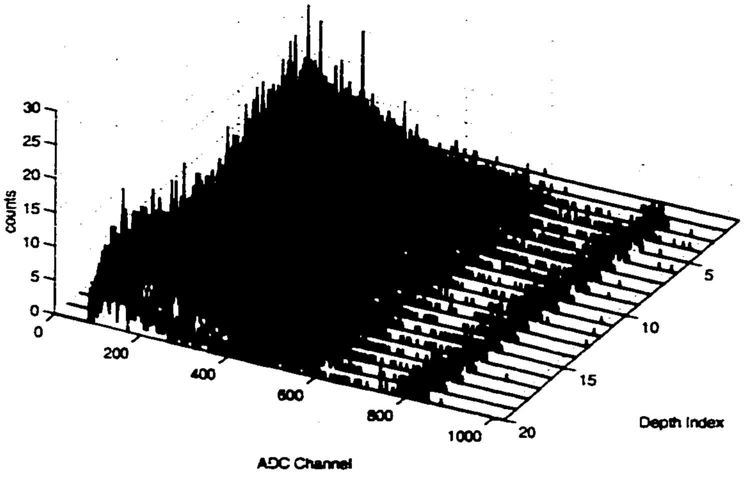

Figure 5.28: Cs-137 spectrum for pixel # 20 of the first detector with increased select threshold.

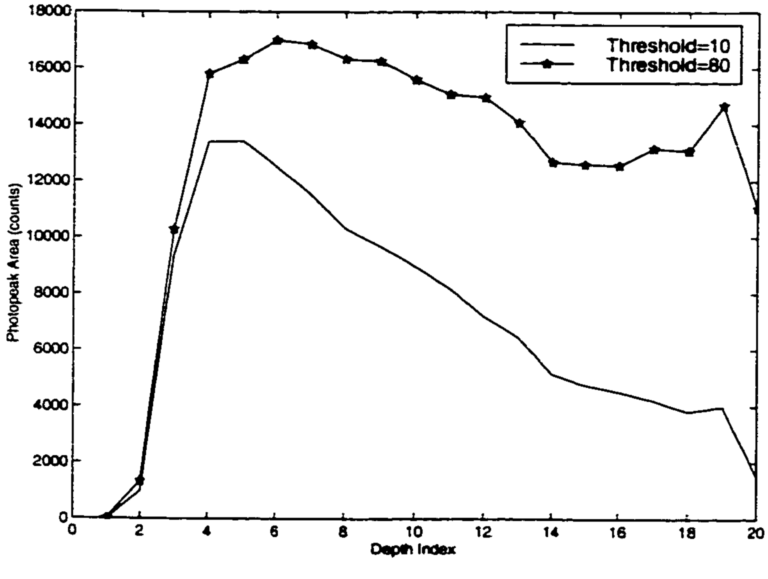

Figure 5.29: The photopeak area distribution for the first detector under two select thresholds.

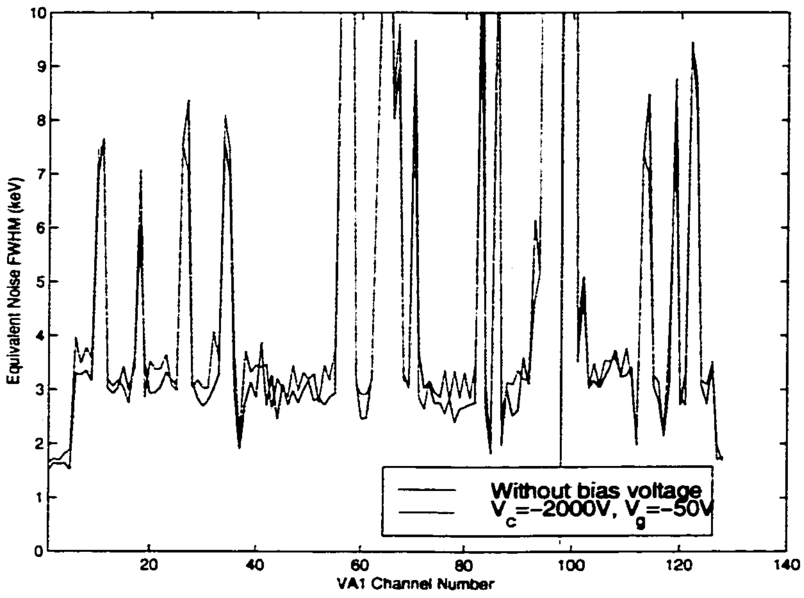

Figure 5.30: The baseline noise for the second detector.

only is the overall efficiency much high under the high threshold, but the distribution over the depth indices becomes more uniform. As the single pixel select threshold increases, the event will not be rejected as a multiple pixel event unless the charge shared by other pixels is above the threshold. That is why the photopeak efficiency increased in Figure 5.29. Therefore, we can conclude that the abnormal photopeak effiency is mainly due to the strong, non-uniform charge sharing.

5.5 The Second Detector Characterization

5.5.1 Electronic Noise and Test Pulse Response

Figure 5.30 is the equivalent noise FWHM of the baseline fluctuation for the second detector before and after applying the bias voltages. Similar to the first detector, the baseline fluctuation does not have any significant changes in different bias conditions. The first 5 and last 2 open VA1 channels have a noise level around

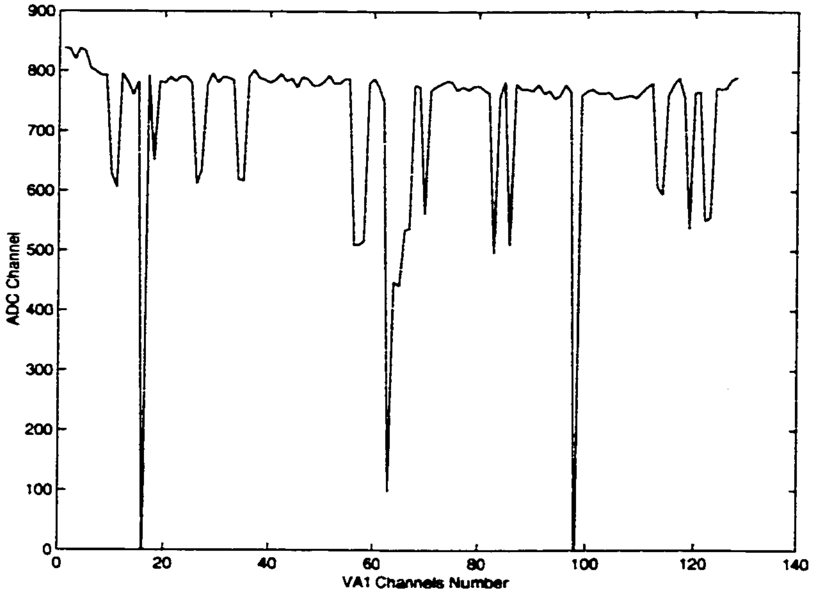

Figure 5.31: Test pulse amplitude for the second detector (Test level = -4.0 V).

1.5 keV. About two thirds of the VA1 channels have the noise levels around 3 keV, but about one third of the channels have abnormally high noise. Figure 5.31 is the VA1 output amplitude when the test level = -4.0 V, cathode bias V_c =-2000 V and anode grid bias V_g =-50 V. Figure 5.32 is the VA1 output amplitude fluctuations. The test results under different bias conditions or different test levels also have similar fluctuations. It is clear in Figure 5.31 that those VA1 channels that have a high noise do not have a normal response to the test pulse. Their output amplitude is smaller than that of the normal channels. The gamma-ray spectra for these channels look also unreasonable, so these pixels are excluded from the data acquisition. Only 83 pixels have normal response.

Similar to the situation for the first detector, in Figure 5.31, the VA1 test pulse amplitudes for those normal channels have non-uniform gains. So the anode pixel

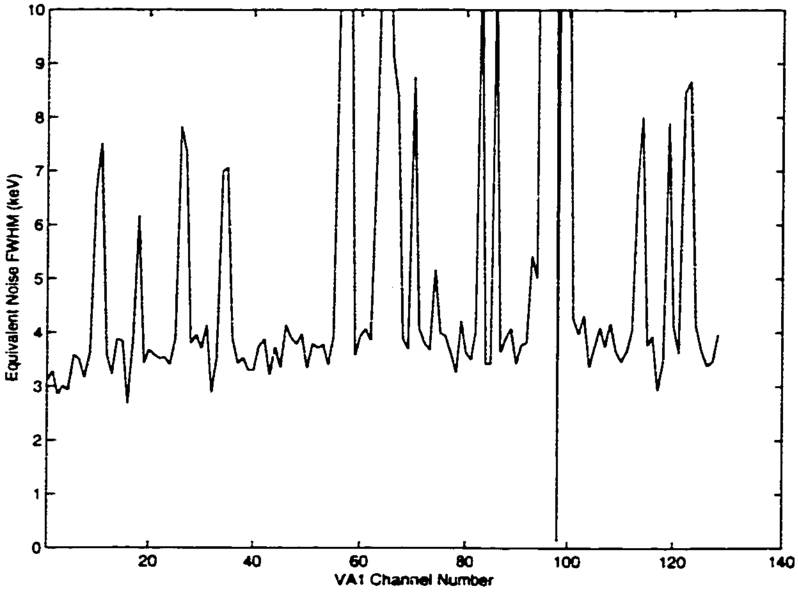

Figure 5.32: Test pulse noise for the second detector.

signal amplitude is corrected for the non-uniform gain based on the normalization factor from the test pulse amplitude at test level -4.1V.

5.5.2 Energy Spectra

All the following spectra were taken with V_c = -2000V and V_g = -50V, and the gamma ray irradiated from the cathode side unless otherwise specified. Figure 5.33 is the 662 keV photopeak centroid distribution for pixel 15, from depth index 4 to 20, the photopeak centroid decreases from 998 ADC channels to 945 channels. So the electron trapping from the cathode to near the anode is around 5.3%. From Equation 5.1, the electrons $\mu_e \tau_e = 0.0078$ cm$^2/V$, which is slightly better than that for the first detector.

After applying the voxel-based electron trapping and material non-uniformity corrections, the Cs-137 spectrum for the second detector is shown in Figure 5.34.

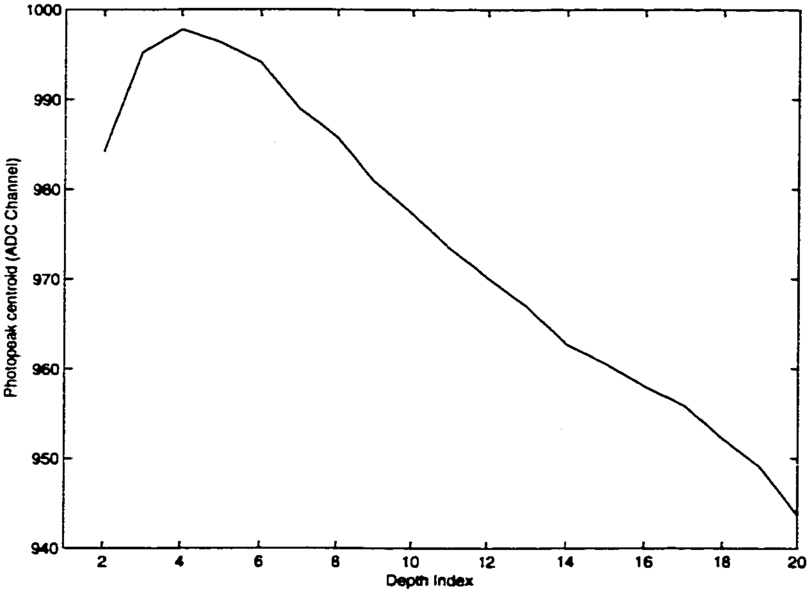

Figure 5.33: 662 keV photopeak centroid distribution for pixel #15 of the second detector.

The energy resolution for the 662 keV photopeak is 1.98%. Figure 5.35 is the Am-241 spectrum with a FWHM of around 5.56 keV. Figure 5.36 is Co-57 spectrum for the whole detector. The FWHM for the 122 keV peak is about 6.7 keV. Therefore, both detectors have similar energy resolutions for 662 keV, 122 keV and 59.5 keV gamma rays.

5.5.3 Material Non-uniformity

Figure 5.37 is the 662 keV photopeak FWHM distribution for the second detector. Again, most of the periphery pixels have much worse resolution than the central pixels. As a result, if we only combined the spectra for the central 9 × 9 pixels, the FWHM would improve to 5 keV, 6.13 keV and 10 keV for 59.5 keV, 122 keV and 662 keV gamma rays respectively. Figure 5.38 is the 662 keV photopeak area distribution. Even for the pixels in the central region, the energy resolution and the

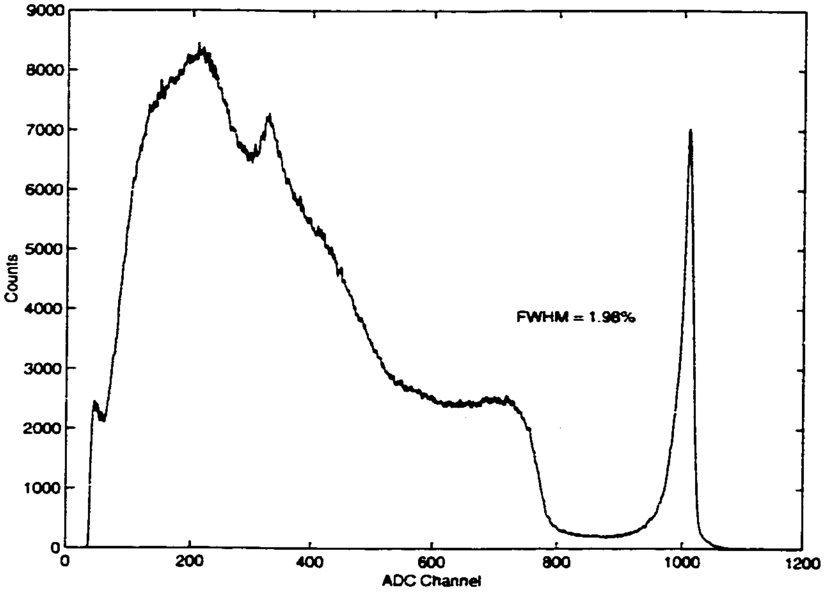

Figure 5.34: Cs-137 spectrum for the whole volume of the second detector.

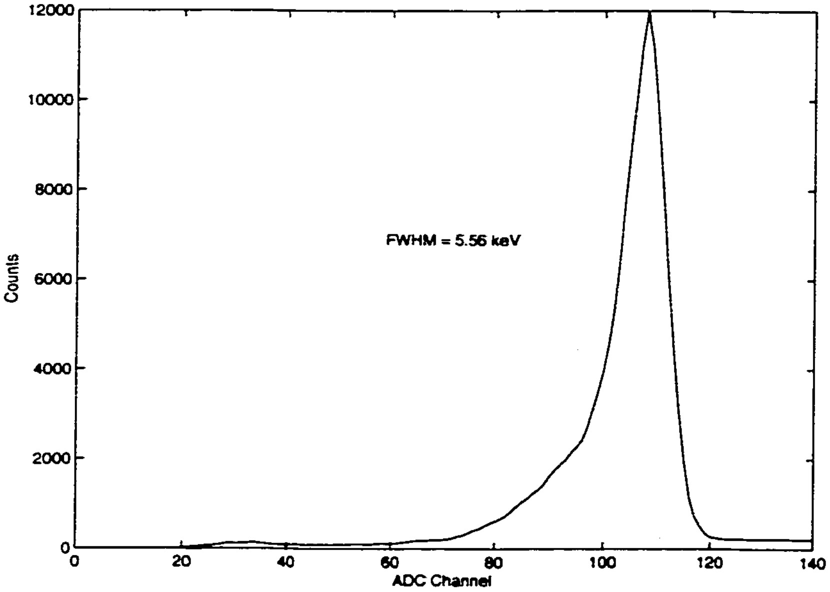

Figure 5.35: Am-241 spectrum for the whole volume of the second detector.

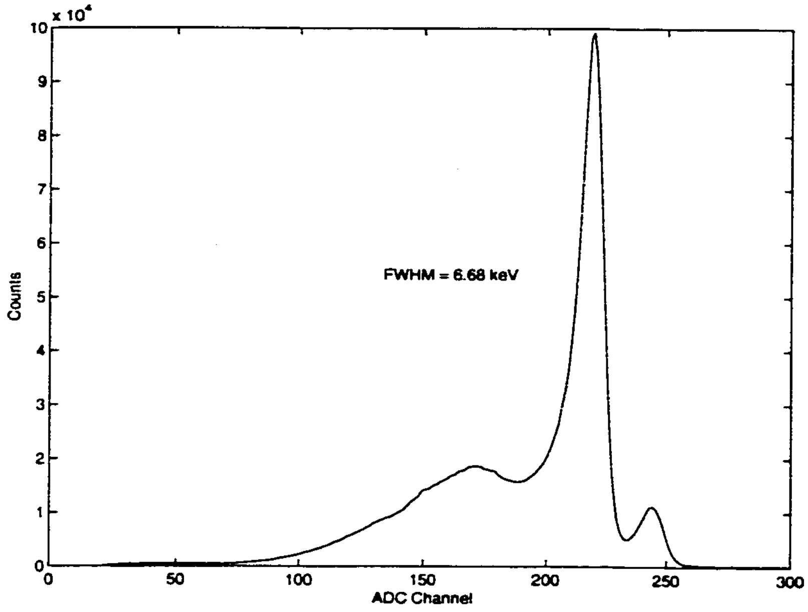

Figure 5.36: Co-57 spectrum for the whole volume of the second detector.

efficiency are not uniform. But compared with the distributions for the first detector in Figure 5.23 and Figure 5.24, the second detector has a more uniform response. If we classified the working pixels in the same fashion as for the first detector, only those pixels along the right edge of the crystal belong to group C. Other pixels have group A type normal photopeak area distributions along the depth indices. Therefore, the crystal for the second detector has much more uniform charge sharing properties than that for the first detector.

5.6 Detectors Energy Resolution Analysis

As presented in the last two sections, the electronic noise for both detectors is only around 3 keV. However the energy resolution is only around 5 keV, 6 keV and 10 keV for 59.5 keV, 122 keV and 662 keV respectively, even for the central pixels. Table 5.2 is the energy resolution for some good pixels in the first detector under

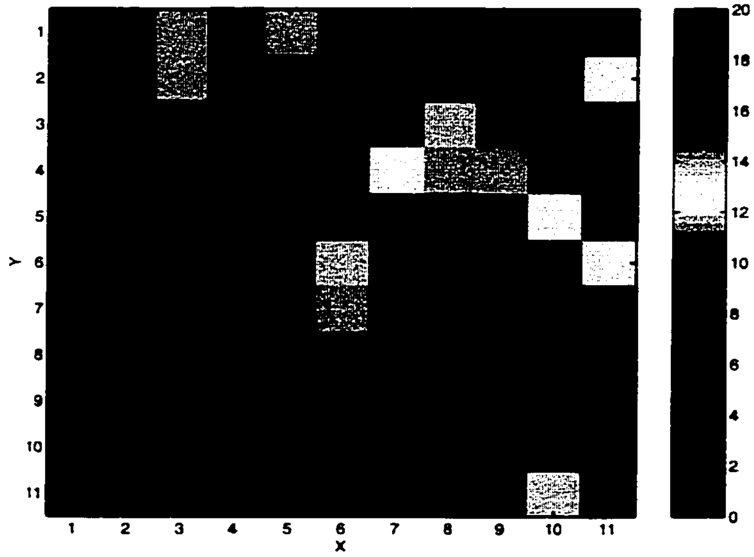

Figure 5.37: 662 keV photopeak energy resolution FWHM(keV) of the second detector.

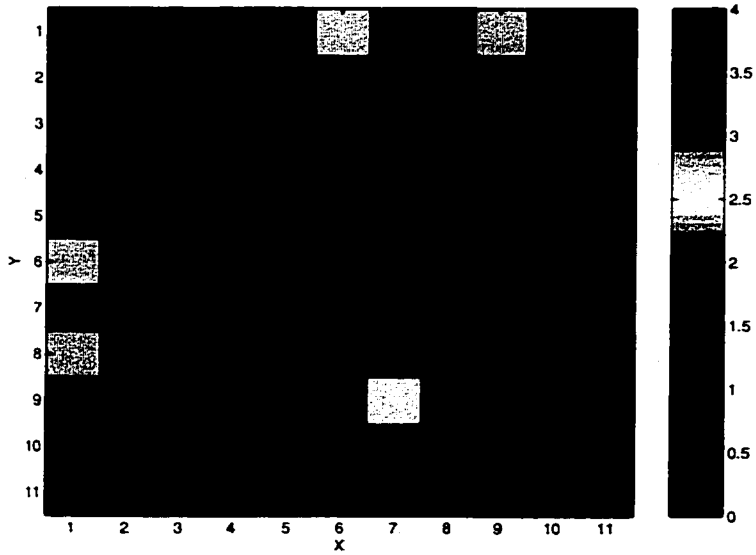

Figure 5.38: 662 keV photopeak area distribution for the second detector (normalized by the photopeak area of the center pixel).

Source	pixel # 22	pixel #27	pixel #28	pixel #54	pixel 55
baseline noise	2.9	2.2	2.3	2.8	2.5
test pulse noise	4.6	4.5	4.4	4.2	4.0
59.5 keV (anode)	5.5	5.5	6.2	6.2	6.2
59.5 keV (cathode)	5.3	6.0	6.0	5.2	6.0
122 keV (anode)	5.4	5.4	4.7	5.4	5.4
122 keV (cathode)	5.4	5.4	5.4	5.4	5.4
662 keV (anode)	8.1	8.1	8.1	8.8	8.1

Table 5.2: Energy resolution FWHM (keV) for some good pixels of the first detector.

various gamma-ray energies and radiation conditions. For these pixels, the baseline fluctuation is less than 3 keV. So the electronic noise should be around this value. As pointed out earlier, the test pulse noise is the quadratic summation of the true electronic noise and the noise for the test pulse itself. As shown in Table 5.2, the measured test pulse noise is only between 4.0 to 4.6 keV for these pixels, so the electronic noise of the VA1 channels for these pixels can not be larger than these test pulse noises. As a very conservative estimation, we can assume the electronic noise for these pixels is 4.0 keV. The relative energy resolution due to charge carriers number fluctuation is given by [Kno00]:

$$R_{statistical} = 2.35\sqrt{\frac{F}{N}}, \tag{5.2}$$

where F is the Fano factor, $N = E/\varepsilon$ is the charge carrier number generated by incident radiation, and ε is the ionization energy. Considering the electron trapping effects, not all electrons can be collected by the anode pixels. If we let η represent the charge collecting efficiency, the statistical limit for the energy resolution FWHM is

$$(FWHM)_{statistical} = R_{statistical}E = 2.35\sqrt{\frac{FE\varepsilon}{\eta}}. \tag{5.3}$$

The overall energy resolution is

$$(FWHM)^2_{overall} = (FWHM)^2_{noise} + (FWHM)^2_{statistical}. \tag{5.4}$$

As shown in the last section, the electron trapping from the cathode to the anode side is 5%. So $\eta = 0.95$ and $\eta = 1.0$ is used for low energy gamma rays incident from the cathode and the anode side respectively. The estimated energy resolution is listed in Table 5.3 for F=0.1 and F=1. Comparing with the measured results in Table 5.2, the measured energy resolution is worse than the estimation, even with Fano factor equal to 1. Therefore, there must exist other energy resolution degradation factors. For our pixellated detectors, material non-uniformity, trigger signal timing variation, charge sharing, and incomplete electron collection by the anode pixels can all contribute to additional energy resolution degradation.

Fano factor	59.5(anode)	59.5(cathode)	122(anode)	122(cathode)	662
0.1	4.02	4.02	4.04	4.04	4.22
1.0	4.20	4.21	4.40	4.42	5.86

Table 5.3: A very conservative estimation of the detector energy resolution FWHM (keV) (assume electronic noise =4.0 keV, ionization energy = 5.0 eV)

5.6.1 Material Non-uniformity

With the three-dimensional position sensing capability, the detector volume is virtually divided into $11 \times 11 \times 20$ voxels. For the central pixels, the effective volume for each voxel is only 0.7 mm × 0.7 mm × 0.5 mm. With this position sensing capability, the voxel by voxel material non-uniformity and electron trapping are corrected. Only the microscopic material non-uniformity within this small voxel affects the energy resolution for each pixel. Due to the short transportation distance of photoelectrons from low energy gamma rays, the microscopic material non-uniformity will affect the low energy gamma-ray energy resolution, such as in 59.5 keV or 122 keV. But for 662 keV, due to the large electron transportation distance, the microscopic material non-uniformity will have little effect on the energy resolution. Furthermore, for interactions near the cathode side, the electrons have to drift across the whole detector thickness to the anode pixels to be collected. The effect of the non-uniform trapping will be the most severe for these electrons. Thus the energy spectrum from interactions near the cathode side should have worse resolution than the spectrum for interactions near the anode side. However in Table 5.2, the Co-57 122 keV photopeak has the same energy resolution when irradiated from the cathode and the anode side. Thus the material non-uniformity is not a dominant factor, at least for these good pixels.

5.6.2 Trigger Signal Timing variation

As shown in Figure 5.4, the delay time between the trigger and the sample/hold signal is critical for the VA1 to capture the correct output peak amplitudes. Any timing variation for the trigger signal will degrade the detector energy resolution. Figure 5.39 shows some measured delay time between the anode grid trigger signal and the VA1 shaping amplifier output peak. For this set of measurements, the average delay time is 1 μs, so we set the delay between the trigger and the sample/hold signal to 1 μs in our data acquisitions. The standard deviation of these delays is 70.5 ns. If we assume the delay time is a Gaussian distribution, the FWHM of the

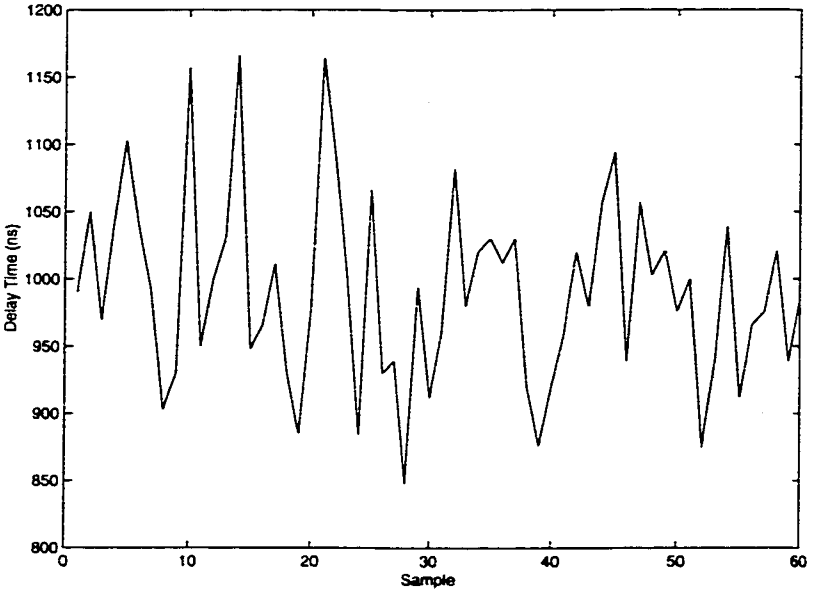

Figure 5.39: Measured delay time between the trigger signal and the VA1 shaping amplifier output peaking time.

delay distribution is $2.35 \times 70.5ns = 165.7ns$. As pointed out in Section 5.2, the additional time walk due to the timer on the DAQ board is 50 ns. Therefore the combined timing uncertainty FWHM is $\sqrt{165.7^2 + 50^2}ns = 173ns$. The blue line in Figure 5.40 is the measured waveform of the VA1 shaping amplifier output whereas the red line is the CR-RC shaping output waveform [Kno00]

$$E_{CR-RC}(t) = \frac{E_{in}\tau_{cr}}{\tau_{cr} - \tau_{rc}}(e^{-t/\tau_{cr}} - e^{-t/\tau_{RC}}), \tag{5.5}$$

with $\tau_{CR} = 600$ ns and $\tau_{RC} = 4.8$ μs. Thus, the VA1 shaping output can be matched very well by a CR-RC shaping output. E_{CR-RC} has the normalized amplitude of 1 at t=1428 ns. $E_{CR-RC}(1428 - 88) = 0.9985$ and $E_{CR-RC}(1428 + 88) = 0.9988$ corresponding to 173 ns FWHM around the peaking time. Therefore, maximum energy uncertainty due to the trigger signal timing uncertainty is around 0.15%. Comparing with the large difference between the measured energy resolution and

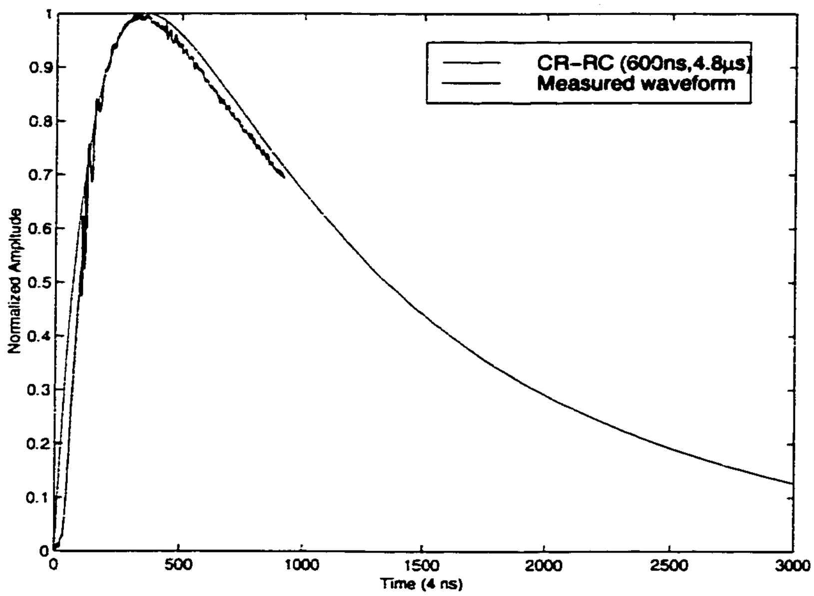

Figure 5.40: Waveform of the VA1 shaping amplifier output signal.

our conservative estimation, it is clear that timing effects can be ignored.

5.6.3 Charge Sharing Effects

As was estimated in Section 5.4.3, for 662 keV photoelectric absorption events near the cathode, 91% will have charge sharing between neighboring pixels. The charge sharing effect has a strong influence on the photopeak efficiency. If the charge sharing occurs, only when the energy shared by its neighboring pixels is larger than the single pixel selection threshold will that event be registered as a multiple pixel event and be rejected. Thus, if the energy shared is less than the threshold, this event will still be incorrectly registered as a single pixel event, but with a smaller energy. For 662 keV photoelectrons, depending on the interaction lateral position, the depth position, and the electron cloud lateral extension, the charge sharing fraction will be different. Charge sharing can contribute significantly to the photopeak broadening.

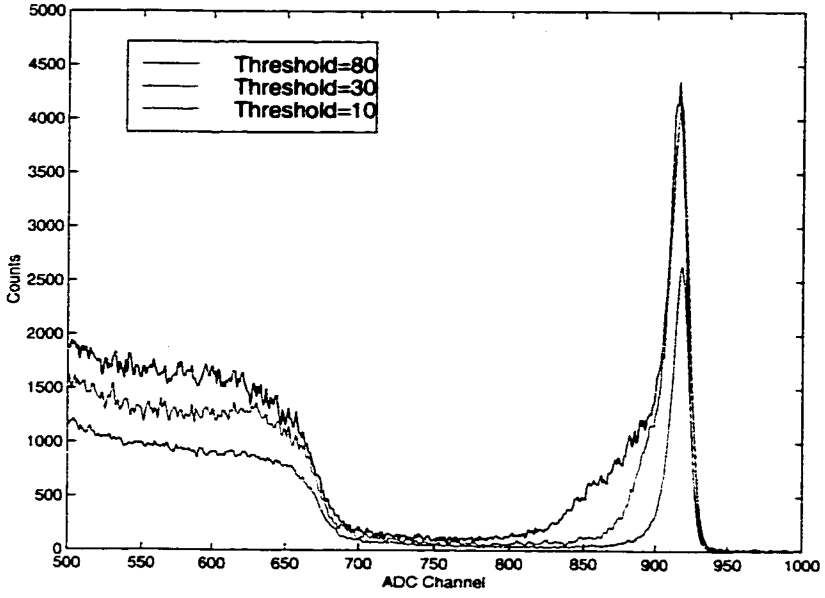

Figure 5.41: Cs-137 spectrum at three single pixel selection thresholds for the first detector.

Figure 5.41 is the measured single pixel events spectrum for the Cs-137 662 keV gamma rays at three select thresholds: 10 ADC channels (6 keV), 30 ADC channels (20 keV), and 80 ADC Channels (55 keV). When the threshold increases, more charge sharing events will be registered as single pixel events. Thus, the low energy tail for the photopeak becomes more obvious and the energy resolution FWHM increases from 9.27 keV to 11.4 keV and 11.9 keV respectively. For low energy gamma rays, such as 122 keV, the photoelectron travel distance is short. If the interaction occurs near the anode side, the electrons will be collected by anode pixels very quickly and the diffusion can also be neglected. The charge sharing probability of such interactions is very small, so charge sharing effect will have a small effect on the energy resolution. Figure 5.42 is the measured Co-57 single pixel spectrum when the source was irradiated from the anode side. As shown in Figure 5.42, the photopeaks

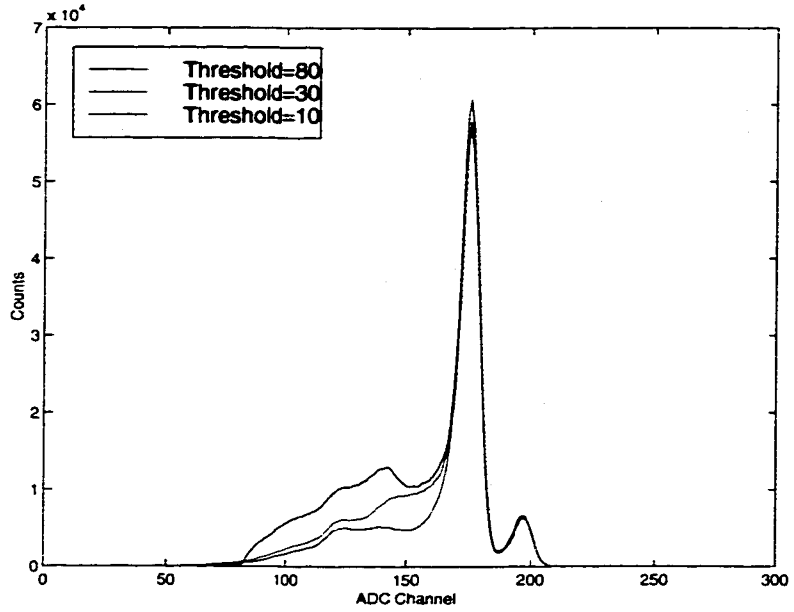

Figure 5.42: Co-57 spectrum at three single pixel selection thresholds for the first detector when irradiated from the anode side.

themselves do not have any significant change with different thresholds. The FWHM of the photopeak remains the same. The only change in Figure 5.42 is the increased counts for the escape peak. Following the photoelectric interaction, if the x-ray travels to other pixels and then deposits its energy there, this event is also rejected as a multiple pixel event if the threshold is low. However with a high threshold, more escape events are recorded.

From the above analysis and experimental results, we can conclude that charge sharing is indeed a degradation factor to the detector energy resolution when the charge sharing probability is high. Due to the limitation of the current readout electronics, we can not measure the correct signal amplitude for multiple interaction events, and have to reject them. The influence of charge sharing on the energy resolution is very severe for 662 keV gamma rays. In future readout electronics, such as the VAS-TAT system, if the ASIC has the self trigger capability and a peak-hold circuit for each channel, then by summing the measured amplitude from multiple channels for multiple pixel events, the charge sharing effect on the energy resolution and the efficiency can be improved. However as long as each channel still has some threshold to trigger its operation, this influence can not be eliminated. Furthermore, by summing multiple pixels' signals together, the electronic noise will increase quadratically. Charge sharing adds another limitation to the energy resolution of pixellated detectors besides the electronic noise and the charge carrier statistics. In order to reduce the charge sharing, the pixel dimensions have to increase. On the other hand, by increasing the pixel size, the small pixel effect becomes less influential, so the contribution due to holes will begin to influence the energy resolution. Therefore, in the design of pixellated detectors, these competing factors need to be considered.

5.6.4 Incomplete Charge Collection

A small -50 V bias voltage is applied to the anode grid to help the electron collection by the anode pixels. Relative to the -2000V bias voltage on the cathode, this -50V bias is small. The operating electric field inside the detector crystal should be ideally uniform for most of the region, then bend towards the anode pixels near the anode surface. In this ideal situation, the anode grid acts like a non-collecting anode for the coplanar grid detector. When the electrons drift towards to the anode, the induced charge on the grid begins to increase. When the electrons move very close to the anode surface and are collected by the anode pixels, the induced charge on the grid quickly drops to zero. Figure 5.43 shows some measured waveforms for the anode grid output. In Figure 5.43 (a), the anode grid signal acts as predicted. However

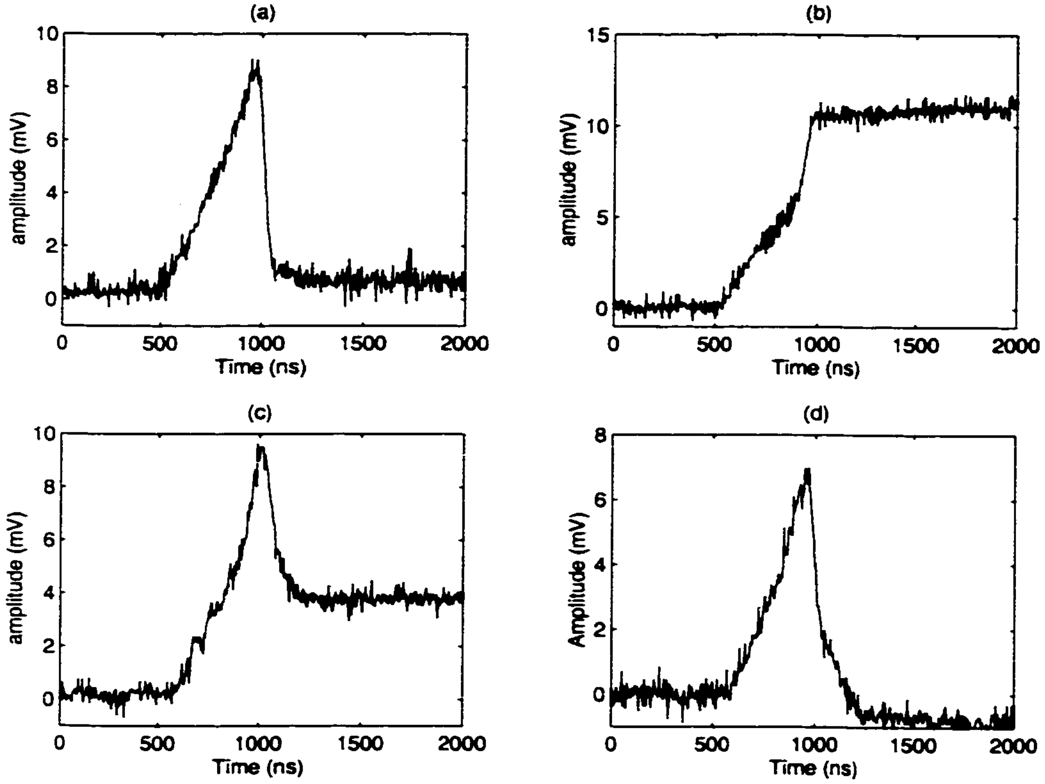

Figure 5.43: Waveforms of the anode grid signals from the first detector.

other waveforms in Figure 5.43 are different from the ideal waveform. In Figure 5.43 (b), the output remains at a high level after increasing from zero. That indicates all the electrons are collected by the anode grid. In Figure 5.43 (c), the grid signal decreases to some middle level from its peak value. That indicates only a fraction of the electrons are collected by the anode pixels. In Figure 5.43 (d), although the grid signal drops to its baseline eventually, the slow slope there suggests the electrons drift very slowly during that time, either due to low electric field or low electron mobility near the anode. This unusual long drift time should lead to more electron trapping.

These three undesirable cases identified in Figure 5.43 lead to incomplete charge collection and therefore degrade the detector energy resolution. As analyzed in the last section, due to the small charge sharing probability, the charge sharing effect has small effect on low energy gamma-ray resolution, especially when the source was irradiated from the anode side. The large energy resolution FWHM in Table 5.43 for 59.5 keV and 122 keV are mainly due to incomplete charge collection since we excluded other factors.

In order to improve the charge collection efficiency, a large bias on the anode grid will be helpful. However increasing the anode grid bias is limited by leakage current constraints. Unless the detector surface processing allows a high enough bias for complete charge collection by the anode pixels, the incomplete charge collection adds another limitation to the energy resolution for the pixellated detectors.

CHAPTER VI

IMAGING DATA ACQUISITION AND ANALYSIS

6.1 Imaging Data Acquisition and Processing

With the 2000V bias between the cathode and the anode, the normal electron drift time from the cathode to the anode is around 500 ns. However due to material non-uniformities inside the crystal, either the electron mobility or the electric field in some region is smaller than the normal value. It was observed that for some events, the signal rise time was larger than the normal 500 ns. Therefore, the coincidence resolution time was set to 1 μs to make sure these events were collected in coincidence mode. As shown in Figure 5.17 and Figure 5.34, the Cs-137 spectra had a much higher count rate in the low energy range due to the increased scattering of gamma rays from the surrounding material. In order to reduce the chance coincidence count rate due to these low energy gamma rays, the anode grid thresholds for both detectors were set as high as possible while allowing the true coincident events from Compton scattering to be collected. During the coincidence imaging data acquisition, the anode pixel number, the anode pixel signal amplitude, and the cathode signal amplitude from each detector are stored in a list mode by the DAQ software. Before the image reconstruction, these raw data are first corrected for non-uniform gains of the VA1 channels. Then, the voxel-based electron trapping and material non-uniformity are corrected. After that, the absolute energy for each event is calculated from each detector's own energy calibration and the 3-D position is calculated based on the pixel position and the C/A ratio. These newly obtained energy and position data are stored to another file in the list mode for image reconstruction.

6.2 Cs-137 Point Source Image

As we estimated in Section 2.3, the field-of-view for the camera is between 20° and 80° scatter angle, which is ±30° around the central scatter angle 50°. A 10 μCi point Cs-137 source (Amersham, S/N AY642) is placed 50° relative to the center axis of the two detectors, right on the front surface of the instrument box of the camera. The distance between the point source to the center of the first detector is 8.45 cm. Due to the symmetric condition for the point source relative to the two detectors, the source does not need to rotate around the center of the field-of-view. Instead, the measured coincidence data are divided into 12 groups with equal counts in each group to simulate the azimuthal sampling between 0° and 360° of the source plane.

6.2.1 Coincident Energy Spectra

The coincident spectra for the two detectors and the summed spectrum are shown in Figure 6.1, Figure 6.2 and Figure 6.3, respectively. The 200 keV peak in Figure 6.1 corresponds to the 50° scattering photons in the first detector. The broadening of the peak is primarily due to the scatter angle spread. Although the scatter angle from the point source to the centers of the two detectors is 50°, the actual scatter angles can range from 35° to 65°. The 460 keV peak for the second detector corresponds to the photoelectric absorption of the scattered photons. The events below this energy are either due to Compton scattering interactions of the scattered photons or the

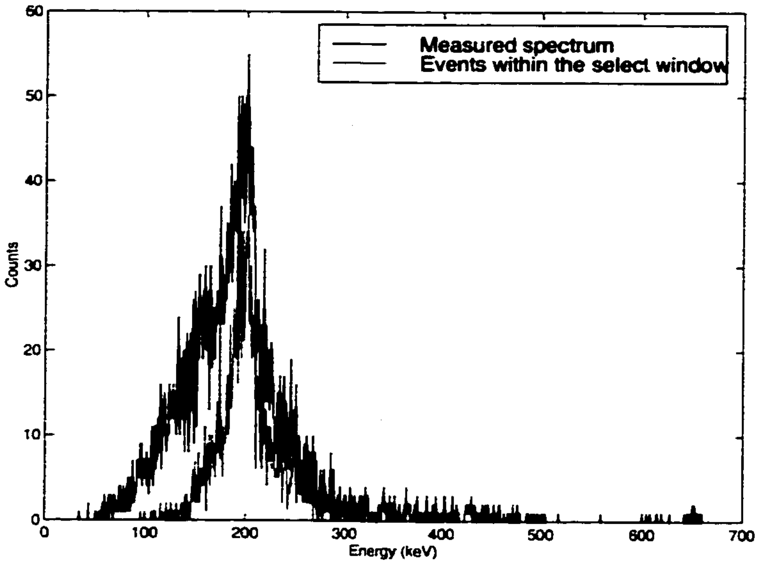

Figure 6.1: Coincident energy spectrum for the first detector with the Cs-137 point source located 50° relative to the centers of the two detectors. The total data collection time is 4.0 × 10^5 seconds.

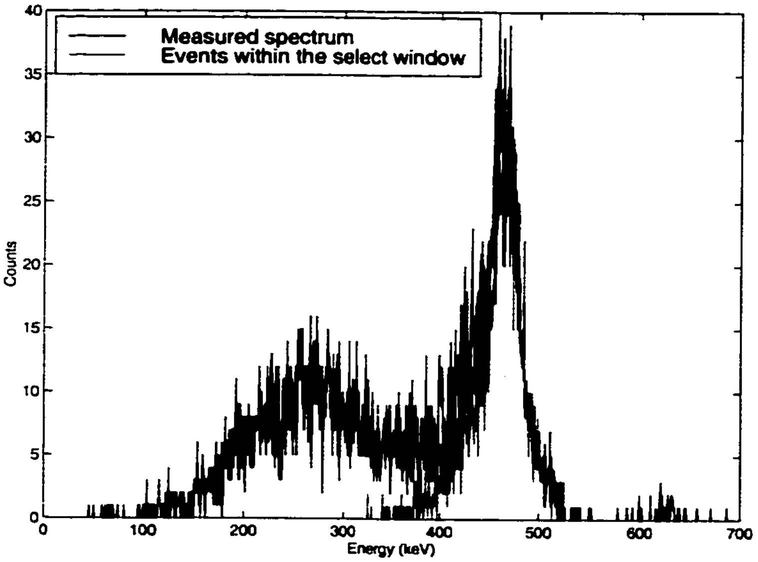

Figure 6.2: Coincident energy spectrum for the second detector with the Cs-137 point source.

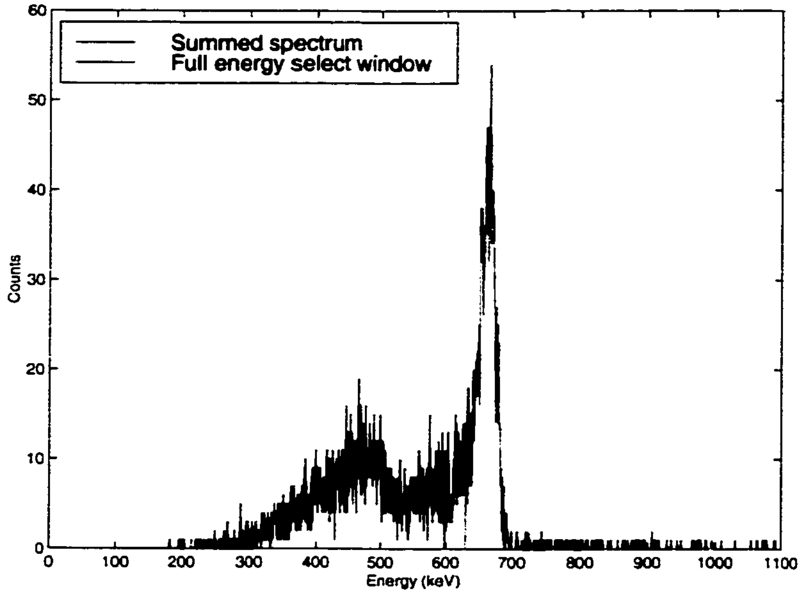

Figure 6.3: Summed energy spectrum for the Cs-137 point source.

accidental coincident events. In the summed spectrum in Figure 6.3, the FWHM for the 662 keV peak is about 21.7 keV. According to the relation between the energy resolution FWHM and the deposited energy for each detector, the FWHM for the first detector around 200 keV is 8.1 keV, and the FWHM for the second detector around 460 keV is 11.4 keV. Then the FWHM for the summed full energy peak should be $\sqrt{8.1^2 + 11.4^2} = 14.0$ keV. The large measured FWHM for the summed spectrum is mainly due to the detector energy calibration error and the gain shift over the long data collection time. These effects will be discussed later. Those events on the right side of the 662 keV peak are chance coincident events. In order to reduce these events, an energy window around the 662 keV peak is applied to the summed spectrum. Only those events whose sum energy is within this window are used for image reconstruction.

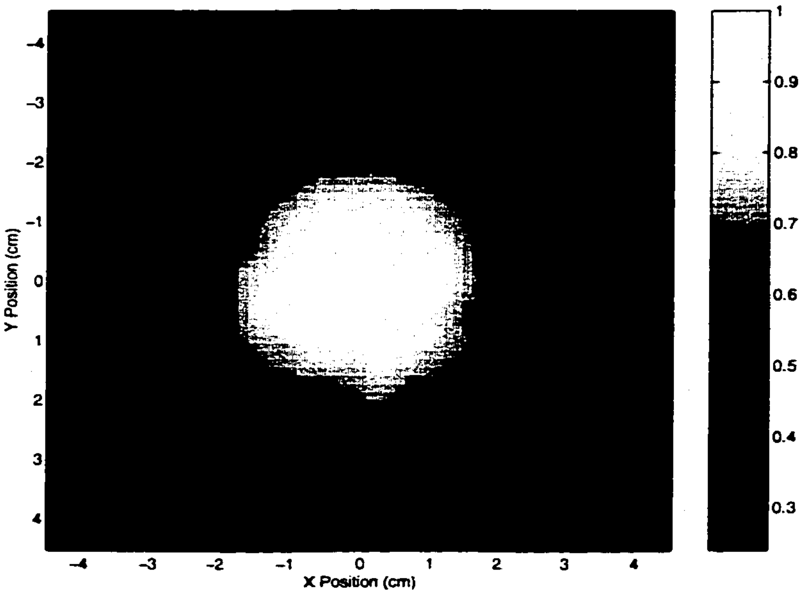

Figure 6.4: The backprojected image for the Cs-137 point source. The activities are normalized by the maximum pixel value. The total 1971 events within the full energy select window are equally divided into 12 groups to simulated 12 azimuthal sampling between 0° to 330° of the source plane.

6.2.2 Cs-137 Point Source Image

The backprojected image for the point source is shown in Figure 6.4. The line profile along the x direction is shown in Figure 6.5 with a FWHM of 5.7 cm. Figure 6.6 is the list mode maximum likelihood reconstructed image. The line profile along the x direction is shown in Figure 6.7. The FWHM for the reconstructed image is 0.77 cm, equivalent to 5.0° angular resolution. Comparing with the analytically predicted angular resolution 2.8° around 50° scatter angle for 662 keV gamma rays, the measured angular resolution is worse than our prediction. An analysis of the camera resolution is provided later in Section 6.4.

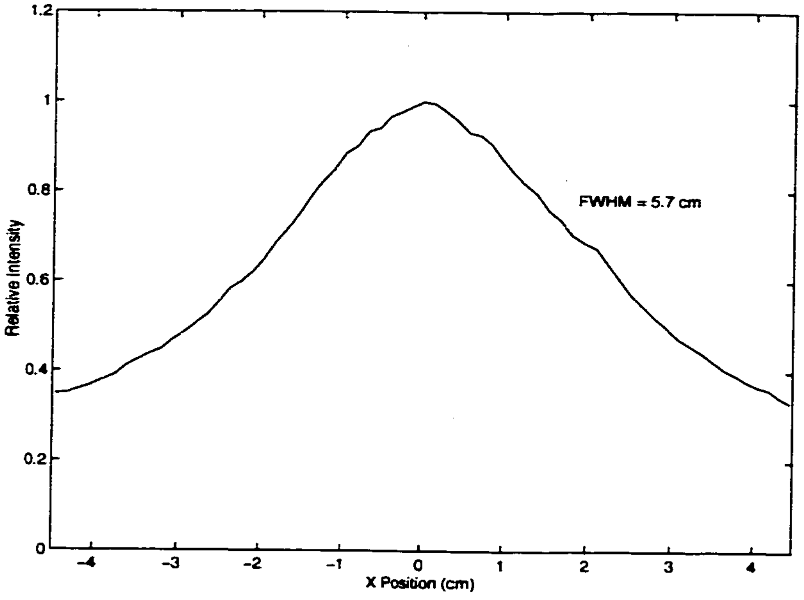

Figure 6.5: The line profile along the x direction for the backprojected image.

6.2.3 Point Source Efficiency

The total number of the events within the selection window is 1971, acquired over a data collection time of 4.0×10^5 seconds. So, the count rate is 4.9×10^{-3} per second. Since the point Cs-137 source AY642 activity was 287 kBq, the absolute efficiency (ε) for the camera is 1.71×10^{-8}. The intrinsic efficiency then is $\varepsilon_{ice} = \varepsilon/\Omega = 1.71 \times 10^{-8} \times 8.45^2 * 4\pi = 1.53 \times 10^{-5}$. Compared with our Monte Carlo calculated camera intrinsic efficiency $\varepsilon_{ice\_cal} = 1.03 \times 10^{-4}$ at 662 gamma rays, the measured efficiency is only 0.1488 of the calculated value.

There are two major factors that contribute to this low measured efficiency. First, due to wire-bonding problems and bad VA1 channels, only 114 pixels in the first detector work properly, and only 83 pixels in the second detector work properly. Second, due to the electron transport and charge carrier diffusion, according to our

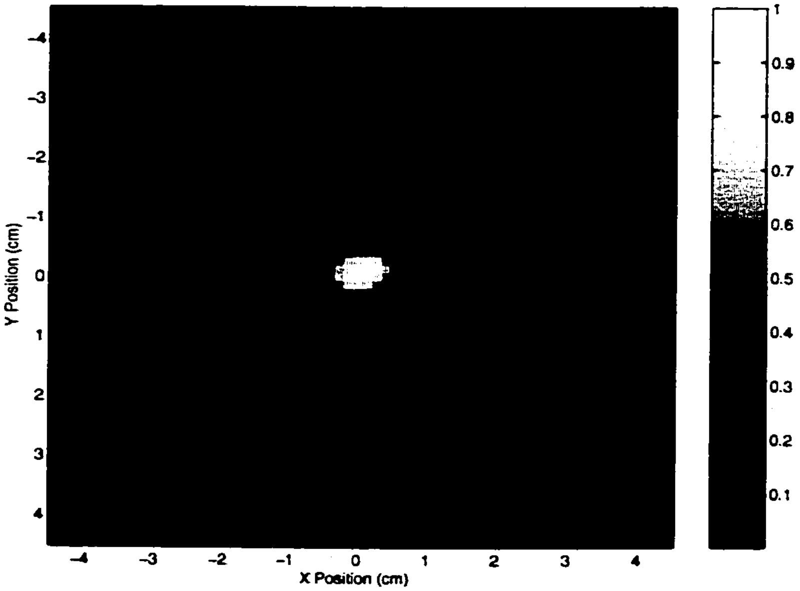

Figure 6.6: List-mode likelihood reconstructed image for the Cs-137 point source after 6 iterations.

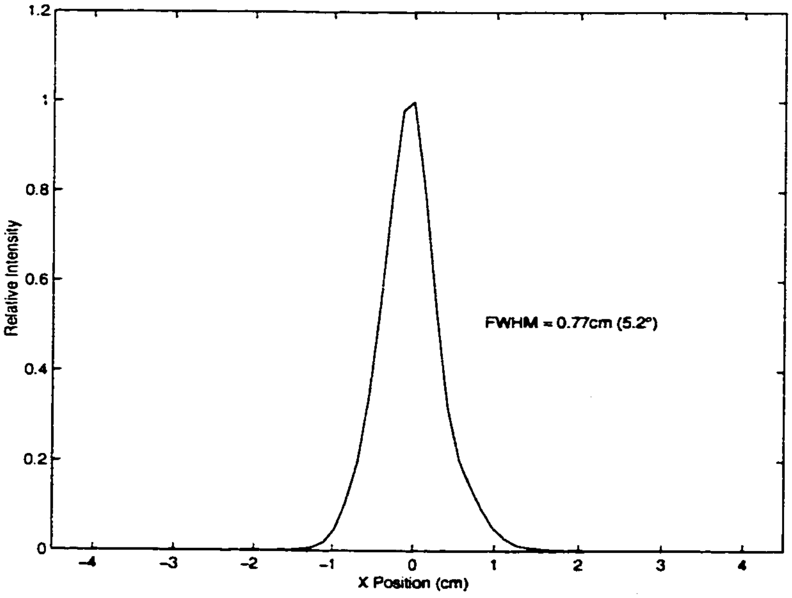

Figure 6.7: Line profile along the x direction for the reconstructed image in Figure 6.6.

Monte Carlo simulation [Du98], only 50% of photoelectric events at 662 keV can be recorded as single pixel events, and only 60% can be recorded as single pixel events at 122 keV. Assuming the charge sharing for a 200 keV energy transfer in the first detector is similar to that of the 122 keV gamma rays, and the situation for the 460 keV scattered photon is similar to that for 662 keV, if we multiply these efficiency loss factors together, we obtain $114/121 \times 83/121 \times 0.6 \times 0.5 = 0.1936$. Compared with the measured to the calculated efficiency ratio 0.1488, the difference between the measured efficiency and the simple estimation is only 5%. As presented in Section 5.4.3, there is strong charge sharing in the first detector for some pixels near the cathode side. This unusually strong charge sharing will further decrease the single pixel event efficiency. Therefore, our measured effiency is consistent with the Monte Carlo calculation.

6.3 Cs-137 Line Source Image

In order to test the imaging capabilities of the camera for spatially extended sources, a 100 μCi 5 cm long line Cs-137 source (Isotope Products Laboratories, serial number SS-975) was imaged. For the spatially extended source, the source has to physically rotate around the center of the FOV in order to get adequate azimuthal sampling. For this line source, four sets of data are collected with the line source located at $0°, 90°, 180°$ and $270°$ relative to the X axis of the source plane.

Figure 6.8 is the backprojected image for the Cs-137 line source with 26191 total events. It is a blurred line distribution. Figure 6.9 is the list mode maximum likelihood reconstructed image. The effect of the image reconstruction is very obvious in Figure 6.9, where most of the activity is concentrated on the line source location. A vertical line profile across the center of the source plane is shown in Figure 6.10. The

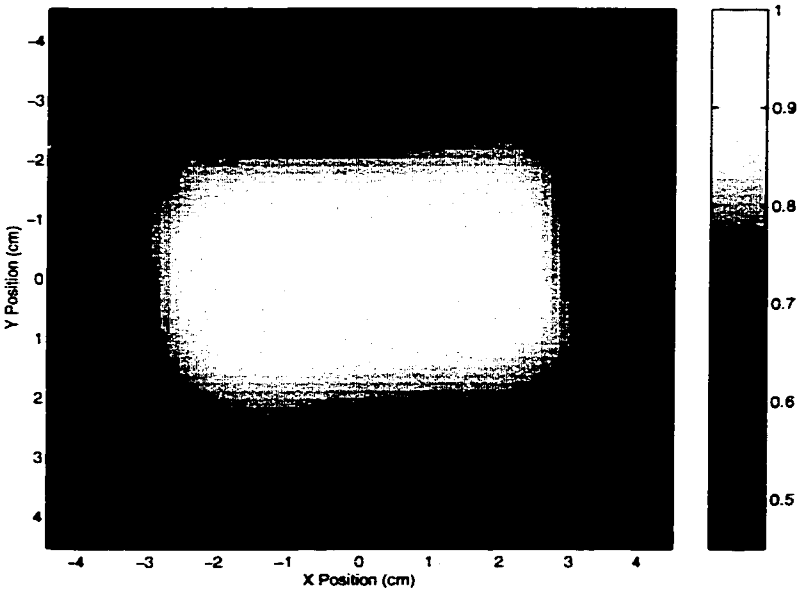

Figure 6.8: Backprojected image for the Cs-137 line source. The source activities are normalized by the maximum pixel value. Four sets of data are collected with the line source located at 0°, 90°, 180° and 270° relative to the X axis of the source plane. The data collecting time at each angle is 12 hours. This is the image from 26191 total events.

FWHM for the line source image is 0.976 cm. According to the source manufacturer specification, the active diameter for the line source is 0.584 cm. Then the intrinsic FWHM for the line image is $\sqrt{0.976^2 - 0.584^2} = 0.782(cm)$. Compared with 0.77 cm FWHM for the point source, the FWHM for the line source is consistent with that for the point source. Figure 6.11 is the horizontal line profile for the line source. The FWHM along the X direction is less than the 5 cm. The reason for this short distribution is unclear at this time.

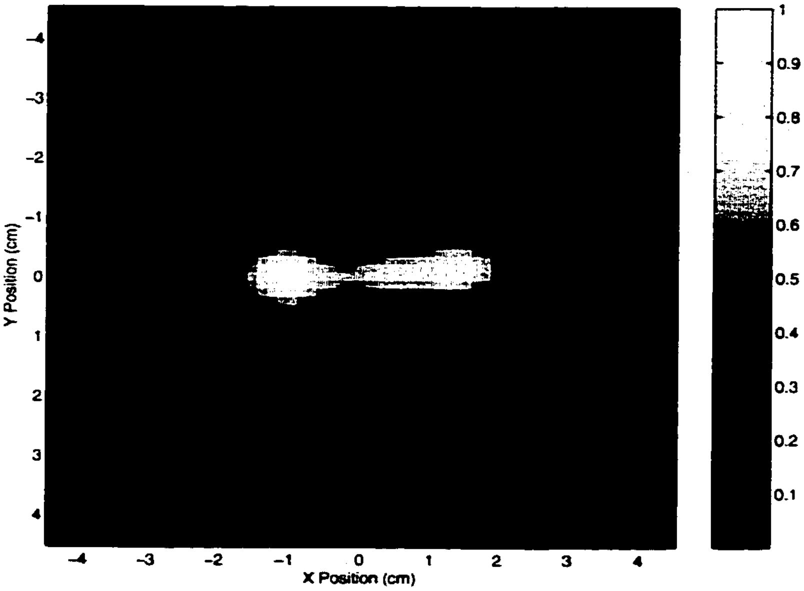

Figure 6.9: List mode maximum likelihood reconstructed image for the Cs-137 line source after 6 iterations.

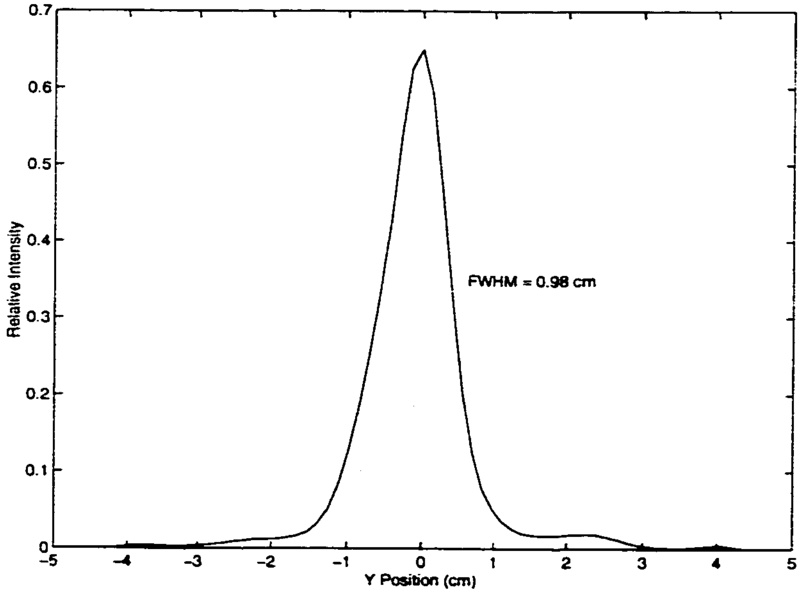

Figure 6.10: Line profile along the y direction for the Cs-137 line source.

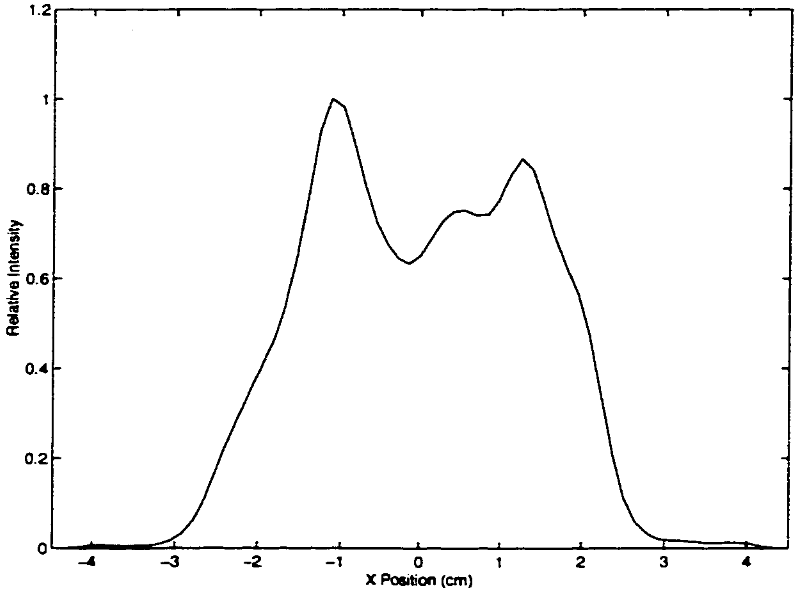

Figure 6.11: Line profile along the x direction for the Cs-137 line source.

6.4 Angular Resolution Analysis

As presented in the last two sections, the measured 5° angular resolution for both the point source and line source image is worse than our analytical predicted angular resolution 2.8°. Besides the intrinsic angular resolution degradation factors such as the detector energy resolution, detector position resolution, and the Doppler broadening effects, any other system errors for the detectors, such as the energy calibration error, non-linearity for the C/A ratio, and detector response shifting over time, as well as contaminating events, like chance coincident events and the wrong sequence of interaction events, will all contribute to the overall camera angular broadening.

6.4.1 Energy Calibration Errors

In order to derive the backprojection angle for each event, the absolute energy is needed for each event. The detector energy calibration is based on the measured photopeak centroids for 59.5 keV, 122 keV, 136 keV and 662 keV gamma rays. For example, the calibration data for the first detector are listed in Table 6.1. By a least squares fit, the energy and the photopeak centroid relation is given by

Source Energy (keV)	Photopeak centroid (ADC Channels)	Calculated Energy (keV)	Calibration Error (keV)
59.5	85	56.4	-3.06
122	175	123.3	1.3
136	196	138.8	2.8
662	900	661.5	-0.5

Table 6.1: Energy calibration parameters for the first detector

$$E = 0.7424 \times ch - 6.6669, \tag{6.1}$$

where E is the energy in keV and ch is the ADC channel number. The calculated energy according to this formula is listed in the 3rd column of Table 6.1. As shown in the 4th column of Table 6.1, the calibration error is between -3 keV to 2.8 keV. According to Equation 2.13, a 3 keV energy error will contribute to 0.6° angular uncertainty. This contribution will be added in quadrature to the overall angular resolution. Compared with the 1.8° detector energy resolution and 2° position resolution contribution, the energy calibration error contribution can be neglected.

6.4.2 Non-linear Relationship Between the C/A Ratio and Physical Depth

For our 3-D CdZnTe detectors, the depth position is derived from the cathode to anode pixel ratio. For simplicity, a linear relationship between the C/A ratio and the physical depth is used. The normalized C/A ratio is equally divided into 20 depth indexes, corresponding to 20 equally spaced 0.5 mm thick detector slices. This simple linear relationship between the C/A ratio and interaction depth is only true under following conditions:

- 1. The hole contribution can be neglected.
- 2. The anode pixel signal is independent of the depth and there is complete electron collection by the anode pixels.

However in reality, due to finite hole drifting, especially near the cathode side where holes can be collected by the cathode, the holes will contribute to the cathode signal. Due to the electron trapping, and the rapid weighting potential change near the anode, the anode pixel signal is also depth dependent. A simple model including these effects indicated that this non-linearity could lead to 0.8 mm depth error [Li00], which is larger than the 0.5 mm depth position resolution in our angular resolution estimation. For the actual detectors, due to non-uniform electric field distribution inside the crystal and the incomplete charge collection, the actual depth position error should be larger than the 0.8 mm model prediction. If we assume the depth resolution is 1 mm instead of 0.5 mm, then the depth position uncertainty contribution to the angular resolution will increase from 1.01° to 2.03°. Then the overall angular resolution will increase to 3.3°.

6.4.3 System Instability Over the Long Data Acquisition Time

It is observed that the photopeak centroid for both detectors have about 3% shift over time. When we collect the spectrum for individual detectors, due to the high count rate, the data collection time is usually less than 12 hours. System instability over such a short time is not obvious. Furthermore, the existence of a clear photopeak in the spectrum enables us to use the photopeak centroid to correct any shift. But in coincidence image data collection, the count rate is very low. It took 4.0×10^5 second (5.5 days) to collect the data for the Cs-137 point source. As shown in Figure 6.1, since there is no clear photopeak in the coincident spectrum, we can not use the same correction method to correct the detector response shift. These system shifts will broaden the detector energy spectrum, and therefore contribute to a larger angular resolution.

6.4.4 Chance Coincident Events

The Compton scatter Equation 2.1 is not valid for chance coincident events, which will give false directional information and contribute to background artifacts in the reconstructed image. As shown in Figure 6.3, those events in the summed energy spectrum above the full energy peak are solely due to chance coincidence. The total counts within the 400 ADC channels above 700 keV is 88. Assuming the chance coincidence rate is same for energy spectrum below 700 keV, the chance counts within our selection window is 22 counts, only 1.12% of the total counts. Therefore, the influence of the chance coincident events can be neglected for the point source image. The very low background artifacts in the reconstructed image in Figure 6.6 also indicate this. For the Cs-137 line source, the source activity is 100 μCi, about 10 times higher than the point source activity. Therefore, the true coincidence count rate should be 10 times of that for the point source. However since the chance coincidence rate is given by

$$n = 2\tau n_1 n_2, \tag{6.2}$$

where the τ is the coincidence resolve time, n_1 and n_2 are the individual detector counting rate, the chance coincidence rate should be 100 times higher than that for the point source. Therefore, the chance count to the true coincidence count ratio should be around 11%. The chance coincident events should have more influence to the angular resolution for line source than for the point source. Thus, the increase in background artifacts in Figure 6.9 for the line source image is mainly due to the chance coincident events.

6.4.5 Wrong Interaction Sequence Events

With only two interaction positions and energy information, we can not identify the interaction sequence in two detectors. For a coincident event, we always assume the photon first Compton scatters in the first detector and then the scattered photon is detected by the second detector. The backprojection is based on this assumption. For those events that have the photons first scatter in the second detector, the backprojection will give a false directional information, just like a chance coincident event. From the geometrical relationship between the source and two detectors, the backscatter angle from the second detector to the first detector is 150° for the point source, and 140° to 160° for the 5 cm long line source when the source is in a horizontal direction. From the Compton scatter energy distribution in Figure 6.12, at 150°, the scattered photon energy is 193.8 keV. If this scattered photon is absorbed by the first detector, the backprojection direction from the centers of two detectors is 48°, 2° away from the true source position. For this false event, the interaction

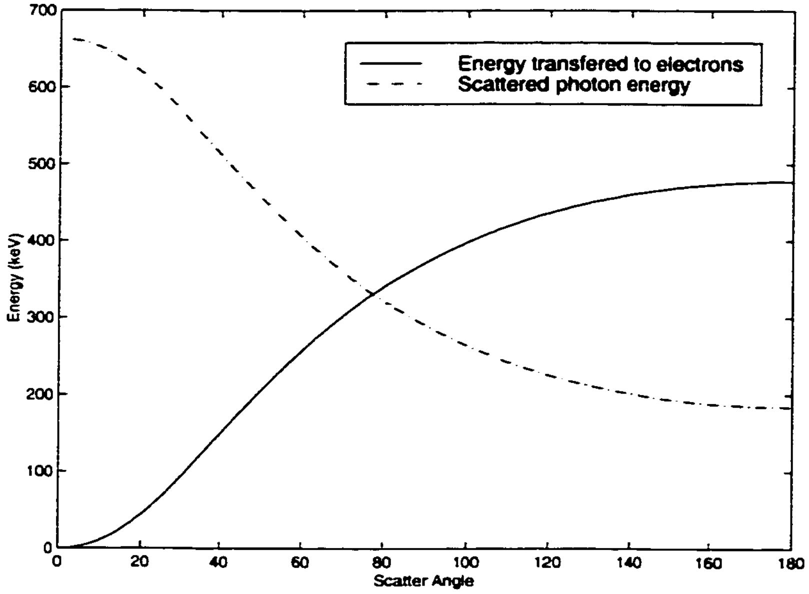

Figure 6.12: Compton scatter energy distribution for 662 keV gamma rays.

positions also lead to wrong backprojection direction, thus the actual error will larger than 2°. When the point source is at the center of the FOV, the distance to the center of the second detector is 12.3 cm. As shown in Figure 6.13, the relative angular cross section are 0.3644 and 0.1481 at 50° and 150° respectively for 662 keV gamma rays. Then the ratio between correct sequence and wrong sequence is $8.45^2/12.3^2 \times 0.1481/0.3644 = 0.19$. Due to the attenuation in the first detector, the real ratio should be smaller than this simple estimation. These wrong sequence events will have little effect on the point source imaging. However for the line source, although the backscatter angle is from 140° to 160°, the scattered photon energy only changes from 188.5 keV to 201.5 keV. The corresponding false backprojection angle is from 47° to 49° from two detectors' centers. Although the source activity is distributed along the 5 cm long line (36 pixels in the reconstruction source plane), all

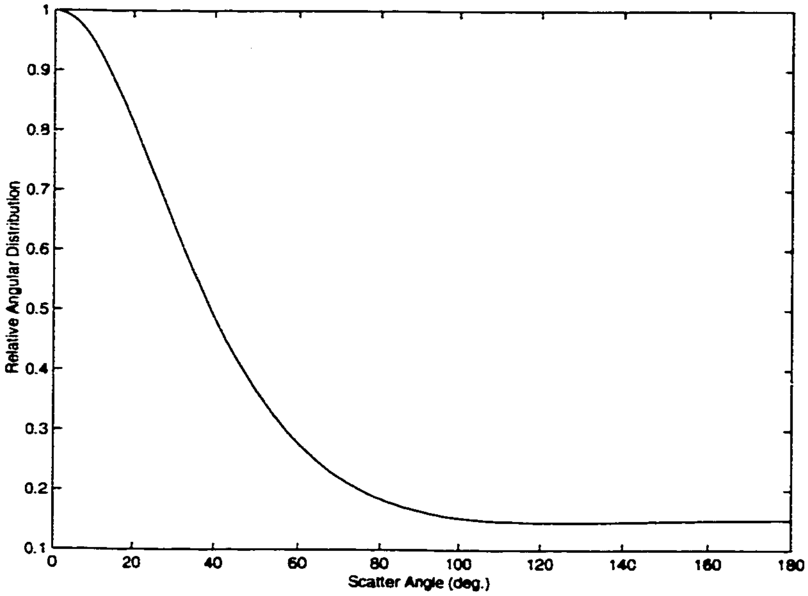

Figure 6.13: Relative Compton scatter angular distribution at 662 keV.

the wrong sequence events will contribute to the similar backprojection angle from 47° to 49°. This is equivalent to a false source near the center of the field-of-view. This is the major reason why there are bumps around the center for the line source in Figure 6.11 and the poorer angular resolution for the line source than that for the point source. In order to eliminate the influence of these wrong sequence events, a collimator between the two detectors can be used.

In summary, the worse measured angular resolution is mainly due to the non-linear relationship between the C/A ratio and the physical depth, system instability over the long data collection time, chance coincidence, and wrong interaction sequence events.

CHAPTER VII

SUMMARY AND RECOMMENDATIONS FOR THE FUTURE WORK

7.1 Summary

In this work, the development of a prototype Compton scattering camera using two 1cm^3 cubic 3-D position sensitive CdZnTe detectors is presented. For each gamma ray interaction in the 3-D CZT detectors, the energy and the lateral information is given by the anode pixel signal and the depth information is derived from the ratio between the cathode and the anode pixel signal.

The analytically predicted camera angular resolution based on our measured detector energy resolution is $3° - 4°$ at 511 keV and reduces to $2° - 3°$ at 1 MeV for scatter angles at $20° - 80°$. The optimal offset angle θ_c between the two detectors should be 50° and the center to center distance between the two detectors should be 5 cm. The field of view (FOV) will be $\pm 30°$ around the axis of the first detector corresponding to $20° - 80°$ scatter angles. The predicted intrinsic camera efficiency for this prototype camera is 1.5×10^{-4} to 8.8×10^{-6} from 500 keV to 3 MeV. As shown in Figure 2.10, Si, Ge and CZT need to have more than 1 cm thickness to get their maximum Compton Aperture Efficiency (CAE) for energy above 300 keV. For such a thick detector, without the depth sensing capability, the distance between two detectors has to be increased to reduce the detector thickness contribution to the angular uncertainty. Thus the overall camera efficiency will be reduced. With the 3-D sensing capability, the maximum CAE can be achieved without sacrificing the overall camera effiency. The 3-D material non-uniformity and electron trapping correction capability is also helpful in improving the overall angular resolution by improving the overall energy resolution. Furthermore, the CZT detectors can operate at room temperature. Therefore, CZT detectors with 3-D position sensitive capability are a better choice than Si or Ge detectors for Compton scatter imaging in the middle and high energy range.

The impractically large memory requirement for the system response matrix and the coincident spectrum prohibits the use of any iterative reconstruction algorithm that requires them. List mode data acquisition and image reconstruction is the only practical choice. Although list mode backprojection filter (BPF) reconstruction is simple and fast, in Compton scatter imaging the intersection of the backprojected cone and the source plane is not a simple straight line as in Computerized Tomography(CT). The simple ramp filter relationship between the original image and its straight line backprojection is not accurate for Compton scatter imaging. As a result, the BPF reconstructed Compton scatter image exhibits artifacts. Therefore, list mode maximum likelihood image reconstruction algorithm is chosen for our Compton camera for image reconstruction. The test results from the Monte Carlo simulated data verified the analytical angular resolution predictions.

The anode pixel signals from each detector are read out by an integrated ASIC VA1 chip. There are 128 independent signal processing channels in one VA1 chip. Each channel has its independent preamplifier, shaping amplifier and sample/hold circuit. For each interaction, all 128 channels need to be serially read out. The falling edge of the transient signal from the anode grid is used to generate the trigger signal for each detector. In order to read out signals in coincidence mode from the two 3-D detectors, a special control circuit was built to coordinate the two VA1 chips. Both VA1 chips hold themselves long enough to allow the signals to be serially read out in coincident events. Each VA1 chip can reset quickly in single detector events. This implementation prevents the single detector events from dominating the system dead time in coincidence data acqusition.

In order to reduce the leakage current contribution to the electronic noise, the two CZT detectors were upgraded from DC coupling to AC coupling between the anode pixels and VA1 inputs. Under the new AC coupling, the electronic noise for both detectors is only around 3 keV. The energy resolution is around 6 keV, 7 keV and 12 keV for 59.5 keV, 122 keV and 662 keV respectively for both detectors after applying the three-dimensional corrections for material non-uniformities and electron trapping. Both detectors have non-uniform responses for the energy resolution and the photopeak efficiency from different pixels. The abnormal photopeak area distribution along the depth indexes, especially for some pixels in the first detector, is primarily due to the strong, non-uniform charge sharing. The measured energy resolution is worse than the conservative estimation that included the electronic noise and charge carrier number fluctuations. Material non-uniformity, charge sharing, and incomplete electron collection by the anode pixels are additional energy resolution degradation factors.

The imaging capability of the system has been tested using both a point and a line Cs-137 source. The measured spatial resolution FWHM for the reconstructed image is 0.77 cm when the Cs-137 point source was located 8.45 cm from the center of the first detector, at 50° relative to the centers of the two detectors. The equivalent angular resolution FWHM is 5.2°. The angular resolution for the line Cs-137 source is similar to that for the point source. These measured angular resolution values are worse than the analytical predicted angular resolution 2.8° around 50° scatter angle for 662 keV gamma rays. The non-linear relationship between the C/A ratio and the physical depth, system instability over the long data collection time, chance coincidence and wrong interaction sequence events can all contribute to the angular resolution degradation. The intrinsic camera efficiency for the point Cs-137 source is 1.53×10^{-5}. Compared with our Monte Carlo calculated camera intrinsic efficiency 1.03×10^{-4} at 662 gamma rays, the measured efficiency is only 0.1488 of the calculated value. The bad pixels and the charge sharing are the two major factors that contribute to this low measured efficiency. A simple estimation considering these two factors indicates our measured effiency is consistent with the Monte Carlo calculation.

In conclusion, the first prototype Compton scattering camera using two 3-D CZT detectors has been built and tested. Its imaging capability has been demonstrated both for a point source and a line source. Comparing with other previously built Compton cameras, this system is very compact and can operate at room temperature. The CZT detectors with 3-D position sensing capability under the current energy resolution can be used effectively for Compton scatter imaging for gamma ray energy above 500 keV, especially for portable imaging devices.

7.2 Recommendations for Future Work

Under the current VA1 working mode, we can not read out the correct signal amplitudes from multiple interaction events. We have to reject all multiple pixel events in both the individual detector spectrum collection and the coincidence imaging data collections. This not only causes significant efficiency loss but also contributes to the low energy tail for the photopeak. A new read out ASIC such as VAS-TAT with self-triggering and peak-hold capability for each channel is highly recommended. If the new ASIC can read out the correct signal amplitudes for multiple pixel events, the detection efficiency will be increased significantly by including these events. Furthermore, the centroid lateral position from multiple pixels can be used for single interaction events. If the electronic noise from each channel is low enough, then the detector lateral position resolution can be smaller than the physical pixel size. This improved position resolution will allow a smaller distance between the two detectors while maintaining the same angular resolution, thus increasing the overall camera efficiency.

It will be helpful if the depth calibration can be carried out directly using a well collimated source. Then the influence of the non-linearity between the C/A ratio and the depth index can be eliminated.

BIBLIOGRAPHY

BIBLIOGRAPHY

[Ait90] F. Ait-Ouamer, et al., "Calibration and Performance of the UCR Double Compton Gamma Ray Telescope," *IEEE Trans. Nucl. Sci.* 37(2)(1990)535.

[Aku69] W. Akutagawa and K. Zanio, *J. Appl. Phys.* 40(1969)3838.

[Ang58] H.O. Anger, "Scintillation Camera," *Rev. Sci. Instrum.* 29(1)(1958)27.

[Bar72] H.H. Barrett, *J. Nucl. Med.* 13(1972)382.

[Bar95] H.H. Barrett, J.D. Eskin and H.B. Barber, *Phys. Rev. Lett.* 75(1)(1995)156.

[Big75] F. Biggs, L.B. Mendelsohn, J.B. Mann, "Hartree-Fock profiles for elements," *Atomic Data and Nuclear Data Tables* 16(1975)201.

[Bre88] R.R. Brechner, M. Singh, "Comparison of an Electronically collimated system and a Mechanical cone-beam system for Imaging single Photons," *IEEE Trans. Nucl. Sci.* 35(1)(1988)649.

[Ces92] R. Cesareo el al., "Interaction of keV photons with matter and new applications," *Physics Reports* 213(3)(1992)117.

[Cop77] M.J. Copper, "Compton scattering and electron momentum," *Contemporary Physics* 18(5)(1977)489.

[Cou] Coulomb, Integrated Engineering Software, 46-1313 Border Place, Winnipeg, Manitoba, Canada.

[Dem77] A. Dempster, N. Laird, and D. Robin, "Maximum likelihood from incomplete data via EM algorithms," *J. R. Statist. Soc. Ser.* B 39(1977)1.

[Du99] Y.F. Du, Z. He, W. Li, G.F. Knoll, D.K. Wehe, "Monte Carlo Investigation of the Charge Sharing Effects in 3-D Position Sensitive CdZnTe Gamma Ray Spectrometers," *IEEE Trans. Nucl. Sci.* 46(4)(1999)844.

[Egs4] SLAC Report-265, Stanford Linear Accelerator Center, Stanford University, Stanford, California

[Fuj87] I. Fujieda, and V. Perez-Mendez, "Theoretical considerations of a New Electronically collimated Gamma Camera utilizing Gas Scintillation," *SPIE Medical Imaging* 767(1987)84.

[Gea3] GEANT3, CERN, Geneva, Switzerland.

[Gor70] R. Gordon, R. Bender, and G.T. Herman, "Algebraic Reconstruction Techniques (ART) for three Dimensional Electron Microscopy and X-Ray Photography," *J. THeo. Biol.* 29(1970)47.

[Gor74] R. Gordon, "A Tutoral on ART," *IEEE Trans. Nucl. Sci.* NS-21(1974)78.

[He96] Z. He et al., "1-D position sensitive signle carrier semiconductor detectors," *Nucl. Instr. & Meth.* A 380(1996)228.

[He97] Z. He et al., "Position sensitive single carrier CdZnTe detectors," *Nucl. Instr. & Meth.* A 388(1997)180.

[He99] Z. He, W. Li, G.F. Knoll, D.K. Wehe, J. Berry, C.M. Stahle, "3-D position sensitive CdZnTe gamma-ray spectrometers," *Nucl. Instr. & Meth.*, A 422(1999)173.

[He00] Z. He, W. Li, G.F. Knoll, D.K. Wehe, C.M. Stahle, "Measurement of material uniformity using 3-D position sensitive CdZnTe gamma-ray spectrometers," *Nucl. Instr. & Meth.*, A 441(2000)459.

[Hec32] K. Hecht, *Physik* 77(1932)235(1932).

[Her75] D. Herzo, et al., "A Large Double Scatter Telescope for gamma rays and neutrons," *Nucl. Instr. & Meth.* 123(1975)583.

[Jon75] L.T. Jones and R.B. Woollam, *Nucl. Instr. & Meth.* 124(1975)591.

[Kno93] G.F. Knoll and D.S. McGregor, *MRS Proc.* 302(1993)3.

[Kno00] G.F. Knoll, *Radiation Detection and Measurement*, third edition, John Wiley & Sons, Inc. 2000.

[Kur98] J.D. Kurfess, "Compton Scatter Imaging in Astrophysics," *IEEE Trans. Nucl. Sci.* 45(3)(1998)936.

[LeB98] J.W. LeBlanc, et al., "C-SPRINT: A Prototype Compton Camera System For Low Energy Gamma Ray Imaging," *IEEE Trans. Nucl. Sci.* 45(3)(1998)943.

[Li99] W. Li, et al., "A Data Acquisition and Processing system for 3-D Position sensitive CZT Gamma-Ray Spectrometers," *IEEE Trans. Nucl. Sci.* 46(6)(1999)1989.

[Li00] W. Li, Z. He, G.F. Knoll, D.K. Wehe, Y.F. Du, "A Modeling Method to Calibrate the Interaction Depth in 3-D Position Sensitive CdZnTe Gamma-Ray Spectrometers," *IEEE Trans. Nucl. Sci.* 47(3)(2000)890.

[Loc79] J.A. Lockwood, et al., "Atmospheric Neutron and Gamma-Ray Fluxes and Energy Spectrum," *J. Geophy. Res.* 84(1979)1402.

[Luk94] P.N. Luke, "Single-polarity charge sensing in ionization detectors using coplanar electrodes," *Appl. Phys. Lett.* 65(22),28(1994)2884.

[Luk95] P. N. Luke, *IEEE Trans. Nucl. Sci.* NS-42(1995)207.

[Luk96] P. N. Luke, "Electrode configuration and energy resolution in gamma ray detectors," *Nucl. Instr. & Meth.* A 380(1996)232.

[Mar93] J.B. Martin, et al., "Imaging Multi-Energy Gamma-Ray Fields with a Compton Scatter Camera," *IEEE Trans. Nucl. Sci.* 41(4)(1994)1019.

[Mar94] J.B. Martin, et al., "A Ring Compton Scatter Camera For Imaging Medium Energy Gamma Rays," *IEEE Trans. Nucl. Sci.* 40(4)(1993)972.

[McG97] D.S. McGregor and H. Hermon, "Room-temperaute compound semiconductor radiation detectors," *Nucl. Instr. & Meth.* A395(1997)101.

[McG99] D.S. McGregor and R.A. Rojeski, "Performance of CdZnTe Geometrically weighted semiconductor Frisch grid radiation detectors," *IEEE Trans. Nucl. Sci.* 46(3)(1999)250.

[Mer61] L. Mertz, N.O. Young, *Proc. Int. Conf. on Opt. Inst.* 305(1961).

[Mur88] K.G. Murthy, *Linear Complementarity, Linear and Non-linear programming.* Berlin, Helderman Verlag, 1988.

[Nor79] S.J. Norton and M. Lionzer, "Ultrasonic reflectivity tomography: Reconstruction with circular transducer arrays," *Ultrasonic Imaging* 1(1979)154.

[Ord98] C.E. Ordonez, A. Bolozdynya, and W. Chang, "Doppler Broadening of Energy Spectra in Compton Camera," 1998 IEEE Nuclear Science Symposium and Medical Imaging Conference record, 8-14 November 1998, Toronto, Canada.

[Ord99] Caesar E. Ordonez, Wei Chang, "Angular uncertainties due to geometry and spatial resoluition in Compton cameras," *IEEE Trans. Nucl. Sci.* 46(4)(1999)1142.

[Par98] L. Parra, H.H. Barrett, "List-Mode Likelihood: EM algorithm and image quality estimation demonstrated on 2-D PET," *IEEE Trans. Med. Imag.* 17(2)(1998)228.

[Pat96] B.E. Patt, J.S. Iwanczyk, G. Vilkelis and Y.J. Wang, *Nucl. Instr. & Meth.* A 380(1996)276.

[Pho] Applied Inventions Corp. Software. P. O. Box 544, Grafton, Massachusetts 01519.

[Ram39] S. Ramo, *Proc. IRE* 27(1939)584.

[Red96] R. Redus, M. Squillante and J. Lund, "Electronics for high resolution spectroscopy with compound semiconductors," *Nucl. Instr. & Meth.* A 380(1996)312.

[Ric92] M. Richter and P. Siffert, "High resolution gamma ray spectroscopy with CdTe detector systems," *Nucl. Instr. & Meth.* A 322(1992)529.

[Sau88] K, Sauer and C. Bouman, "A local update strategy for iterative reconstruction from projections," *IEEE Trans. Sig. Proc.* 41(2)(1993)534.

[Sch73] V. Schonfelder, et al., *Nucl. Instr. & Meth.* 191(1973)385.

[Sch82] V. Schonfelder, et al., "Properties and Performance of the MPI Balloon Borne Compton Telescope," *Astron. Astrophys.* 110(1982)138.

[Sch84] V. Schonfelder, et al., "The Imaging Compton Telescope, COMPTEL, on the Gamma Ray Observatory," *IEEE Trans. Nucl. Sci.* NS-31(1)(1984)766.

[Sch93] V. Schonfelder, et al., "Instrument Description and Performance of the Imaging Gamma-Ray Telescope COMPTEL aboard the COMPTON Gamma Ray Observatory," *Astrophys. J. Suppl.* 86(1993)657.

[She82] L. Shepp and Y. Vardi, "Maximum likelihood reconstruction for emission tomography," *IEEE Trans. Med. Imag.* 1(1982)113.

[Sco38] W. Schockley, *J. Appl. Phys.* 9(1938)635.

[Sin83a] M. Singh, *Med. Phys.* 10(1983)421.

[Sin83b] M. Singh, D. Doria, *Med. Phys.* 10(1983)428.

[Sol88] C. Solomon, et al., "Gamma Ray Imaging with Silicon detectors - a Compton camera for Radionuclide Imaging in Medicine," *Nucl. Instr. & Meth.* A 273(1988)787.

[Squ89] M.R. Squillante, G. Entine, E.E. Frederick, L. Cirignano and T. Hazlett, *Nucl. Instr. & Meth.* A 283(1989)323.

[Tak96] H. Takahashi, et al., "Signal processing for CdTe detectors using a fast signal digitalizing techniques," *Nucl. Instr. & Meth.* A 380(1996)381.

[Tum95] O.T. Tumer, et al., "The TIGRE Instrument for 0.3-100 MeV Gamma-Ray Astronomy," *IEEE Trans. Nucl. Sci.* 42(4)(1995)907.

[Tod74] R.W. Todd, J.M. Nightingale, and D.B. Everett, "A proposed γ Camera," *Nature* 251(1974)132.

[Wil01] S.J. Wilderman, J.A. Fessler, N.H. Clinthorne, J.W. LeBlanc, W.L. Rogers, "Improved modeling of system response in list mode reconstruction of Compton scatter camera images," *IEEE Trans. Nucl. Sci.* 48(1)(2001)111.

[Zan77] K. Zanio, *Rev. De Phys. Appl.* 12(1977)343.